Weight Estimation Of Turboshaft Engines

Continuation in the development of WEST: a component based preliminary design and weight estimation tool for turbine engines

Frederick Verweij

Technische Universiteit Delft

TU Delft Delft University of Technology

Challenge the future

Weight Estimation Of Turboshaft Engines

Continuation in the development of WEST: a component based preliminary design and weight estimation tool for turbine engines

by

Frederick Verweij

in partial fulfillment of the requirements for the degree of

Master of Science
in Aerospace Engineering

at the Delft University of Technology,
to be defended publicly on Tuesday October 9, 2023 at 2:30 PM.

Supervisor:	Dr. ir. Carlo De Servi	TU Delft
Thesis committee:	Prof. dr. ir. Piero Colonna,	TU Delft
	Dr. ir. Matteo Pini,	TU Delft
	Dr. ir. Feijia Yin	TU Delft

An electronic version of this thesis is available at http://repository.tudelft.nl/.

TU Delft Delft University of Technology

PREFACE

Ever since I was a child, as far back as the second or third grade, if anyone asked me what would I have liked to be when I grew up, I would have always answered the same thing: “I want to be an aeronautical engineer”. Some time has passed now, but my answer is still the same. This is the reason why I chose to come to study at TU Delft, and the reason I chose this faculty.

With this work I hope to conclude this journey and finally fulfill my dream.

Frederick Verweij
Delft, September 2023

ACKNOWLEDGEMENTS

I wish to express my deep gratitude to my supervisor, Dr. Carlo De Servi, for his invaluable contributions to this thesis project. He not only provided the thesis topics but also extended unwavering support throughout the entire duration of this endeavor.

I would also like to extend a special acknowledgment to Dabo Krempus, a dedicated PhD candidate who closely followed my progress and offered continuous feedback and assistance. Dabo's provision of crucial literature sources significantly contributed to the quality of the methodology employed in this report, and his feedback during our discussions was crucial for finishing this work.

My heartfelt thanks go out to my thesis committee for their willingness to participate and for affording me the opportunity to defend the substantial effort I invested in this research.

I am indebted to the professors of the Aerospace Engineering faculty at Delft University of Technology for their invaluable contributions to my education. They have imparted extensive knowledge about aero engine technology and prepared me exceptionally well for this thesis. I would like to particularly recognize the significant impact of Dr. Gianfranco La Rocca, Dr. Matteo Pini, and Dr. Carlo De Servi in this regard.

Lastly, I want to extend my sincere appreciation to my family and friends, whose unwavering financial and emotional support was instrumental during my time studying in the Netherlands. I am profoundly grateful for their constant encouragement and belief in me.

Above all, I want to express my deepest gratitude to Sofia. Despite the distance that separated us for an extended period, her enduring love and unwavering encouragement were a source of strength and motivation throughout this journey. Her support was truly invaluable.

A Francesco, mi manchi tanto.

ABSTRACT

The need for more efficient aircraft has led to the conception of innovative engine configurations, such as the combined-cycle engine proposed by Delft University of Technology or the Water-enhanced turbofan developed by MTU and Pratt & Whitney. The evaluation of the potential benefits of these novel engine concepts requires detailed performance studies considering weight and drag penalties as figures of merit. At present, no weight estimation tools with sufficient level of accuracy and flexibility are publicly available, apart from WATE++, a tool developed by NASA. However, this software is subject to export control restrictions and cannot be used outside the USA. For this reason, the development of a new component-based preliminary engine design tool, "Weight EStimation of gas Turbine engines" (*WEST*), was started. The goal of WEST is to predict the weight of novel engine architectures with a reasonable level of accuracy, accounting for design parameters like turbine inlet temperature, overall pressure ratio, mass flow rate, and turbomachinery configuration, with a minimal set of geometry inputs specified by the user. A previous work demonstrated that WEST can effectively predict the weight of turbofan gas generators. As only the main components are modeled, the WEST estimates account for approximately 70 – 90% of the actual engine weight.

The capabilities of WEST were expanded in this study to allow for the design of small-scale turboshaft engines. To this purpose, a methodology to design radial compressor disks was implemented, and successfully verified against FEM results. Regarding the modeling of the complete turboshaft, it was found that the predictions of the tool account for only 60 – 70% of the actual engine weight. Such result was, however, expected, as WEST does not take into account the particle separator and the integrated gearbox, which may account for up to 30% of the engine's total weight.

Contents

List of Figures

List of Tables

NOMENCLATURE

ABBREVIATIONS

Abbreviation	Definition
2D	Two-Dimensional
3D	Three-Dimensional
APU	Auxiliary Power Unit
ARENA	Airborne Energy Harvesting for Aircraft
BPR	Bypass Ratio
°C	Degrees Centigrade
CAD	Computer Aided Design
CC	Combined-Cycle
CC-APU	Combined-Cycle Auxiliary Power Unit
CCE	Combined-Cycle Engine
const.	Constant
corr.	Corrected
deg.	Degree(s)
DLR	German Aerospace Center
e.g.	exempli gratia (“for example”)
etc.	et cetera
ft.	foot (feet)
FEA	Finite Element Analysis
FEM	Finite Element Method
FPT	Free Power Turbine
g	Gram(s)
GG	Gas Generator
GGT	Gas Generator Turbine
GTlab	Gas Turbine Laboratory
H	Hub (Radius)
HPC	High Pressure Compressor
HPT	High Pressure Turbine
i.e.	id est (“that is”)
in	Inch(es)
J	Joule(s)
JPL	Jet Propulsion Library
K	Kelvin
kg	Kilogram(s)
L	Lower
lb	Pound(s)
LE	Leading Edge
LER	Leading Edge Radius
LHV	Lower Heating Value
LPC	Low Pressure Compressor
LPT	Low Pressure Turbine
M	Mid (Radius)
m	Meter(s)
MJ	Megajoule(s)
mm	Millimetre(s)
MPa	Megapascal(s)

Abbreviation	Definition
ms	Millisecond(s)
MW	Megawatt(s)
N	Newton(s)
N/A	Not Applicable
NASA	National Aeronautics and Space Administration
Nom	Nominal
obj.	Objective
OPR	Overall Pressure Ratio
ORC	Organic Rankine Cycle
Pa	Pascal(s)
Qty	Quantity
rad	Radian(s)
RPM	Revolutions Per Minute
s	Second(s)
SF	Safety Factor (or Factor of Safety)
SFC	Specific Fuel Consumption
SI	International System of Units
T	Tip (Radius)
TE	Trailing Edge
Temp.	Temperature
TIT	Turbine Inlet Temperature
T-s	Temperature-Entropy (Diagram)
TU Delft	Delft University of Technology
U	Upper
UTS	Ultimate Tensile Strength
vs.	Versus
W	Watt(s)
WEST	Weight Estimation of Aeronautical Gas Turbine Engines
WHR	Waste Heat Recovery (Unit/System)
°	Degrees (Angle)

SYMBOLS

Symbol	Definition	Unit
$A, B, C, \ldots, H, r, q$	—	Coefficients
A	m^2	Cross-Sectional Area
AR	—	Aspect Ratio
b	m	Blade Height, or ...
b	m	Channel Height
BPR	—	Bypass Ratio
c	m	Chord, or ...
c	$J/kg \cdot K$	Specific Heat Capacity, or ...
c	m	Center of gravity axial coordinate
c_L	—	Lift Coefficient
c_p	$J/kg \cdot K$	Specific Heat Capacity (at Constant Pressure)
D	m	Diameter
DF	—	Diffusion Factor
D_H	—	DeHaller Number
E	Pa	Elastic (Young's) Modulus, or ...
E	J	Energy
F	N	Force
f	—	Factor
$f(\ldots)$	—	Function of $(\ldots)$

Symbol	Definition	Unit
G	Pa	Shear Modulus
g	—	Row or Stage Gap
g_0	m/s^2	Gravitational Constant/Acceleration
H	—	(Normalized) Maximum Arc Height
h	J/kg	Specific Enthalpy, or ...
h	—	Non-Dimensional Step Size (Finite Differences)
I_{sp}	s	Specific Impulse
k	$W/m \cdot K$	Thermal Conductivity, or ...
k	—	Impeller Shape Factor, or ...
l	m	Length
LHV	J/kgf	Lower Heating Value
M	$N \cdot m$	(Bending) Moment
m	kg	Mass, or ...
m	—	Mach Number
$\dot{m}$	kg/s	Mass Flow Rate
M	—	Mach Number
N	RPM	Rotational Speed
n	—	Number of ...
OPR	—	Overall Pressure Ratio
P	bar	Pressure, or ...
P	kW	Power
p	Pa	Pressure
PR	—	Pressure Ratio
Pr	—	Prandtl Number
R	m	Range, or ...
R	—	Degree of Reaction
r	m	Radius, or ...
r	m	Radial Coordinate
R_{gas}	$J/kg \cdot K$	Specific Gas Constant
S	N	Restoring Force
s	$J/kg \cdot K$	Specific Entropy
SF	—	Safety Factor
SFC	$g/kN \cdot s$	(Thrust) Specific Fuel Consumption
T	K	Temperature, or ...
t	m	Thickness
t/c	—	Thickness-to-Chord Ratio
u	m/s	Circumferential Velocity
v	m/s	Absolute Velocity
V	m^3	Volume
w	m/s	Relative Velocity
W	kg	Weight (Mass)
$\dot{W}$	W	Power
w	J/kg	Specific Work
x	m	X-Axis Coordinate
X_T $\%c$	—	Position of Maximum Thickness (Turbine Blade)
Δx	m	Gap/Displacement/Length (Axial Direction)
y	m	Y-Axis Coordinate
z	m	Z-Axis Coordinate
α	rad	Flow Angle, or ...
α	K^{-1}	Coefficient of Thermal Expansion, or ...
α	—	Factor, or ...
α	rad	Shaft Angle
β	rad	Blade Angle, or ...
β	—	Pressure Ratio

Symbol	Definition	Unit
Δ	—	Variation of ...
η	—	Efficiency
γ	—	Ratio of Specific Heats
λ	—	Taper Ratio
μ	—	Empirical Coefficient, Elastic Portion of Deformation Energy
ν	—	Poisson's Ratio
ω	rad/s	Angular Velocity
Ω	RPM	Angular Velocity
ϕ	—	Flow Coefficient
ψ	—	Work Coefficient
Ψ	—	Zweifel Coefficient
Π	—	Pressure Ratio
ρ	kg/m^3	Density
σ	—	Solidity, or ...
σ	Pa	(Normal) Stress
$\delta\sigma$	Pa	Change in Stress
τ	Pa	Shear Stress
θ	rad	Tangent Angle, or ...
θ	rad	(Generic) Angle

SUBSCRIPTS

Subscript	Definition
0	Original/Initial Value
0,1,2,3	Station Numbering
1,2,3,...	Stage Numbering
1,2,3,4,5,6	Stations in Disk Geometry Formulation
2,21,25,3,4,45,5,...	Engine Station Numbering
A, B	Adjacent Infinitesimal Ring Elements of Disk
a	Aircraft (Excluding Usable Fuel), or ...
a	Blade Root Inner Radius
abs	Absolute (Frame of Reference)
airfoil	Airfoil
avg	Average
axi	Axial
bl	Blade(s)
$corr$	Corrected
cas	Casing
cc	Combustion Chamber (Combustor)
cmp	Compressor
con	Containment
d	Deviation (Angle)
des	Design
disk	Disk
dome	Dome
duct	Duct
f	Fuel
fuel	Fuel
G	Centroid / Centre of Mass
h	Hoop/Tangential (Stress), or ...
h	(Blade) Hub
HPC	High-Pressure Compressor

Subscript	Definition
HPT	High-Pressure Turbine
hub	(Blade) Hub
i	Inner, or ...
i	belonging to element/section 'i'
kin	Kinetic (Energy)
LE	Leading Edge
liner	Liner
loc	Local (Spanwise Location)
LPC	Low-Pressure Compressor
LPT	Low-Pressure Turbine
m	Mean/Mid, or ...
m	Meridional
max	Maximum
mech	Mechanical
mid	Mid/Mean (Spanwise Location)
min	Minimum
n	Arbitrary Station Number, or ...
n	Neutral Axis
nominal	Nominal
o	Origin, or ...
o	Outer
obj.	Objective (Function)
op	Operating
out	Outlet
pr	Pressure
pt	Polytropic
R	Residence
r	Radial, or ...
r	Radial-Axis
ref	Reference
rel	Relative (Frame of Reference)
rim	(Disk Outer) Rim
root	(Blade) Root
rotor	Rotor (Row/Blade)
row	Row
s	Static Property (Thermodynamics)
sh	Shaft
sk	Skeleton Line
stator	Stator (Row/Blade)
stg	Stage(s)
t	Total Property (Thermodynamics), or ...
t	Tangential, or ...
t	Thickness
tr	Total Relative Property (Thermodynamics)
TE	Trailing Edge
tg	Tangential
tip	(Blade) Tip
total	Total Value
trb	Turbine
tt	Total-to-Total
U	Upper Surface
UTS	Ultimate Tensile Strength
y	Yield (Stress/Strength)

1

INTRODUCTION

Recently, the focus of research in the field of new aircraft development has been on achieving higher efficiency. As a result, numerous innovative aircraft configurations and engine designs have been proposed. However, these novel architectures still require extensive and thorough feasibility assessment studies to determine with reasonable accuracy their potential. Enhancing aircraft performance is crucial not only for a more sustainable future but also from an economic perspective. Prior to the pandemic-induced lockdowns and border closures in 2020, commercial aviation accounted for approximately 2.1% of global CO2 emissions and 12% of all transport-related emissions (Air Transport Action Group (ATAG) [20]).

The margin of improvement in efficiency of conventional propulsion systems is limited [21]. To achieve lower aircraft emissions, it becomes essential to explore novel engine configurations. One such endeavor is the Airborne Energy Harvesting for Aircraft (ARENA) project [22], led by the Power & Propulsion group at Delft University of Technology in collaboration with multiple OEM's of the aerospace sector. This project aims at developing a pioneering power generation system by, integrating a gas turbine with an organic Rankine cycle system to recover energy from the gas turbine exhaust gases and convert it in additional electric power.

Component weight is a key parameter that profoundly influences aircraft performance. Therefore, when embarking on the design of novel engine architectures, it becomes imperative to precisely estimate their weight. This is vital for a comprehensive understanding of the engine's potential performance.

As of now, there is a lack of publicly available tools that can be used for weight estimation of novel gas turbine-based propulsion systems with the desired level of precision. In response to this gap, the development of a component-based weight estimation tool for aeronautical gas turbine engines has been initiated. The primary objective of this tool is to predict the weight of innovative engine architectures with a reasonable degree of accuracy. This tool serves a crucial role within the ARENA project and will offer an open-source alternative to existing non-publicly available component-based weight estimation tools [23].

This project is about improving and expanding the capabilities of WEST: a component-based weight estimation tool for gas turbine engines developed by I.Boersma[23] during his master thesis project. Currently the program (WEST) is only able to work with axial turbomachinery and still requires as inputs form the user some low-level geometric input parameters of the engine, such as the aspect ratio of the compressor rotor and stator blades.

The project's main objectives are twofold:

- Improving the existing tool by incorporating an automated method to determine the optimal aspect ratio for the blades of each compressor stage. This enhancement seeks to reduce the number of geometric inputs required from the user, making the weight estimation process more efficient and user-friendly.
- Expanding the functionality of the tool by introducing the capability to design and analyze radial compressor stages and other components. This extension will enable effective modeling of small to medium turboshaft engines, the prime movers of the propulsion systems investigated in the ARENA project.

By achieving these goals, the project aims at advancing the state-of-the-art of tools and methods devoted to gas turbine engine weight estimation, facilitating more accurate and comprehensive assessments of novel engine architectures and promoting further advancements in aeronautical engineering.

1.1. COMPONENT-BASED WEIGHT ESTIMATION METHODS

The simplest methods for estimating the weight of turbine engines are based on single-equation models. While these offer great computational efficiency, the simplified nature of the methods severely limits their accuracy and flexibility; furthermore these methods are based on historical data of existing engines, and thus will not be useful while trying to model a novel engine architecture. According to Lolis et al. [24] the accuracy of single equation weight estimation models for turbofan engines varies between ±25% and ±50%, however no such models are available for turboshaft engines.

Component-based weight estimation tools estimate the weight of each engine component separately. These weights are then combined to obtain the weight of the entire engine.

A variety of component-based methods have been developed by many institutions in the past, such as GTlab [25] developed by the German Aerospace Centre (DLR) and ATLAS [26] developed by Cranfield University. The most relevant is WATE++ developed by NASA starting from 1979 with the historically-driven component weight correlations by Onat and Klees [27]. At present, none of these methods are however publicly available.

In summary, the adoption of a component-based approach significantly enhances the versatility of the methodology. Once the methodology is validated against data of existing engines, it can be applied to model innovative engine designs. This approach yields practical, physically-based solutions, even for engines that are entirely new and lack a closely related configuration. Consequently, these methods are applicable not only to the analysis of existing engines but also to the assessment of and emerging technologies.

1.1.1. WEST

WEST is a component-based weight estimation tool developed specifically for gas turbine engines. Its purpose is to *"perform the preliminary sizing of aeronautical gas turbine engines and provide insights into the weight trends concerning power capacity and design parameters like turbine inlet temperature (TIT), overall pressure ratio (OPR), mass flow rate, number of stages, and the chosen turbomachinery configuration (axial, radial, mixed, etc.)"* [23].

The primary goal behind the development of WEST is to enable the estimation of the engine size and weight given the cycle thermodynamic specifications and power capacity and with the minimum information on the engine geometry to be provided by the user.

The WEST tool has been developed by I. Boersma in his thesis project. However, the tool has still some relevant limitations. It can only work with axial compressors and turbines, thus limiting its use primarily to conventional engines. Additionally, certain low-level geometrical inputs are still required from the user.

The objective of this project is to advance the software's capabilities by reducing the number of geometrical input parameters that need to be specified by the user. This enhancement aims to streamline the weight estimation process further and increase the user-friendliness of WEST. Moreover, the project seeks to expand the functionality of the tool to encompass a broader range of engines.

1.2. RESEARCH AIM

The findings reported by I.Boersma [23] show that statistically-derived single-equation weight estimation models lack the required accuracy, sensitivity, and flexibility for novel gas turbine-based propulsion systems, such as those investigated in the ARENA project. While component-based methods offer the needed accuracy, their computational cost hinders their integration into system design and optimization studies.

Since no available tool meets the accuracy requirements, the development of a new component-based preliminary engine design and weight estimation tool became necessary. The developed tool should accurately reproduce existing engine designs for validation, while facilitating the generation of new designs, a key objective of the ARENA project. The success of the tool depends on realistic component designs, as accurate designs lead to reliable weight estimations for the engine as a whole.

The overall aim of the thesis research is to develop a knowledge base and a tool for performing the preliminary sizing of aeronautical gas turbine engines, in particular for small to medium scale turboshaft engines with radial compressor stages, as well as for predicting weight trends concerning power capacity, TIT, OPR, mass flow rate, number of stages, and turbomachinery configuration (axial, radial, mixed, etc.).

A reasonable expectation for the accuracy of the WEST tool, as outlined by I.Boersma [23] in his work, is, however, in the order of $+10\%/-40\%$ of gas turbine engines weight. This level of accuracy is expected to suffice for preliminary design studies of novel (very low TRL) engine concepts.

1.3. IMPACT

The WEST program, as an open-source tool, holds promising potential not only for research endeavors within the TU Delft, such as the ARENA [22] project, but also for researchers worldwide in the field of aeronautical engineering. By providing an accessible and reliable weight estimation tool, it may propel advancements in novel propulsion system modelling and foster global collaborations. The impact of this component-based weight estimation tool is far-reaching, offering valuable contributions to research focused on the design of propulsion systems where engine weight is a critical factor.

Within the ARENA project, both turbofan and turboshaft engines are of importance, with a particular focus on turboshafts. Turboshaft engines are gaining prominence due to their role played in hybrid-electric propulsion, more-electric aircraft, and urban air mobility. However, compared to turbofans, the literature on turboshaft design and weight estimation is relatively limited, lacking methods like the well-established regression equations developed by Greitzer et al. [4] for conventional engines.

The absence of such equations for turboshafts emphasizes the need for a validated, component-based turboshaft design tool like the WEST program. A precise component-based weight estimation tool like WEST can also be used to create a set of regression equations like those discussed earlier that would make the weight estimation of turboshaft engines even more computationally efficient.

Turboshaft engines have many applications in the fields of vertical takeoff and landing aircraft and urban air mobility concepts. Designs such as the large tiltrotor vehicle platforms studied by Snyder et al. [28, 29] as part of the NASA heavy lift rotorcraft systems investigation are some examples. At the same time, different development projects on more-electric aircraftare going on such as the ECO-150 [30] and ONERA's DRAGON [31], both 150 passenger regional airliners, or NASA's N3-X [32], a 300 passenger hybrid wing body. All these designs feature electric or turbo-electric distributed propulsion, where a turboshaft engine is used to generate the electrical power for the aircraft. It is thus clear how these types of project would benefit from the development of a tool like WEST, especially as other tools are not openly available. The current battery technology does not allow for a high enough energy density to make medium range aircraft fully electric. On-board electric power generation will be still required. This task will be most likely carried out by a turboshaft engine.

The aviation industry is witnessing an expanding range of potential applications for turboshaft engines. To continuously advance research in these areas, the development of an engine preliminary design tool is essential. Such a tool is not only vital for analyzing the evolving weight characteristics of the engine itself but also for integration into multidisciplinary, system-level aircraft performance studies. This need is particularly pressing for turboshaft applications, as previously discussed, where a dedicated tool currently does not exist. However, the relevance extends to turbofan engines as well, despite the presence of similar programs.

Many aerospace researchers are currently left with the choice of resorting to lower-fidelity methods or creating their own component-based models, as is the case with this thesis. These limitations either compromise the quality of their specific research or lead to prolonged development and analysis times before useful results can be obtained. Consequently, by open-sourcing the new weight estimation tool, the potential impact of this development effort is greatly amplified.

2

ASPECT RATIO OF AXIAL COMPRESSOR BLADES

WEST is envisioned as a preliminary design and component-based weight estimation method for turbomachinery, which only requires high level thermodynamic and design inputs to achieve its results; as of now, however, in the case of axial compressors, some low-level geometrical inputs are still required by the user.

The aim of this chapter is to research possible ways of automatically determining the optimal aspect ratio for the blades of each axial compressor stage, without relying on values guessed by the user.

Section 2.1 reports a brief overview of the available literature on the design criteria for the choice of the aspect ratio of blades in axial compressors; an analysis was then performed using computational fluid dynamics tools to gain a better understanding of the problem. This analysis is described in sections 2.2 through 2.5.

2.1. BACKGROUND

There is no conclusive information in the literature regarding the criteria for the choice of optimal aspect ratio during the preliminary design phase of the stage of an axial compressor, neither there is information about the relation between the optimal aspect ratio and the duty coefficients and the operating conditions of an axial compressor stage.

Measurements conducted by Britsch et al.[33] and Fahmi [34] stage efficiency reduces by increasing the blade aspect ratio whereas an increase in efficiency is observed by Smith [35] in a similar circumstance.

In the 2003 lecture series from the Von Karman Institute [1] it is suggested that the optimal aspect ratio for a compressor stage may change depending on the work coefficient. In this lecture the author argues that, based on historical data taken from real engines, the trend in modern engines is to have higher pressure ratios across the single stages, thereby reducing the total number of stages in the engine despite the increasing overall pressure ratio.

This can be achieved by increasing either the circumferential speed (U_M) or the work coefficient (Ψ) of the stage, as proven by the following expression of the stage pressure ratio [Eq:2.1]:

$$\Pi_{stage} = \left[\Psi \eta_{is} \left(\frac{U_M}{\sqrt{T_1}} \right)^2 \frac{1}{c_P} + 1 \right]^{\frac{\gamma}{\gamma-1}} \tag{2.1}$$

Where T_1 is the inlet total temperature of the stage.

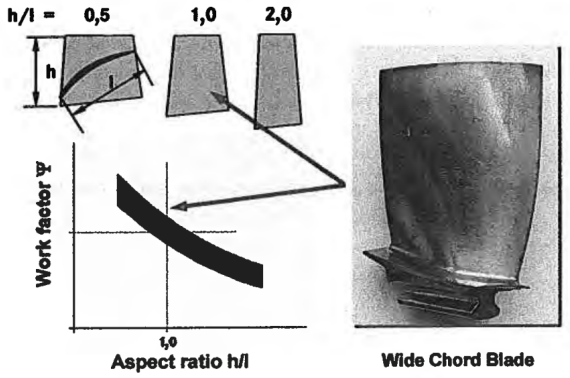

Figure 2.1: Qualitative plot of the correlation between work coefficient and aspect ratio [1]

Since increasing the circumferential speed may cause both structural problems and issues related to supersonic flows, increasing the work coefficient is argued to be the best choice to obtain stages with higher pressure ratios; in presenting this argument the author includes a diagram illustrating a qualitative inversely proportional correlation between the work coefficient and aspect ratio [Fig:2.1]; this suggests that it may be possible to determine the optimal aspect ratio for the blades in a compressor stage based on the duty coefficients and operating conditions alone.

Historical data gathered by Bolam et al.[2] on the evolution of axial compressor geometries in aeronautical engines from 1950 to 1990 show a clear trend in a gradual reduction of the average aspect ratio of compressor blades and an increase of average loading with the introduction of more modern engines, which is aligned with the previously discussed observation presented by Steinhardt [1].

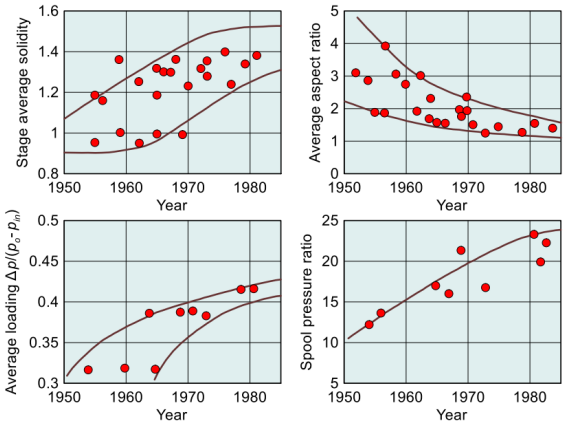

Figure 2.2: The trend in compressor geometry with time [2]

In the paper by To et.al. [3] an in-depth analysis using loss models and CFD is performed on the effect of aspect ratio on performance of so called low-aspect-ratio compressors. The paper also proposes an equation to obtain the optimal aspect ratio as a function of the end-wall loss coefficient (ξ_{ewo}) and the maximum-thickness (of the blade profile) to height ratio of the blades ($\frac{t_{max}}{h}$) [Eq:2.2]; this analysis, however, was done with stage blade counts based on constant solidity, but the method used to determine this solidity (and thus the blade count) is not mentioned.

$$AR_{opt} = \left(\frac{\xi_{ewo}}{k_p \frac{t_{max}}{h}} \right)^{0.5} \tag{2.2}$$

The authors also found that an aspect ratio variation of ±0.1 around the optimum would yield a negligible change in efficiency, meaning that the sensitivity of the performance of the compressor to aspect ratio changes around the optimum is very low.

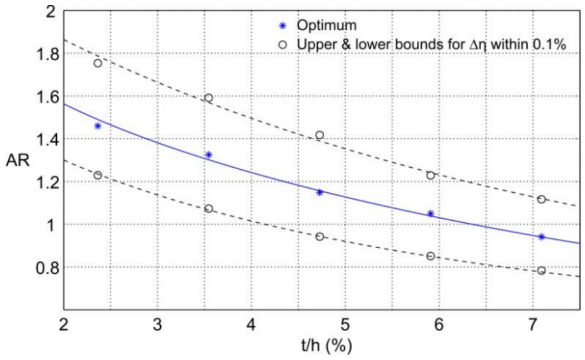

Figure 2.3: Optimal aspect ratio variation with thickness-to-height ratio [3]

In the study conducted by Greitzer et al. [4] on the weight estimation of engine designs using WATE++, the component-based weight estimation tool developed by NASA, the authors rely upon an empirical correlation based on data from existing engines to determine the stage aspect ratio based only on the height of the blades. Thus the aspect ratio only varies with the size of the engine [Fig2.4].

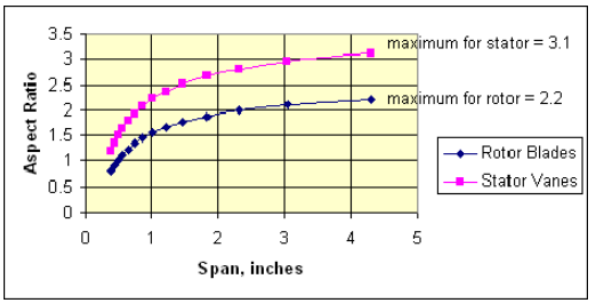

Figure 2.4: Compressor aspect ratio variation with span from Greitzer et al. [4]

Peters et al. [36] conducted a numerical study on the influence of compressor blade aspect ratio on profile and secondary loss of an axial compressor stage and developed a new analytical model for these losses that shows how increasing the aspect ratio while maintaining constant blade solidity and height causes an increase in the profile losses while secondary losses decrease. This data shows the same trend reported in the paper by To et al. [3] discussed earlier. The authors do not provide a general correlation, but the trend in the loss components suggests that a point of minimum losses can be found.

The aim of this study is to use the data available from these studies in combination with a series of CFD simulations todefine guidelines regarding the choice of the blade aspect ratio for compressor stages. This knowledge may then be used to implement a simplified method to automatically determine the aspect ratio in WEST without resorting to any input from the user.

2.2. ANALYSIS PROCEDURE

Based on the literature summarized above, especially the 2003 lecture series from the Von Karman Institute [1], it is expected that i would be possible to find a correlation between the optimal aspect ratio for the rotor and the stator of an axial compressor stage based only on the duty coefficients (with emphasis on the work factor Ψ) and the operating conditions. This would make it possible to automatically determine the optimal aspect ratios for a stage within WEST based on already the value set for the design variables of the stage without having to rely upon additional user inputs.

In order to investigate the existence and the physical basis of this trend, it was chosen to proceed with a series of CFD simulations on an exemplary compressor stage, following the procedure outlined in Figure 2.5, to observe how the optimal aspect ratio varies while changing other design inputs of the stage.

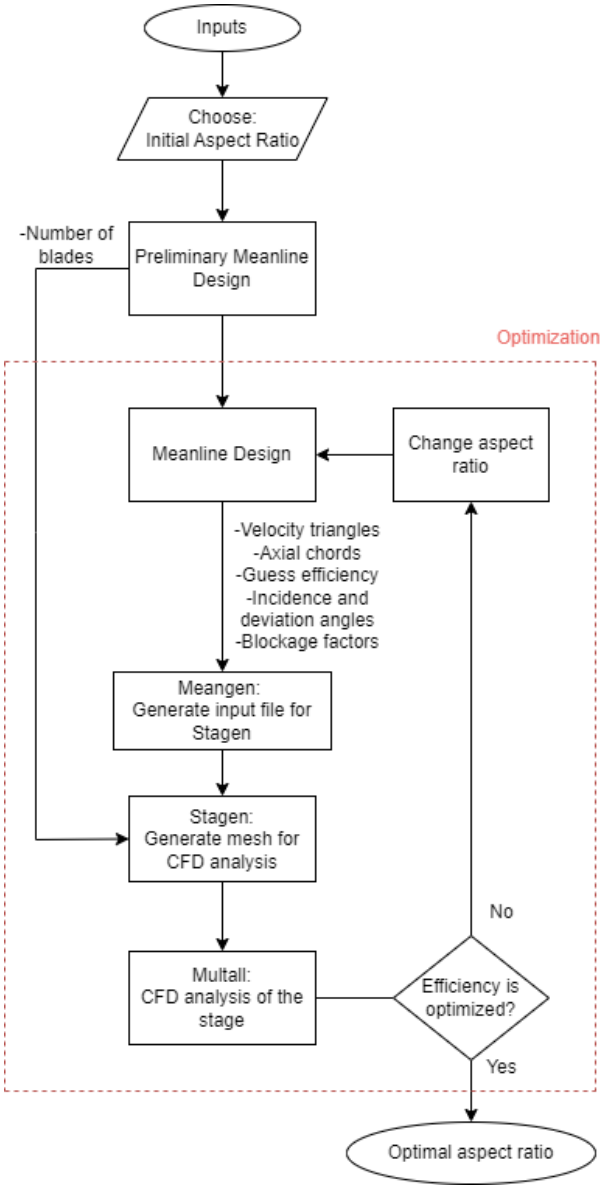

Figure 2.5: Flow chart of the optimization procedure

2.2.1. CFD - BASED APPROACH

The literature, specifically the information provided by Peter et al. [36] and E.Steinhardt [1] suggests that it is possible to find a correlation between the duty coefficients of a compressor stage and the optimal aspect ratio.

To identify this correlation, a set of gradient-based optimizations of the aspect ratio will be performed for an exemplary axial compressor stage, one for each combination of duty coefficients. This optimization process study makes use of a CFD model to predcit the flow through the stage and the estimate of the polytropic efficiency. The use of CFD analysis is preferred over simplified methods that rely on loss models, as it ensures the best possible accuracy of the results. It should be noted that in low aspect ratio configurations, loss models may not be able to accurately predict profile and endwall losses [3].

If the simulation results are deemed satisfactory and a clear correlation between the studied input parameters (blade count, work coefficient, flow coefficient) and the optimal aspect ratio is observed, the data obtained from these simulations could be utilized to generate Smith-like maps to be used within WEST.

Smith charts are graphical representations that allow for the prediction of compressor stage efficiency based on the stage's duty coefficients. These charts plot the compressor's pressure ratio, flow coefficient, and efficiency onto a single graph, allowing for quick and easy estimation of the stage's performance [37]

2.2.2. GEOMETRY GENERATION BASED ON MEANLINE DESIGN

To investigate the relationship between the design variables and the optimal aspect ratio, a meanline design code was created using MATLAB following the same approach used in WEST by I. Boersma for axial machines [23]. The MEANGEN meanline design tool was used to translate the designed flow path geometry in a format that was then meshed using STAGEN. Finally, the resulting mesh was fed into the CFD solver MULTALL to obtain the stage efficiency.

MEANGEN is a mean-line code used for turbomachinery design, and its results represent the input data for STAGEN and MULTALL [38]. Although it can function as a standalone design code, in this work, it is used to convert the data of the compressor stage designed by the MATLAB-based mean-line code into a format that can be read by STAGEN. STAGEN, on the other hand, is a package used for generating blade geometry, and its output can be used in the 3D, multistage, turbomachinery flow calculation program MULTALL [39, 40].

The use of Matlab as programming language for implementing the optimization procedure offers several benefits, such as the utilization of the fmincon gradient-based multidisciplinary optimization package. Additionally, a method for interfacing Matlab scripts with MULTALL and its software package has already been developed during the turbomachinery course, which can be easily adapted for the problem at hand.

Once all the design parameters of the compressor stage are set through the meanline design, a gradient-based optimization of the polytropic efficiency of the stage can be performed to find the optimal aspect ratio. The efficiency of a particular stage configuration is determined by running a CFD simulation of the stage using MULTALL.

2.2.3. CFD ANALYSIS

MULTALL is a tool used for 3D flow calculations that was specifically developed for turbomachinery. It has been continuously developed over several years and includes options to model the most common flow features found in turbomachines. It can be used to predict the flow through axial flow machines and provides detailed information on the machine's efficiency, mass flow, pressure ratio, and flow field.

MULTALL was selected for this study because it is faster than most other CFD codes. It can produce relatively accurate results in a relatively short time (10-15 minutes for a single stage) [40] on a conventional laptop. Additionally, the software package consisting of MULTALL, MEANGEN, and STAGEN is designed to work together, simplifying the setup of the optimzation study.

The initial simulations were conducted to determine the design variables that have the most significant impact on the optimal aspect ratio, which are expected to be the flow coefficient and work factor based on Refs [3, 36].

It is important to notice, as clearly visible in the flow chart provided in Figure 2.5, that the number of blades for the stage is determined outside of the optimization loop, This means the number of blades is kept constant during the whole optimization.

2.2.4. BLADE NUMBER

The meanline code requires the aspect ratio of the stage as an input for determining the number of blades, as it uses the same procedure as used in WEST [23], where the optimal number of blades for the rotor and the stator of the stage is calculated based on the velocity triangles, the hub and tip radii and the axial chord of the blades:

$$N_{B,rotor} = f(W_1, W_2, c_{axi}, r_{tip}, r_{hub}) \tag{2.3}$$

$$N_{B,stator} = f(V_2, V_3, c_{axi}, r_{tip}, r_{hub}) \tag{2.4}$$

Given that the velocity triangles and the radii can be completely derived from the duty coefficients and inlet flow characteristics, which are already required inputs of the design procedure, equations 2.3 and 2.4 can be re-written as follows.

$$N_{B,-} = f(inputs, AR) \tag{2.5}$$

$$inputs = (\phi, \Psi, R, \Omega, p_0, T_0, U_{m,max}) \tag{2.6}$$

The axial chord can be expressed as

$$c_{axi} = \frac{b_{avg}}{AR_{axi}}, \; AR_{axi} = f(AR, \theta_s) \tag{2.7}$$

where θ_s is the bade stagger angle, which can be derived based on the inputs alone.

It is thus clear how the number of blades, being a finite integer, may interfere with the gradient-based optimization of the aspect ratio, as each analyzed aspect ratio may lead to a different optimal number of blades, severely impacting the convergence of the optimization and the significance of the results; for this reason, the number of blades is determined based on a first guess of the aspect ratio at the beginning of each optimization, and the optimization is repeated for different blade numbers.

In the following sections it will be shown how this interdependence between the number of blades and the aspect ratio make it difficult define guidelines for the choice of the aspect ratio of the blades.

2.2.5. INPUTS

The inputs needed to determine the geometry of the stage are listed in Table 2.1. Most of the inputs values are defined in the same way as in the WEST [23] meanline design code for axial compressors. The main differences lie in the pressure rise through the stage (either provided by specifying the outlet pressure or the stage pressure ratio in WEST) which is in this case derived based on the maximum circumferential speed and the work coefficient using equation 2.1. The number of blades of the two rows is specified in place of the aspect ratios for the reasons discussed in section 2.2.4.

Duty Coefficient	**Unit**	**Description**
ϕ	[-]	Flow coefficient, v_m/u
ψ	[-]	Work coefficient, $\Delta h_{t,ad}/u^2$
R	[-]	Degree of reaction, $\Delta h_{rotor}/\Delta h_{t,ad}$
Thermodynamic	**Unit**	**Description**
$\dot{m}_{air}$	[kg/s]	Mass flow rate
Ω	[RPM]	Rotational speed
p_0	[Pa]	Inlet pressure
T_0	[K]	Inlet temperature
$U_{m,max}$	[m/s]	Maximum circumferential speed
Geometric	**Unit**	**Description**
$N_{B,rotor}$	[-]	Number of rotor blades
$N_{B,stator}$	[-]	Number of stator blades
$(t_{max}/c)_{rotor}$	[-]	Rotor maximum thickness-to-chord ratio
$(t_{max}/c)_{stator}$	[-]	Stator maximum thickness-to-chord ratio

Table 2.1: Input parameters for the stage design

2.3. OPTIMIZATION CASE STUDIES

The objective of the analysis is to understand what effect the different design parameters have on the optimal aspect ratio of the rotor and stator blades of an axial compressor stage.

To accomplish this a series of optimizations, as described in section 2.2 were performed on the same compressor stage, varying the design parameters one by one. A total of 220 different optimizations were run, resulting from the combination of 10 different values of work coefficients, which linearly varies between 0.35 and 0.45, 2 values of flow coefficients and 11 values of blade numbers. All the input parameters for the compressor stage are reported in Table 2.2.

Duty Coefficient	Unit	Value
ϕ	[-]	0.5 – 0.6
ψ	[-]	0.35 – 0.45
R	[-]	0.5
Thermodynamic	**Unit**	**Value**
$\dot{m}_{air}$	[kg/s]	20
Ω	[RPM]	10000
p_0	[Pa]	100000
T_0	[K]	296
$U_{m,max}$	[m/s]	250
Geometric	**Unit**	**Value**
$(t_{max}/c)_{rotor}$	[-]	0.1
$(t_{max}/c)_{stator}$	[-]	0.075

Table 2.2: Parameters used for the analysis

As discussed in section 2.2.4, the blade number sets were generated following the same procedure as in WEST, for a range of different first guess aspect ratios (AR_0) varying between 2 and 3.25. The different values of flow and work coefficients influence the blade number estimation, so the blade number sets were all calculated using $\psi = 0.35$ and $\phi = 0.6$ and kept consistent between all optimizations.

Typically, the aspect ratio for axial compressor blades lies between 1.5 and 3.5 [41] so the range of AR_0 values used were chosen within this range. The corresponding blade numbers used for the analysis are reported in Table 2.3.

AR_0	$N_{B,rotor}$	$N_{B,stator}$
1.500 [a]	21	44
2.000	27	58
2.125	29	62
2.250	31	66
2.375	32	69
2.500	34	73
2.625	36	76
2.750	37	80
2.875	39	84
3.000	41	87
3.125	42	91
3.250	44	94

[a] Data calculated only for $\phi = 0.6$

Table 2.3: Sets of blade numbers used for the analysis

The range of work coefficients, flow coefficients and aspect ratios to be used in this analysis was chosen based on typical values found in axial machines for aeronautical applications as per the lecture slides of the AE turbomachinery course [19] and the books by P.P.Walsh and P.Fletcher[41], and M.Gambini and M.Vellini [5].

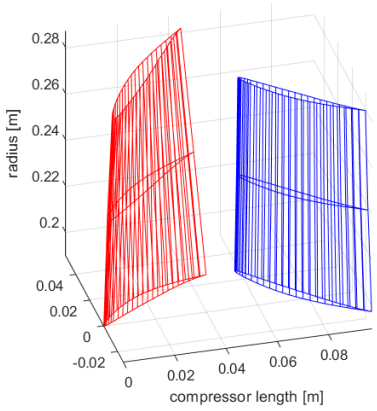

Figure 2.6: 3D plot of the compressor blades with AR = 1.5, rotor in red, stator in blue

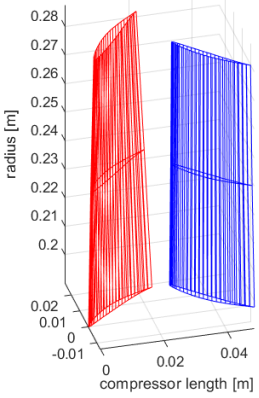

Figure 2.7: 3D plot of the compressor blades with AR = 3, rotor in red, stator in blue

Figures 2.6 and 2.7 are examples of the 3D geometry of the compressor blades analysed in this study, with two very different values of aspect ratio. Note that, as the blade heights and metal angles are the same for both stages, changing the aspect ratio only implies a change of the chord of the blades, and, as the maximum-thickness-to-chord ratio is kept constant, the maximum thickness is changed as well.

2.3.1. OPTIMIZATION STRATEGY

While performing the optimizations described in the previous section, it was quickly realized that the efficiency of the stage would always follow the same trend with respect to the aspect ratio, if the number of blades is fixed. This trend is the same as reported by To et al. [3].

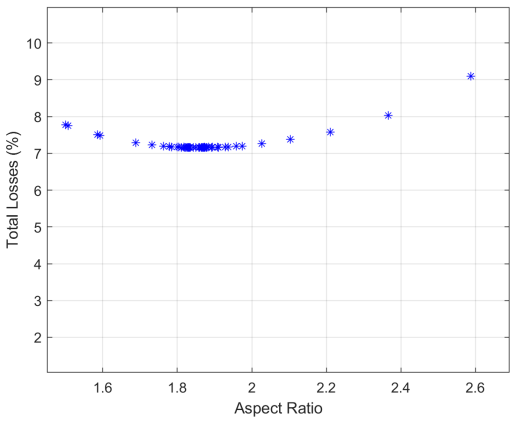

Figure 2.8: Set of aspect ratios analysed as part of one of the optimizations ($\psi = 0.35$, $\phi = 0.6$, $AR_0 = 1.5$)

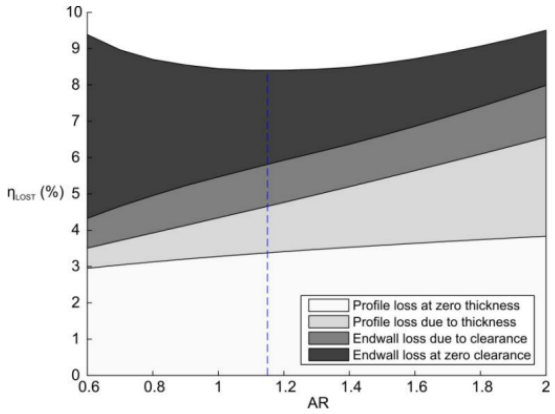

Figure 2.9: Trend of stage efficiency with blade aspect ratio by To et al. [3]

In order to increase the computational efficiency and decrease the required time for each optimization, an alternative to the gradient-based method was implemented; for each inputs set, the stage efficiency is calculated for seven equally spaced values of the AR. The results are then fitted with a fourth degree polynomial. The optimum AR is determined by identifying the minimum of the fitted curve, lowering in this way the number of CFD simulations needed to optimize the AR, from more than 30 to only 7.

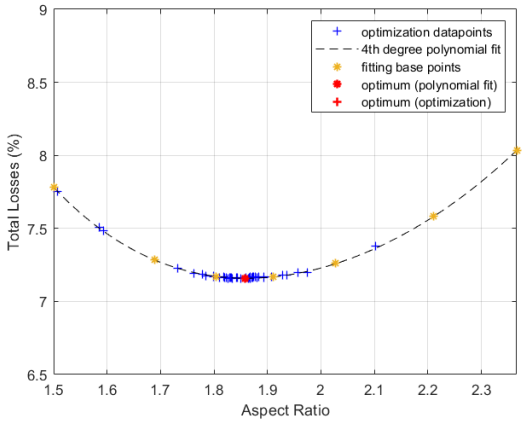

Figure 2.10: Comparison of the results obtained with the full optimization method and the fitting of seven data points with a forth degree polynomial

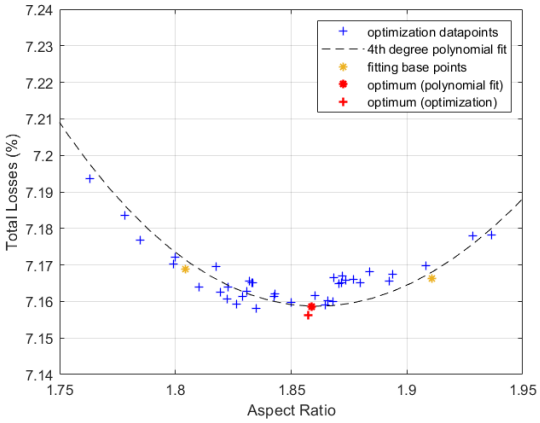

Figure 2.11: Comparison of the results obtained with the full optimization method and the fitting of seven data points with a forth degree polynomial (zoom-in close to the optimum)

As can be observed from figures 2.10 and 2.11, the efficiency variation for values of aspect ratios of 1.8 and 1.9 is less than 0.02% which is in accordance with the conclusions provided by To et al. [3]. This low variation makes it harder for a gradient-based optimizer to pinpoint an optimum due to the numerical noise in the points close to the optimum, as clearly visible in figure 2.11.

The solutions provided by these methods have for this reason a margin of uncertainty in the optimal AR of ±0.1, as in this range the efficiency variation is so low, such an uncertainty has low impact on the design of the stage.

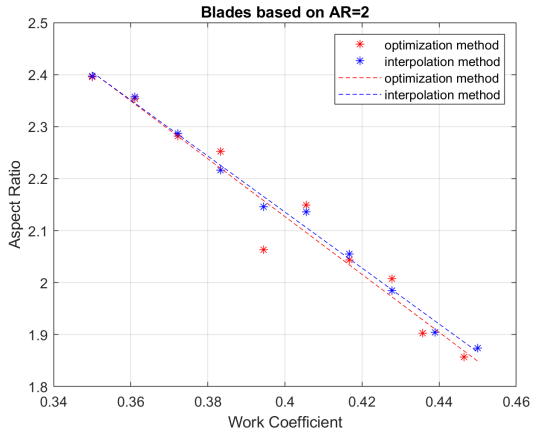

Figure 2.12: Optimal aspect ratio results of the gradient based optimization (optimization method) and the polynomial fit (interpolation method)

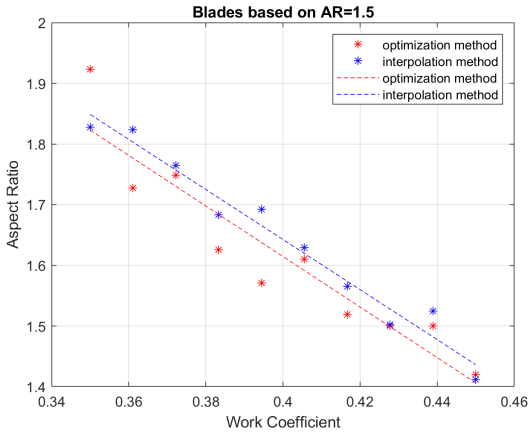

Figure 2.13: Optimal aspect ratio results of the gradient based optimization (optimization method) and the polynomial fit (interpolation method)

As can be seen in figure 2.12 and 2.18 the results obtained with the two methods match well: except in one case, the optimal aspect ratio values are always within 0.1 of each other.

The optimal values obtained through the fitting of polynomials follows a linear trend more closely, and the optimal aspect ratios are less spread out compared to the gradient-based optimization results. The match between the gradient based optimization results and the polynomial fit was also found to be closer for higher aspect ratios, as the scatter of the efficiencies close to the optimum point was found to be lower in those cases.

The results shown in the following sections were all obtained using the polynomial fitting method as it provides the same quality of results of the gradient based optimization method, but with a fraction of the computational requirements.

2.4. RESULTS

Here are reported the plots showing the results obtained for a value of the flow coefficient of 0.5 and 0.6 when the work coefficient is varied between 0.35 and 0.45.

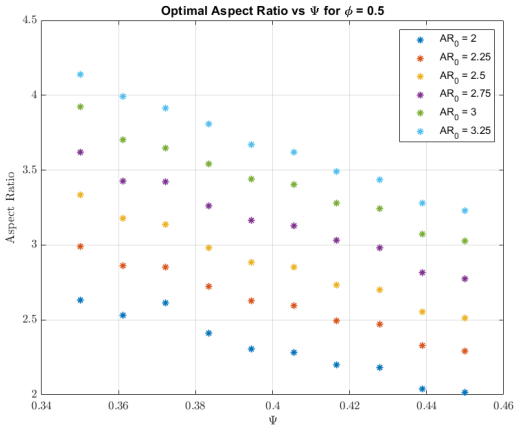

Figure 2.14: Optimal aspect ratio results for the set of optimizations for $\phi = 0.5$

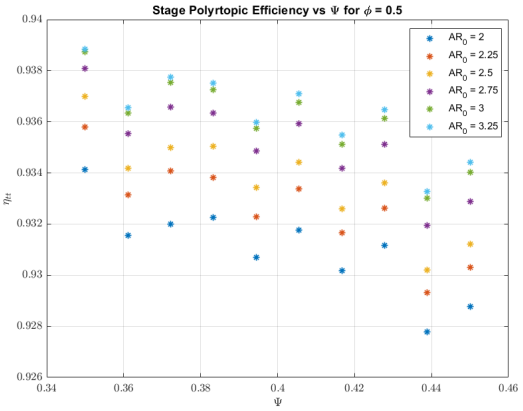

Figure 2.15: Efficiencies corresponding to the optimal aspect ratio results for the set of optimizations for $\phi = 0.5$

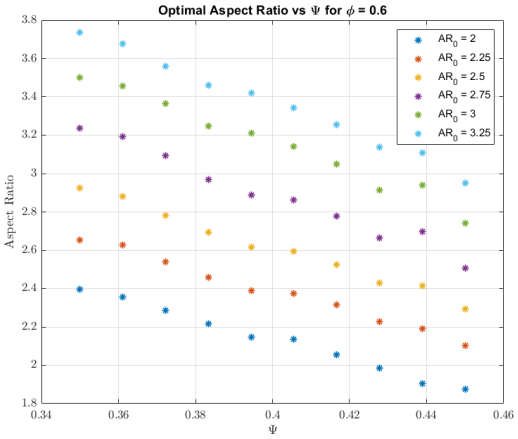

Figure 2.16: Optimal aspect ratio results for the set of optimizations for $\phi = 0.6$

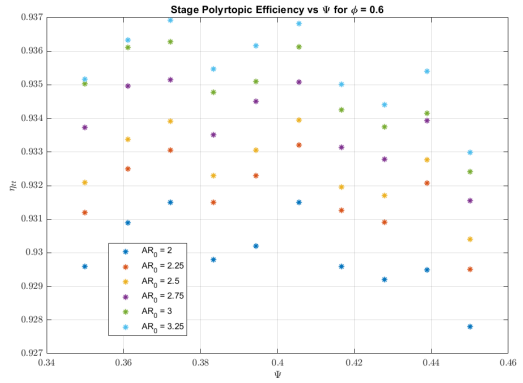

Figure 2.17: Efficiencies corresponding to the optimal aspect ratio results for the set of optimizations for $\phi = 0.6$

The results clearly follow the same trend described in the 2003 lecture series from the Von Karman Institute [1]: for higher work coefficients the optimal aspect ratio is lower, but if the number of blades is allowed to vary, then the trend in efficiency clearly shows how the highest efficiencies are reached for higher blade counts and aspect ratios. Moreover, the optimal aspect ratio increases with the number of blades.

2.4.1. MEANLINE-BASED LOSS MODELS

Meanline loss models can be used to evaluate a preliminary loss breakdown and have a better idea of the variation of the stage efficiency with respect to the aspect ratio. The results obtained by applying these models will inevitably be less accurate than a CFD simulation, but they can give a rough estimate of how the individual losses vary with respect to the aspect ratio.

The set of loss models provided in the book by M. Gambini and M. Vellini [5] was implemented in the available meanline design code and used to repeat the alanyses already done using CFD. This is the most cohesive and complete set of loss models for axial compressors found in the available relevant literature.

The analysis based on the meanline code was found to give similar results to the CFD simulations both in terms of optimal aspect ratios and efficiency, as shown in the following.

The calculation procedure starts by estimating a first guess of the stage efficiency based on the Smith charts. The thermodynamic states of the stage are then computed based on this first guess and from these values the

total pressure losses (equations 2.8 to 2.10) are then determined with the set of loss models. Then all pressure losses and the thermodynamic states of the stage are re-calculated to determine a new value for the efficiency.

$$Y_{tot,R} = \frac{p_{1tr} - p_{2tr}}{p_{1tr} - p_1} \tag{2.8}$$

$$Y_{tot,S} = \frac{p_{2t} - p_{3t}}{p_{2t} - p_2} \tag{2.9}$$

$$Y_{tot,-} = Y_p + Y_s + Y_{ew} + Y_{shock} + Y_{TC} \tag{2.10}$$

This procedure is iterated until the calculated efficiency converges and the pressure ratio matches the design value. The pressure losses are split by this method into 5 main contributions: profile losses, secondary losses, endwall losses, shock losses(only calculated if the flow becomes supersonic at any point) and tip clearance losses; the full set of loss models is provided in appendix A.

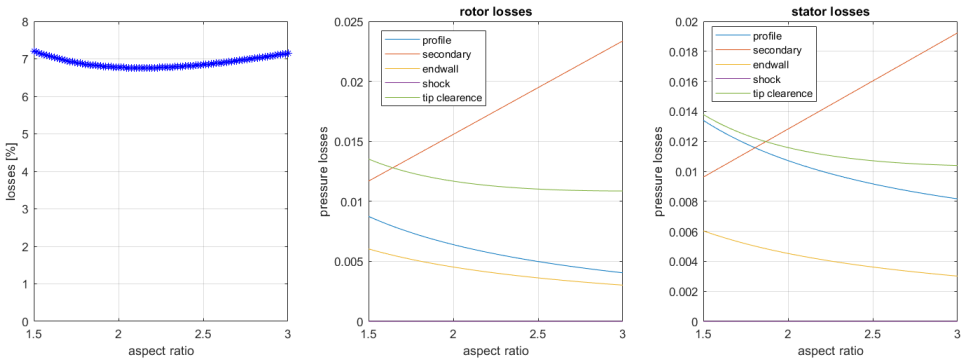

Figure 2.18: Breakdown of the loss contributions obtained with the set of loss models

The trend shown in Figure 2.18 (in this case for a starting aspect ratio $AR_0 = 1.5$) is the same as obtained with CFD, and the loss breakdown matches the findings by Peters et al. [36]. Increasing the aspect ratio increases the secondary losses while decreasing profile and endwall losses even though, differently from Ref [36], the constant solidity condition is not imposed in this case but the number of blades is kept constant. So it is expected that the secondary losses have a faster growth, as solidity decreases with an increase of aspect ratio.

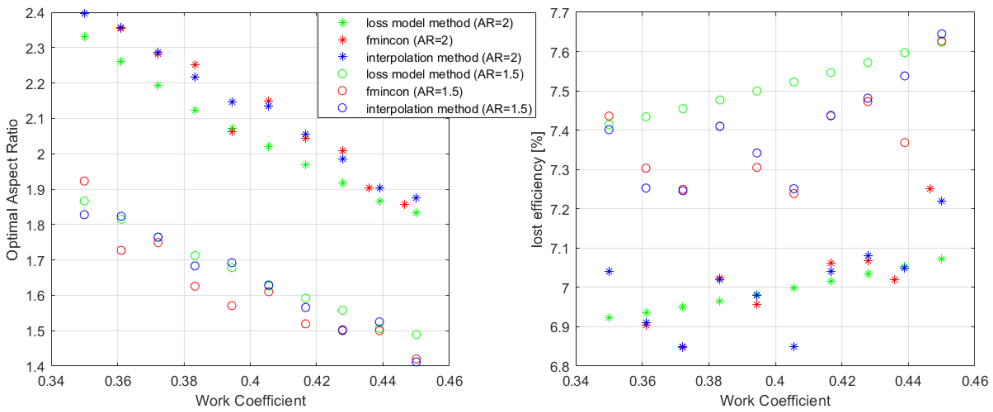

Figure 2.19: Plot of the optimal aspect ratios and corresponding efficiencies obtained with the gradient based optimization, polynomial fit and loss models

Figure 2.19 shows also that very similar results in terms of optimal aspect ratio and efficiency trends can be achieved using just meanline based loss models compared to the results obtained using CFD.

2.4.2. DISCUSSION

Given the results from the literature and from the analyses described above, the choice of optimal aspect ratio for the blades of an axial compressor row cannot be reduced to a simple procedure. It is apparent that the efficiency of the stage is not the only figure of merit for the choice of an 'optimal' value of aspect ratio.

The same clear trend between aspect ratio, number of blades and efficiency was found when both CFD and meanline based loss models are used to compute the stage efficiency; if the number of blades is fixed, this trend that matches what was reported by Peters et al. [36] and To et al.[3] which were considering stages with fixed solidity. However, fixing the solidity of a stage in place of the number of blades has the same effect of fixing the number of blades, because the three parameters (blade count, solidity, aspect ratio) are interlinked in such a way that if two of them are set, the third is automatically determined.

It is also worth observing how the aspect ratio of the blades influences other important aspects in blade design, such as the stress at the blade root (which also directly influences the design of the disk). This has been evaluated for the whole range of analysed aspect ratios using the same procedure currently in use in WEST for disk design of axial turbomachinery.

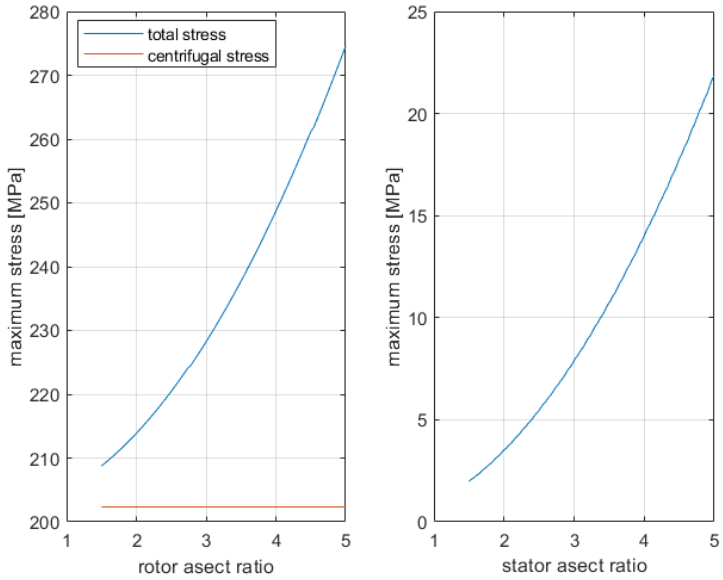

Figure 2.20: Effect of aspect ratio on blade root stress if the number of blades is calculated based on aspect ratio

The thickness-to-chord ratio of the blades is kept the same for all aspect ratio configurations, while the height of the blade is fixed by the stage thermodynamics. The chord of the blades is then calculated using the aspect ratio. Assuming that the effect of the twist of the blades on blade volume is negligible, the ratio between the area of the blade root and the volume of the blade is kept the same for all aspect ratios. Thus the centrifugal stress at the blade root stays constant.

The stress caused by blade loading, however, grows with the aspect ratio; this is due to the choice of keeping the thickness-to-chord ratio constant: increasing the aspect ratio while maintaining the height of the blade constant effectively reduces the chord, and so the thickness of the blade. Thinner blades are then more affected by aerodynamic loads. It is evident from what can be seen in figure 2.20 that the impact of aspect ratio on structural loads is significant, but this effect is limited to the blade itself as the centrifugal force is not affected.

The core of the problem lies in the strong coupling that the optimal aspect ratio has with the solidity/number of blades of the stage. Thus, if only aerodynamic aspects are concerned, the optimal solution is to have "infinitely many, infinitely thin" blades. In all examined cases the solution was found to tend towards that limit, even though the difference between the maximum and minimum measured efficiencies is less than 1% and the variation in efficiency is very low (figures 2.15 and 2.17); most likely structural and manufacturing limitations dictate the limits the choice of aspect ratio, as well as off design performance. Based on a very rough estimation of the stresses involved, the structural limitations seems arguably associated to vibrations and fluid-structure interactions, which cannot be thoroughly evaluated during preliminary design.

The results obtained using a set of meanline-based loss models show that, if a method is found to estimate the optimal solidity / number of blades for the stage regardless of the aspect ratio of the blades, then these loss models can be used to determine the optimal aspect ratio with a reasonable degree of precision.

At the preliminary design stage of an axial compressor, an acceptable value of the solidity of the blades can be obtained from the velocity triangles using the criterion proposed by Lieblein [42, 19]. This criterion is based on the fact that the boundary layer momentum thickness to blade chord ratio stabilizes close to its minimum value for global diffusion factors (DF) below 0.45; where the global diffusion factor is defined in Equation 2.11.

$$DF = \left(1 - \frac{\cos(\beta_1)}{\cos(\beta_2)}\right) + \frac{\cos(\beta_1)}{2\sigma}(\tan(\beta_1) - \tan(\beta_2)) \tag{2.11}$$

$$\sigma = \frac{\cos(\beta_1)}{2DF - 2\left(1 - \frac{\cos(\beta_1)}{\cos(\beta_2)}\right)}(\tan(\beta_1) - \tan(\beta_2)) \tag{2.12}$$

If $DF = 0.45$ is assumed, then the blade solidity can be obtained from Equation 2.12, and the aspect ratio can be optimized maintaining a fixed value for the solidity. The design of the compressor stage was repeated using the operating conditions listed in Table 2.2 and the solidity computed with Lieblein's criterion; the results are shown in Figure 2.21.

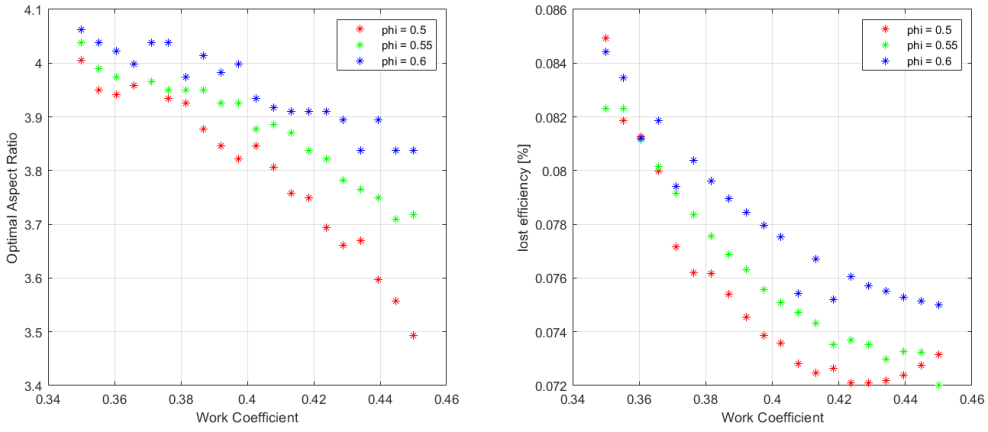

Figure 2.21: Optimal aspect ratio if solidity is determined through Lieblein's criterion.

The efficiency of the stage used to determine these optimal aspect ratios was computed using the previously discussed set of loss models. The trend of the optimal aspect ratio with a variation in work coefficient, as can be clearly seen in Figure 2.21, matches the trend presented by Steinhardt [1].

The computed stage losses for all the optimum points in Figure 2.21 are about 15% (1% of the total stage efficiency) higher than what was obtained for the highest efficiency configurations when the aspect ratio was varied independently from the blade number (see Figures 2.15 , 2.17 and 2.19).

2.5. CONCLUSIONS

A brief literature review was conducted to explore the possibility of determining the optimal aspect ratio of an axial compressor stage given its operating conditions and duty coefficients. No general consensus on this topic was found during the review, but some semi-empirical methods, such as those proposed by By Greitzer et al. [4] and To et al. [3] were found.

It was hypothesized that the work coefficient of the stage may have a correlation with the optimal aspect ratio based on what was reported by E.Steinhardt [1]. This is also suggested by observing the historical trend in axial compressors, which sees an overall increase in work coefficient and decrease in aspect ratio the more modern the machines [2]. This hypothesis was tested by conducting a series of CFD-based optimizations using the MULTALL[40] software on a sample compressor stage varying flow coefficient, work coefficient and number of blades.

Through these simulations it was possible to reproduce the trends shown in the aforementioned sources, and a better understanding of the effects influencing the optimal aspect ratio of compressor blades was obtained.

A strong connection between the aspect ratio and the solidity/number of blades in the stage was observed. Consequently, when solely considering aerodynamic factors, the most optimal solution tends towards a configuration with many extremely thin blades. However, the difference between the highest and lowest recorded efficiencies calculated in this study is less than 1%, and the efficiency variation is quite minimal. It is most likely the constraints related to structural and manufacturing considerations determine the choice of the aspect ratio, as well as the performance under off-design conditions.

An initial estimation of the stresses at the blade root suggests that structural limitations are potentially linked to issues such as vibrations and interactions between the fluid and the structure, which cannot be comprehensively assessed during the preliminary design phase of the compressor.

A possible solution to decouple the choice of the aspect ratio and the solidity/number of blades in the stage is offered by the criterion proposed by Lieblein [42, 19]. This criterion can be used to estimate the optimal solidity of the stage based only on the velocity triangles if an assumption is made about the diffusion factor of the blade rows. By using this method it was possible to reproduce the trend presented by Steinhardt [1]. However, the calculated efficiency for the optimal aspect ratio configurations obtained with this method was lower than what was estmated when the aspect ratio was varied independently of the solidity/ blade count.

Further studies on how Lieblein's criterion can be used in conjunction with meanline-based loss models to estimate the optimal aspect aspect ratio are very likely to yield promising results for the future development of the WEST tool. If properly validated by comparing the obtained designs with existing engines, this method may be implemented in WEST to estimate the aspect ratio of axial compressor stages without requiring additional user inputs.

As discussed earlier the height of the blades is determined given the thermodynamic conditions of the stage. This means that a variation of aspect ratio is effectively a variation of the blade true (and thus also axial) chord; this would heavily impact the design of the rotor disk, which would need to be much thicker in case of axially longer, thicker and heavier blades, as also stated by Steinhardt [1]. The number of blades also interacts with the disk design by changing the centrifugal force at the rim, as a higher blade count will increase the mass of the rotating assembly, requiring stronger disks.

A further investigation of this effect was not conducted in this study, and represent an interesting opportunity for a future work.

3

MODELLING OF RADIAL COMPRESSORS

Compressors, combustors, and turbines enable the implementation of the Brayton cycle. Large turbofan engines employ turbomachinery to handle large mass flow rates, while smaller turboshafts achieve compression through axial, radial, or mixed turbomachinery configurations.

Turbomachinery significantly contributes to the total engine weight, making the design of these components crucial for overall weight estimation. Representative designs of blades, disks, and casings are essential to achieve accurate weight estimates. This chapter's objective is to describe the methodology used in the design of radial compressor stages.

The deign procedure of a radial compressor stage involves three key components: the flow path (blades and diffuser vanes), the disk, and the casing.

The chapter is structured as follows: section 3.1 explains in detail how the aerodynamic and thermodynamic design of a stage is executed, section 3.2 describes the method used to model the compressor disks, while the simplified stress analysis methodology that was developed for this purpose is discussed in section 3.3. Finally section 3.4 reports how the casing of a stage is designed.

3.1. FLOW PATH DESIGN

The implemented flow path design procedure follows the methodology described by M. Gambini and M. Vellini [5], which is largely based on the work by R.H. Aungier [43]. The authors provides a comprehensive guide for the initial fluid-dynamic design of radial compressor impellers and diffusers. This procedure covers all the main design steps, from the preliminary evaluation of the thermodynamic quantities across the stage to blade geometry design.

3.1.1. MEANLINE DESIGN

The implemented meanline code (flow chart presented in Figure 3.1) mainly follows the procedure detailed by M. Gambini and M. Vellini [5] and R.H. Aungier's [43]. The procedure is based upon two nested iterative loops: one to determine the efficiency of the stage through loss models and one to ensure that the effective total-to-total pressure ratio of the compressor meets the design specification.

Unless the efficiency of the machine has been previously calculated through other means (for example based on empirical data for similar machines or charts like the ones available in the paper by Lou et al. [44]), the only way to preliminarily estimate the efficiency of a radial compressor without using computationally heavy methods like CFD simulations is to use loss models. The meanline design requires the efficiency of the machine as input. So if the total-to-total efficiency is not provided, a first guess value is set for the first design iteration. Subsequently, the efficiency is calculated with a set of loss models to be then fed back into the design procedure until the calculated efficiency matches the one of the previous iteration.

The second iteration loop is required because the total-to-total pressure ratio of the compressor computed after the meanline design is completed is often lower than the input value used for the design due to the fluid slip at the outlet of the impeller. To solve this issue, it is sufficient to iterate the procedure by changing the input pressure ratio in order to match the design output to the desired value.

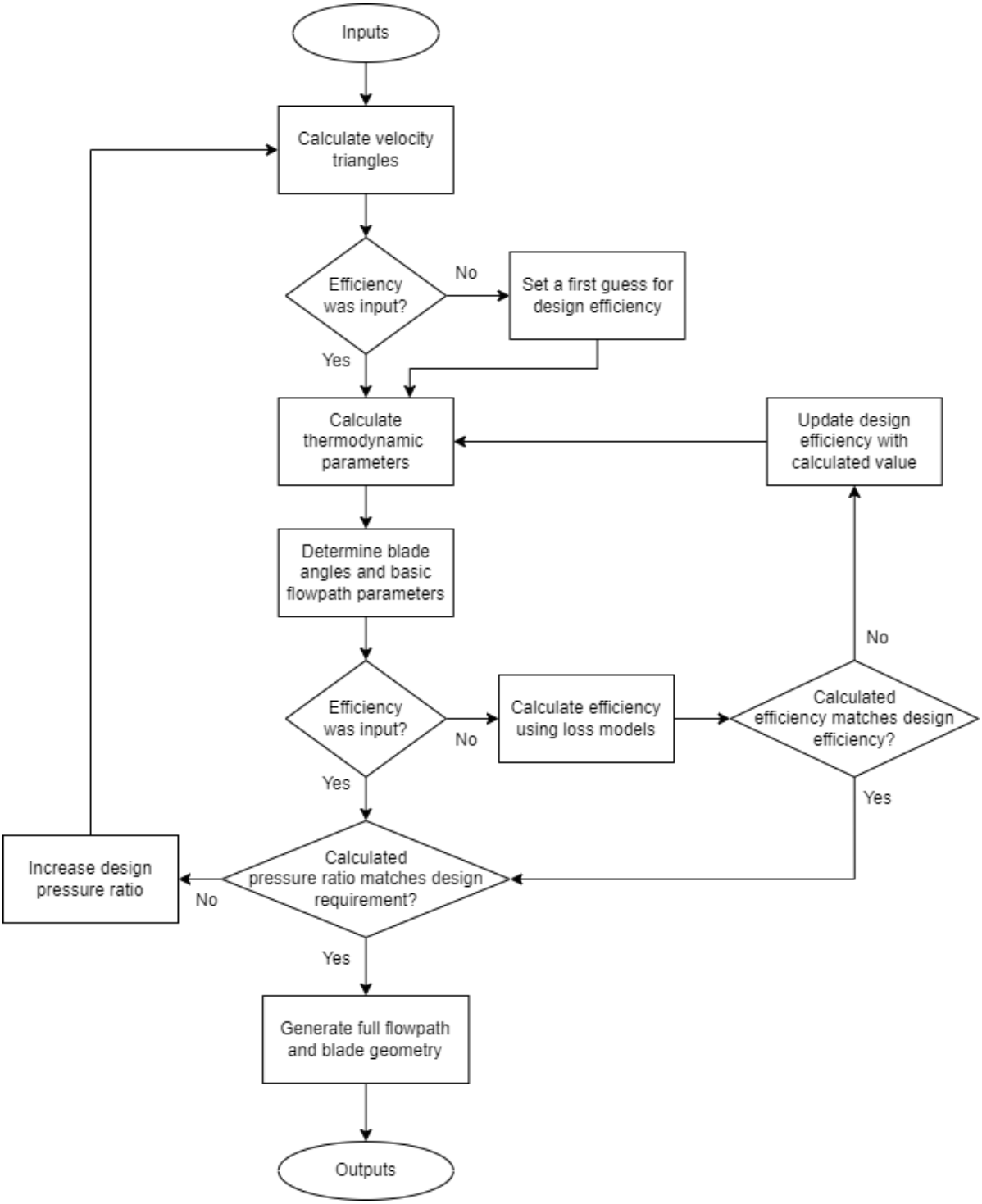

Figure 3.1: Meanline design flowchart

3.1.2. INPUTS

The inputs required for the meanline design (Table 3.6) of the flow path of the radial compressor stage can be divided into three categories: duty coefficients, thermodynamic parameters, and geometric parameters.

Duty Coefficient	Unit	Description
ϕ	[-]	Flow coefficient
ψ	[-]	Work coefficient
R	[-]	Degree of reaction
Thermodynamic	**Unit**	**Description**
β_{tt}	[-]	Total to total pressure ratio, p_{1t}/p_{3t}
α_1	[rad]	Rotor inlet flow angle
$\dot{m}_{air}$	[kg/s]	Mass flow rate
Ω	[RPM]	Rotational speed
p_{1t}	[Pa]	Total inlet pressure
t_{1t}	[K]	Total inlet temperature
η_{tt}	[-]	Total-to-total efficiency (optional)
Geometric	**Unit**	**Description**
k	[-]	Impeller shape factor
splitter blades	[true/false]	Presence of splitter blades
splitter length ratio	[-]	Splitter to full length ratio, $L_{\text{splitter}}/L_{\text{full}}$

Table 3.1: Input parameters for the meanline design

The thermodynamic parameters determine the characteristics of the compression process the airflow goes through and the capacity of the machine. The isentropic efficiency of the stage is an optional input of the design code, as the efficiency of the stage can also be estimated through the use of meanline based loss models. If the efficiency is provided as an input, the outlet total temperatures and pressures are determined accordingly.

The duty coefficients, represented by the flow coefficient (ϕ), work coefficient (ψ), and degree of reaction (R), which are defined in equations 3.1 through 3.3 respectively, define the complete design and performance of the machine.

$$\phi = \frac{v_{1,m}}{u_2} \tag{3.1}$$

$$\psi = \frac{\Delta h_{t,ad}}{u_2^2} \tag{3.2}$$

$$R = \frac{\Delta h_{rotor}}{\Delta h_{t,ad}} \tag{3.3}$$

However, some additional geometrical parameters are needed to close the design problem. These are: the impeller shape factor, whose definition is given in equation 3.4, and the presence of splitter blades[1] with their length.

$$k = 1 - \left(\frac{D_{1,h}}{D_{1,t}}\right)^2 \tag{3.4}$$

The working fluid is modelled as a calorically-perfect gas. This simplifying assumption, which implies that working fluid properties remain independent of temperature, is made to streamline the program development and minimize computational costs.

However, it is advised to reconsider this assumption in the future and explore alternative working fluid models that account for temperature dependence of specific heat capacity (such as the thermally-perfect gas model used in GTlab [45]) and variations in composition (e.g., fuel-to-air ratio) to assess the corresponding improvements in accuracy. Table 3.2 [19, 5] presents typical values for duty coefficients and working fluid properties in radial compressor stage, assuming dry air as the working fluid.

[1] additional blades placed between the impeller full blades that occupy only partially the flow path towards the outlet

Duty Coefficient	Unit	Value
ϕ	[-]	0.2 - 0.3
ψ	[-]	0.5 - 1.0
R	[-]	0.5 - 0.85
Gas Parameter	**Unit**	**Value**
R_{gas}	[J/kg· K]	287
c_p	[J/kg· K]	1000
γ	[-]	1.4

Table 3.2: Typical ranges/values for radial compressor duty coefficients and working fluid properties [19, 5]

3.1.3. VELOCITY TRIANGLES

The first step of the meanline design is the calculation of the velocity triangles, based on the duty coefficients and the inlet absolute flow angle, following the free-vortex assumption to compute the velocity triangles at points other than the mid blade plane.

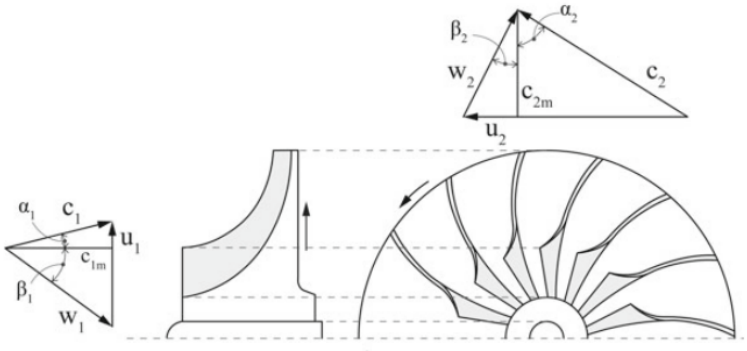

Figure 3.2: Radial impeller velocity triangles [5].

In order to calculate the velocity triangles of the radial compressor it is necessary to define three additional parameters that distinguish this procedure from its counterpart for axial machines: the rotor meridional velocity ratio $\xi = \frac{v_{2,m}}{v_{1,m}}$, the tip diameter ratio $\delta_t = D_{1,t}/D2$ and the hub diameter ratio $\delta_h = D_{1,h}/D2$. The two diameter ratios, together with the diameters of the impeller, can be easily obtained from the design inputs (the simple procedure is included in Appendix B). The rotor meridional velocity ratio is, instead, calculated as a function of the degree of reaction and the tip diameter ratio:

$$\xi = \sqrt{1 - \frac{2\psi}{\phi^2}\left(R + \frac{\psi}{2} - 1\right) + (\tan(\alpha_1))^2\left(1 - \delta_t^2\right) - \frac{2\psi\delta_t}{\phi}\tan(\alpha_1)} \tag{3.5}$$

Once the aforementioned parameters are calculated, the absolute and relative flow angles for the impeller can then be calculated as follows, noting that the angles at the inlet (1) station are calculated at the mid plane of the blade and not at the tip. At different radial position along the inlet section the tangential velocity is different, and thus also the velocity triangle will differ. It was chosen to consider the quantities at the mid plane, as these define the average velocity triangle.

The procedure can be based on the velocity triangle at the tip or at the hub of the inlet to represent the entire flow (for example in the book by M. Gambini and M. Vellini [5] the tip velocity triangle is used). All possibilities are anyway valid, and the method can be adapted to use one of these options, with minor adjustments, while mantaining the free-vortex assumption for the inlet flow, as also done for axial compressors in WEST [23]:

$$\alpha_2 = \arctan\left(\frac{1}{\phi\cdot\xi}\cdot\left(\psi + \phi\cdot\frac{\delta_t + \delta_h}{2}\cdot\tan(\alpha_1)\right)\right) \tag{3.6}$$

$$\beta_1 = \arctan\left(\frac{\delta_t + \delta_h}{2\cdot\phi} - \tan(\alpha_1)\right) \tag{3.7}$$

$$\beta_2 = \arctan\left(\frac{1}{\phi\cdot\xi} - \tan(\alpha_2)\right) \tag{3.8}$$

Once the angles are calculated, the velocities can then be determined through the following relations:

$$v_1 = u_2 \cdot \phi \cdot \sqrt{1 + \tan^2(\alpha_1)} \tag{3.9}$$

$$v_2 = u_2 \cdot \phi \cdot \xi \cdot \sqrt{1 + \tan^2(\alpha_2)} \tag{3.10}$$

$$w_1 = u_2 \cdot \phi \cdot \sqrt{1 + \tan^2(\beta_1)} \tag{3.11}$$

$$w_2 = u_2 \cdot \phi \cdot \xi \cdot \sqrt{1 + \tan^2(\beta_2)} \tag{3.12}$$

$$u_1 = u_2 \cdot \frac{\delta_t + \delta_h}{2} \tag{3.13}$$

$$v_3 = v_1 \tag{3.14}$$

$$u_{1,tip} = \frac{D_{1,t}}{60 \cdot \pi} \cdot \Omega \tag{3.15}$$

$$u_{1,hub} = \frac{D_{1,h}}{60 \cdot \pi} \cdot \Omega \tag{3.16}$$

3.1.4. THERMODYNAMIC CALCULATION

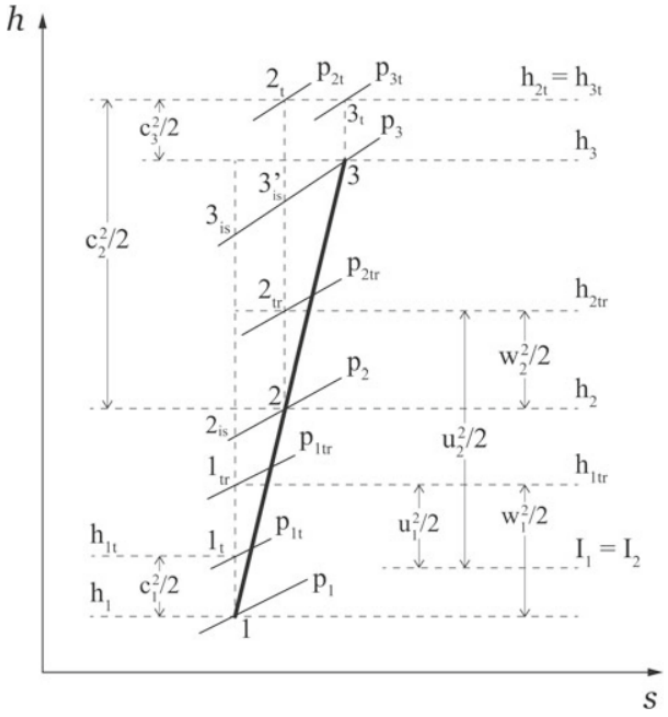

Figure 3.3: plot showing the compression process in a radial compressor stage on the h-s diagram [5].

The fluid thermodynamic states along the stage are calculated by applying the conservation equations at the three main positions of the meanline flow path, namely at the inlet (1), at the outlet of the impeller (2), and at the outlet of the vaned diffuser (3). These calculations are done based on the velocity triangles previously computed, as shown in Figure 3.3:

From the total quantities at the inlet, which are inputs of the meanline design, the static temperature (T_1), pressure (p_1), inlet mach number (m_1) and density (ρ_1) can be calculated as:

$$h_1 = h_{1t} - v_1^2/2\ ,\ T_1 = \frac{h_1}{cp}\ ,\ m_1 = \frac{v_1}{\sqrt{\gamma \cdot R \cdot T_1}}\ ,\ p_1 = \frac{p_{1t}}{\left(1 + \frac{\gamma-1}{2} \cdot m_1^2\right)^{\frac{\gamma}{\gamma-1}}}\ ,\ \rho_1 = \frac{p_1}{R \cdot T_1} \tag{3.17}$$

The entropy at the inlet can then be calculated as the entropy rise between the inlet static condition and a reference condition defined by T_{ref} and p_{ref}, being these the reference quantities of any arbitrary state:

$$s_1 = cp \cdot \ln\left(\frac{T_1}{T_{ref}}\right) - R \cdot \ln\left(\frac{p_1}{p_{ref}}\right) \tag{3.18}$$

The relative total quantities ($h_{1tr}, T_{1tr}, p_{1tr}$) at the inlet can then be computed as:

$$h_{1tr} = h_1 + \frac{w_1^2}{2}\ ,\ T_{1tr} = \frac{h_{1tr}}{cp}\ ,\ p_{1tr} = p_1 \cdot exp\left(\frac{cp}{R} \cdot \ln\left(\frac{T_{1tr}}{T_1}\right)\right) \tag{3.19}$$

Based on the definition of the degree of reaction (R_{stage}), the enthalpy rise across the impeller can be calculated based on the specific work of the stage (w), namely:

$$\Delta h_R = w \cdot R_{stage} \tag{3.20}$$

$$h_{2\text{is}} = h_1 + \eta_R \cdot \Delta h_R \tag{3.21}$$

Considering the conservation of rothalpy across the impeller, the outlet enthalpy can then be calculated as:

$$I_2 = I_1 = h_{1tr} - \frac{u_1^2}{2}\ ,\ h_2 = I_2 - \frac{w_2^2}{2} + \frac{u_2^2}{2} \tag{3.22}$$

The static quantities at the impeller outlet can then be computed along with the entropy at the outlet of the impeller and the outlet absolute mach number (m_2), which read:

$$T_{2\text{is}} = \frac{h_{2\text{is}}}{cp}\ ,\ T_2 = \frac{h_2}{cp}\ ,\ p_2 = p_1 \cdot \left(\frac{T_{2\text{is}}}{T_1}\right)^{\frac{\gamma}{\gamma-1}}\ ,\ \rho_2 = \frac{p_2}{R \cdot T_2} \tag{3.23}$$

$$s_2 = cp \cdot \ln\left(\frac{T_2}{T_{ref}}\right) - R \cdot \ln\left(\frac{p_2}{p_{ref}}\right) \tag{3.24}$$

$$m_2 = \frac{v_2}{\sqrt{\gamma \cdot R \cdot T_2}} \tag{3.25}$$

The total quantities and total relative quantities at the outlet are then computed as:

$$h_{2t} = h_2 + \frac{v_2^2}{2}\ ,\ T_{2t} = \frac{h_{2t}}{cp}\ ,\ p_{2t} = p_2 \cdot \left(1 + \frac{\gamma-1}{2} \cdot m_2^2\right)^{\frac{\gamma}{\gamma-1}} \tag{3.26}$$

$$h_{2tr} = h_2 + \frac{w_2^2}{2}\ ,\ T_{2tr} = \frac{h_{2tr}}{cp}\ ,\ p_{2tr} = p_2 \cdot exp\left(\frac{cp}{R} \cdot \ln\left(\frac{T_{2tr}}{T_2}\right)\right) \tag{3.27}$$

The total enthalpy is conserved through the stator/diffuser; the total, static and static-isentropic enthalpy at station 3 can be then calculated as:

$$h_{3t} = h_{2t}\ ,\ h_3 = h_{3t} - \frac{v_3^2}{2}\ ,\ h_{3\text{is}} = h_1 + \eta_{\text{is}} \cdot (h_3 - h_1) \tag{3.28}$$

The remaining static and total quantities at the outlet of the stage are determined as:

$$T_{3\text{is}} = \frac{h_{3\text{is}}}{cp}\ ,\ T_3 = \frac{h_3}{cp}\ ,\ p_3 = p_1 \cdot \left(\frac{T_{3\text{is}}}{T_1}\right)^{\frac{\gamma}{\gamma-1}}\ ,\ \rho_3 = \frac{p_3}{R \cdot T_3} \tag{3.29}$$

$$s_3 = cp \cdot \ln\left(\frac{T_3}{T_{ref}}\right) - R \cdot \ln\left(\frac{p_3}{p_{ref}}\right) \tag{3.30}$$

$$T_{3t} = \frac{h_{3t}}{cp}\ ,\ m_3 = \frac{v_3}{\sqrt{\gamma \cdot R \cdot T_3}}\ ,\ p_{3t} = p_3 \cdot \left(1 + \frac{\gamma-1}{2} \cdot m_3^2\right)^{\frac{\gamma}{\gamma-1}} \tag{3.31}$$

3.1.5. BLADE ANGLES AND BLADE COUNT

After the thermodynamic quantities and velocity triangles are calculated, the blade main geometric parameters can then be defined and the outlet velocity slip can be estimated.

First the mean inlet relative velocity (w_{1M}) is calculated based on the average inlet relative flow angle (β_{1M}), which is considered equal to the relative flow angle at the blade inlet at mid-span (β_1):

$$w_{1M} = \frac{v_{1_m}}{\cos(\beta_{1M})} \tag{3.32}$$

Where v_{1_m} is the inlet meridional velocity.

The number of blades of the impeller (N_{BR})is then estimated by using the relation proposed Eckert et al. [46] and reported in this formulation by Osnaghi [47]:

$$N_{BR} = \left\lceil \frac{2\pi \cdot \cos(\beta_M)}{\xi \cdot ln\left(\frac{1}{\delta_t}\right)} \right\rceil \tag{3.33}$$

where $\beta_M = \frac{\beta_{1M}+\beta_{2B}}{2}$ and β_{2B} are, respectively, the mean relative flow angle and the impeller outlet metal blade angle; δ_t is the tip diameter ratio defined in Section 3.1.3 and ξ is a constant which value can be chosen from a range between 0.35 to 0.45 according to Eckert et al. [46]. In this case $\xi = 0.45$ is assumed, as it was found to provide the best results during the validation of the meanline code.

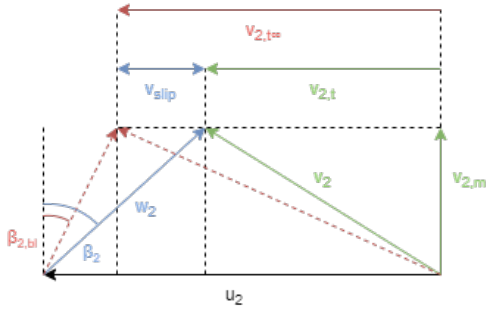

Figure 3.4: Illustration of the effect of slip on the impeller outlet velocity triangle

Once the number of rotor blades is estimated, the slip factor ($SF = \frac{v_{2,t}}{v_{2,t,\infty}}$) is computed using the method by Weisner [48]:

$$SF = 1 - \frac{\sqrt{\cos(\beta_{2,bl})}}{N_{BR}^{0.7}} \tag{3.34}$$

In the book by Aungier [43] it is suggested that in case the mean diameter ratio ($\delta_M = \frac{D_{1,M}}{D_2}$) exceeds its limit value ($\delta_{M_{lim}}$), a correction should be applied to the slip factor:

$$SF = SF\left(1 - \left(\frac{\delta_M - \delta_{M_{lim}}}{1 - \delta_{M_{lim}}}\right)^{\sqrt{\frac{90-\beta_2}{10}}}\right) \tag{3.35}$$

Where SF_{lim} and $\delta_{M_{lim}}$ are defined as follows:

$$SF_{lim} = \sin\left(19\,\text{deg} + 0.2 \cdot (90\,\text{deg} - \beta_2)\right) \tag{3.36}$$

$$\delta_{M_{lim}} = \frac{SF - SF_{lim}}{1 - SF_{lim}} \tag{3.37}$$

Based on the computed value for the slip factor, a new value of the impeller outlet metal blade angle is computed based on the geometric relation shown in Figure 3.4, namely:

$$\tan(\beta_{2,bl}) = \frac{u_2}{v_{2,m}} - \frac{v_{2,t}}{SF \cdot v_{2,m}} \tag{3.38}$$

The solution of the set of equations 3.33 - 3.38 is then repeated until convergence is achieved.

3.1.6. IMPELLER GEOMETRY

The hydraulic diameters at the inlet and outlet (D_{hyd1} and D_{hyd2}) are defined as:

$$D_{hyd} = 4 \cdot \frac{Cross\ sectional\ area}{Wetted\ perimeter} \tag{3.39}$$

The average hydraulic diameter (D_{hydR}) is calculated as the average of D_{hyd1} and D_{hyd2}:

$$D_{hyd,R} = \frac{D_{hyd1} + D_{hyd2}}{2} \tag{3.40}$$

The axial length (L_a), if not provided by the user through the axial-length-to-tip-diameter ratio is calculated according to the semi-empirical correlation provided by Aungier [43]:

$$L_a = D_2 \cdot \left(0.014 + \frac{0.023}{\delta_h} + 1.58(\delta_t^2 - \delta_h^2)\phi\right) \tag{3.41}$$

The meridional length ($L_{m,R}$) of the impeller flowpath is then determined (in a first approximation) as the lenght of a semi-circular arc of equivalent radius r_{eq}:

$$r_{eq} = \frac{(2 \cdot L_a - b_2 + D_2 - D_{1,t} + b_1)}{4} \tag{3.42}$$

$$L_{m,R} = \frac{\pi}{2} r_{eq} \tag{3.43}$$

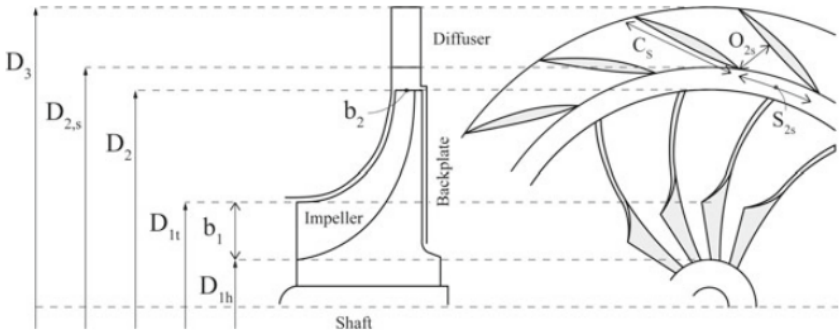

Figure 3.5: Schematic of the compressor stage geometry with the relevant diameters [5]

Figure 3.5 shows a simplified schematic of a radial compressor stage. It can be seen how the diffuser is divided into two sections: the vaneless diffuser between D_2 and $D_{2,s}$, and the vaned diffuser between D_2, s and D_3.

3.1.7. VANELESS DIFFUSER GEOMETRY

The vaneless diffuser length is determined using the relation obtained by interpolating the data provided by Grieb [6](Fig. 3.6):

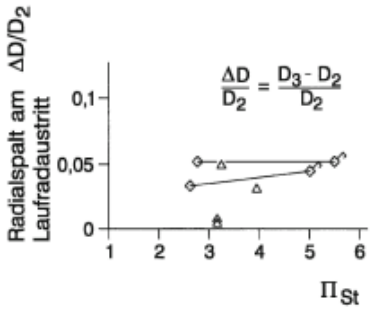

Figure 3.6: Vaneless diffuser lenght against stage pressure ratio, in the plot what is referred to as D_3 corresponds to the vaneless diffuser outlet diameter $D_{2,s}$ [6]

$$D_{2s} = 1.05 \cdot D_2 \tag{3.44}$$

Given its relatively short length, the flow angle through the vaneless portion of the diffuser is assumed to be constant:

$$\alpha_{2s} = \alpha_2 \tag{3.45}$$

3.1.8. VANED DIFFUSER GEOMETRY

The vaned diffuser blade height can be calculated by equating the flow area at the outlet of the vaneless diffuser with the flow area at the inlet of the vaned diffuser.

The vaned diffuser length is also determined using a relation obtained by interpolating the data provided by Grieb [6] (Fig. 3.7) which reads:

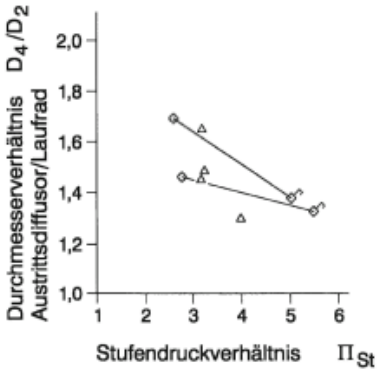

Figure 3.7: Vaned diffuser lenght against stage pressure ratio, in the plot what is referred to as D_4 corresponds to the vaned diffuser outlet diameter D_3 [6]

$$D_3 = (-0.05 \cdot \beta_{tt} + 1.575) \cdot D_2 \tag{3.46}$$

The number of vanes in the diffuser (N_{BS}) is determined based on the number of blades of the impeller in order to avoid resonance phenomena as suggested by Aungier [14]:

$$N_{BS} = N_{BR} + 8 \tag{3.47}$$

The choice of the number of vanes for the diffuser is a quite complex design problem. The relation provided by Aungier[14] reprsents a good first guess, but a more detailed design might yield a different optimal number of blades.

The meridional length ($L_{m,s}$) and hydraulic length ($L_{hyd,s}$) of the vaned diffuser can be then computed as:

$$L_{m,s} = \frac{D_3 - D_{2,s}}{2} \tag{3.48}$$

$$L_{hyd,s} = \frac{L_{m,s}}{2cos((\alpha_{2s} + \alpha_3)/2)} \tag{3.49}$$

If not provided as an input of the meanline design, the vaned diffuser outlet absolute flow angle (α_3) is determined by enforcing that the value of the divergence angle (θ_c) as defined by Aungier [43] falls within its optimal range.

$$tan(\theta_c) = \frac{\pi \cdot (D3 \cdot cos(\alpha_3) - D2s \cdot cos(\alpha_{2s}))}{2 \cdot N_{BS} \cdot L_{hyd,s}} \tag{3.50}$$

$$10^o < 2 \cdot \theta_{c,opt} < 11^o \tag{3.51}$$

Once the vaned diffuser outlet absolute flow angle (α_3) is defined, the static thermodynamic quantities have to be calculated again based on the new velocity triangle.

3.1.9. DIFFUSER VANE GEOMETRY

The diffuser vanes are designed adopting the thickness distribution suggested by Aungier [13]. In this case, the maximum thickness is the same as the outlet blade thickness of the impeller while the inlet and outlet thicknesses are assumed to be 0.

The thickness distribution is defined as follows:

$$t = t_0 + (t_m - t_0) \cdot y^e \tag{3.52}$$

$$t_0 = t_{in} + (t_{out} - t_{in}) \cdot x/c \tag{3.53}$$

$$y = x/x_m \; for \; x < x_m \; and \; y = (1-x)/(1-x_m) \; for \; x > x_m \tag{3.54}$$

$$e = \sqrt{\frac{0.4 x_m}{c}} \cdot (0.95 \cdot (1 + x/c) \cdot (1 - y) + 0.05) \tag{3.55}$$

Where t_{in} is the inlet thickness, t_{out} is the outlet thickness, t_m is the maximum thickness of the profile and x_m is its position along the chord, in this case set to a default value of 0.3; Figures 3.8 and 3.9 display examples of diffuser vanes for two radial compressors, featuring different inlet and outlet angles and diameters.

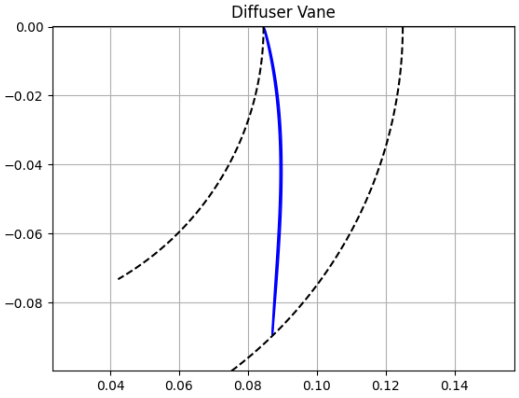

Figure 3.8: Example of a generated diffuser vane with $\alpha_{2s} = 74.4^o$ and $\alpha_{2s} = 46.8^o$

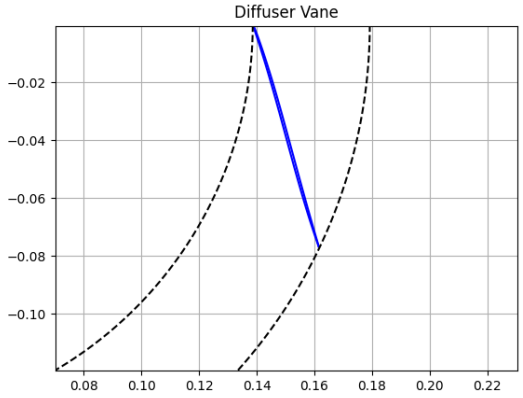

Figure 3.9: Example of a generated diffuser vane with $\alpha_{2s} = 70^o$ and $\alpha_{2s} = 44^o$

These plots show a front view of the diffuser, analogous to Figure 3.18, where the x and y axis display the actual dimensions in meters.

3.1.10. FLOWPATH SHAPE

The meridional flowpath shape is generated using a set of Bezier curves, with a method similar to that described by Smith et.al. [49]. The tip and hub profiles of the meridional flowpath of the impeller are drawn using 4 control points each, as shown in Figure 3.10. The first three control points are equally spaced along a line, which is horizontal for the tip profile, and diagonal for the hub profile, in order to make sure that the inlet hub meridional profile is not horizontal.

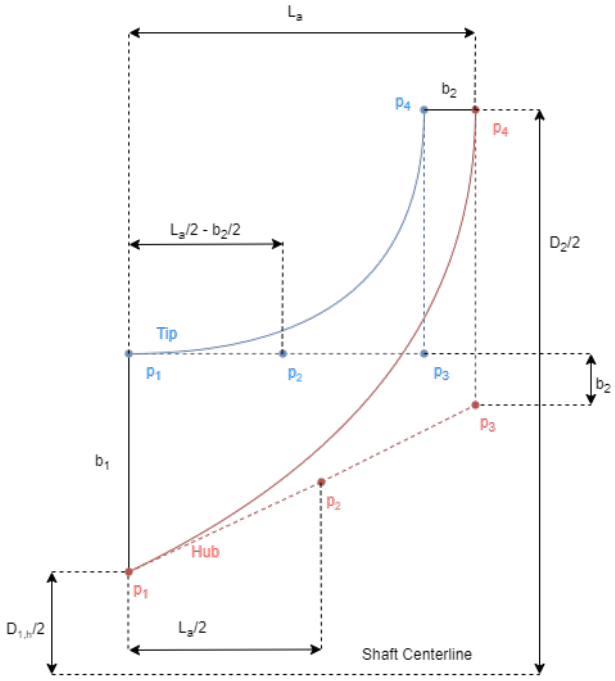

Figure 3.10: Control points of the Bezier curves used to generate the tip (blue) and hub (red) geometry of the impeller meridional flow path

3.1.11. BLADE ANGLE DISTRIBUTION

Given the shape of the hub and tip profiles of the meridional channel, the blade shape can be designed using a blade angle distribution defined by another series of Bezier curves, similarly to what is done by Smith et.al. [49]. These curves are still based upon 4 control points: the inlet and outlet points are fixed by the meanline design, and they correspond to the inlet and outlet blade angles,while the other two points, which are equally spaced along the meridional channel length, are tuned in order to achieve an axial backsweep angle of less than 30 degrees at the outlet.

An example of a meridional channel and blade angle disribution obtained using these methodologies is reported in figures 3.41 and 3.12.

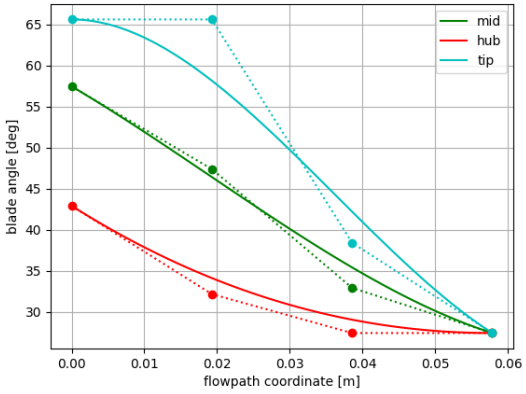

Figure 3.11: Example of a blade angle distribution along the impeller flow path generated using Bezier curves

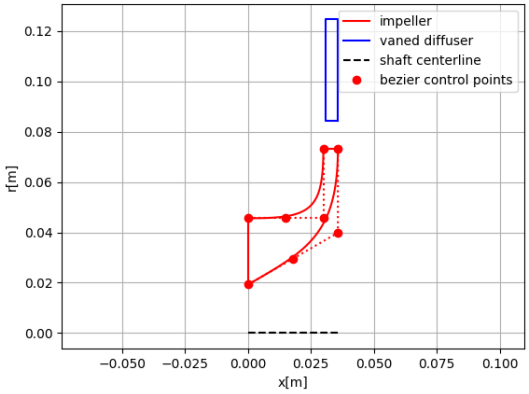

Figure 3.12: Example of the meridional flow path shape generated using Bezier curves

3.1.12. IMPELLER BLADE SHAPE GENERATION

The blade shape is generated according to the previously calculated blade angles following an iterative method mapping the 2D coordinates of the meridional flow path to the 3D coordinates of the tip and hub of the blade,

namely:

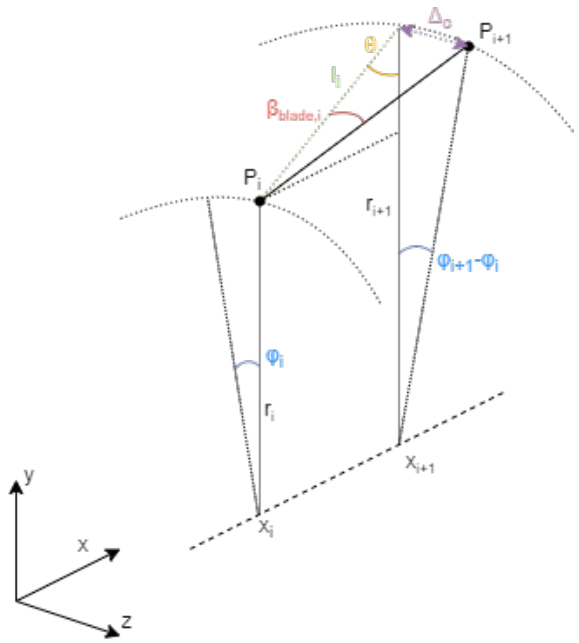

Figure 3.13: Illustration of the coordinate conversion for the hub or tip 3D blade profiles

$$P_{2D} = (x, r) \Rightarrow P_{3D,polar} = (x, r, \phi) \Rightarrow P_{3D} = (x, y, z)$$

The following equations show how the coordinates of the 3D profile are calculated based on the meridional channel shape and blade angle distribution, with $\beta_{blade,i}$ being the blade angle calculated at the position along the meridional channel corresponding to (x_i, r_i):

First, the meridional channel is discretized into segments and the angle between the radial direction and each segment (θ) is calculated, along with the resulting length of the segment (l_i):

$$\theta = \arctan\left(\frac{x_{i+1} - x_i}{r_{i+1} - r_i}\right) \tag{3.56}$$

$$l_i = \frac{r_{i+1} - r_i}{\cos(\theta)} \tag{3.57}$$

Then the local tangential component of the blade segment (Δ_c) and the corresponding cylindrical coordinate angle (ϕ) are calculated:

$$\Delta_c = l_i \cdot \tan(\beta_{blade,i}) \tag{3.58}$$

$$\phi_{i+1} = \phi_i + 2\arcsin\left(\frac{\Delta_c}{2 \cdot t_{i+1}}\right) \tag{3.59}$$

The cylindrical coordinates can then be easily converted into 3D coordinates:

$$y_{i+1} = r_{i+1} \cdot \cos(\phi_{i+1}) \tag{3.60}$$

$$z_{i+1} = r_{i+1} \cdot \sin(\phi_{i+1}) \tag{3.61}$$

3.1.13. BLADE THICKNESS

Differently to axial compressors, radial compressor blades are much longer compared to the blade height, and thus the impeller blades can be modelled as thin panels whose thickness increases linearly from the inlet to the outlet of the impeller.

The blade thickness at the inlet and outlet can be then estimated by using the data provided by Xu and Amano [7, 8] correlating the blade thickness with blade height for a set of radial compressors.

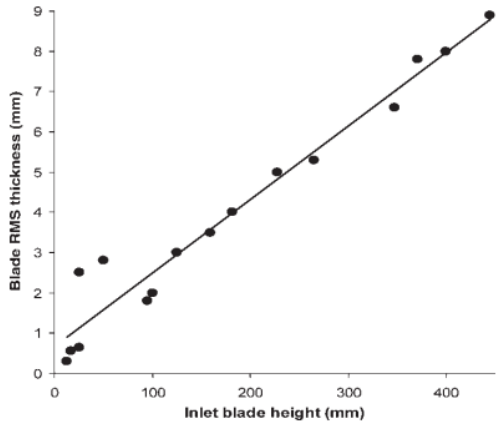

Figure 3.14: Blade thickness vs. height at station 1 [7, 8]

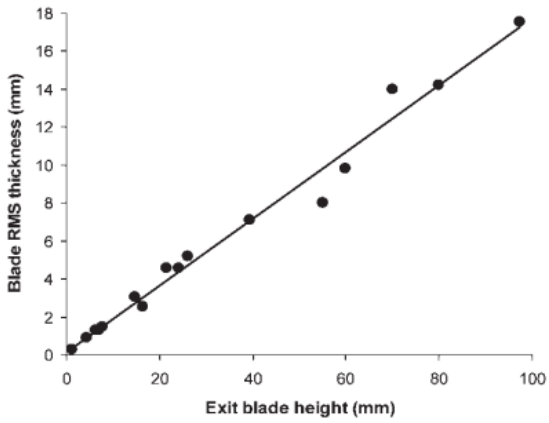

Figure 3.15: Blade thickness vs. height at station 2 [7, 8]

3.1.14. VALIDATION

The meridional channel shape generation was validated by comparing the design obtained with the proposed procedure to the preliminary design shown by Bryce et.al. [50]. The specifications of this test case are reported in Table 3.3:

Duty Coefficient	**Unit**	**Value**
ϕ	[-]	0.2826
ψ	[-]	0.79
R	[-]	0.625
Thermodynamic	**Unit**	**Value**
β_{tt}	[-]	6.807
α_1	[rad]	0
$\dot{m}_{air}$	[kg/s]	0.907
Ω	[RPM]	75000
p_{1t}	[Pa]	100000
t_{1t}	[K]	300
Geometric	**Unit**	**Value**
k	[-]	0.8219 [a]
splitter blades	[true/false]	False
L_a/D_2	[-]	0.3

[a] Value not provided, was calculated based on the geometry presented in the paper

Table 3.3: Input parameters for the validation case

One additional input was necessary to replicate this validation case, namely the axial-length-to-tip-diameter ratio (L_a/D_2). Such a quantity was determined based on the axial length of the impeller presented in the paper. Otherwise, the the design procedure would lead to an axial length about 20% lower than that reported in the reference.

The axial impeller length only influences the efficiency of the rotor resulting from the implemented loss models. All other parameters, such as the velocity triangles and blade count, are independent from this quantity.

Parameter	Unit	Bryce et al. [50]	Calculated
$\beta_{1,hub}$	[deg]	45.6	42.8
$\beta_{1,tip}$	[deg]	63.4	65.5
β_2	[deg]	41.9	43.7
$\beta_{2,blade}$	[deg]	33	27.4
N_{blades}	[-]	19	22
β_{tt}	[-]	6.807	6.8
η_{is}	[-]	0.81	0.83
$m_{1,tip}$	[-]	1.195	1.158

Table 3.4: Design comparison

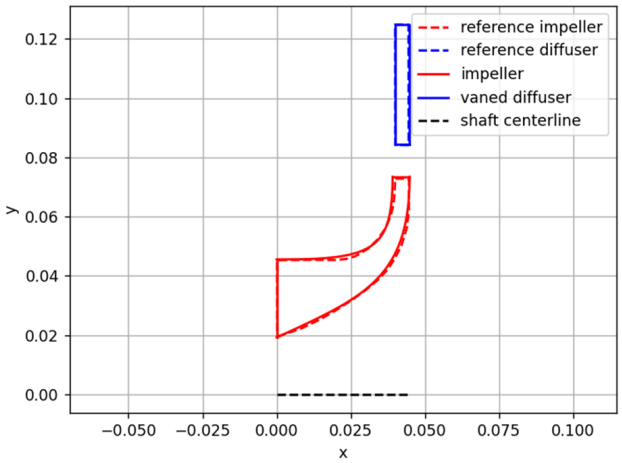

Figure 3.16: Meridional flow path plot

Overall, a good match is found between the reference data and the designed impeller (shown in more detail in Figures 3.17 and 3.18). The highest mismatch is found in the impeller outlet blade angle ($\beta_{2,blade}$), probably due to the approximations made in the calculation of the outlet slip factor. The impeller outlet relative flow angle (β_2) is very closely replicated by the design method, with a mismatch of less than 2^o; however the difference between the blade and flow angle is much higher for the calculated values than for the reference, meaning that the slip is overestimated by the meanline design.

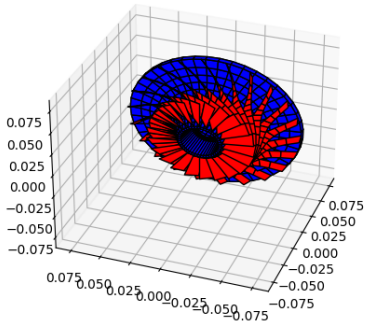

Figure 3.17: Example of the 3D shape of the impeller with blades

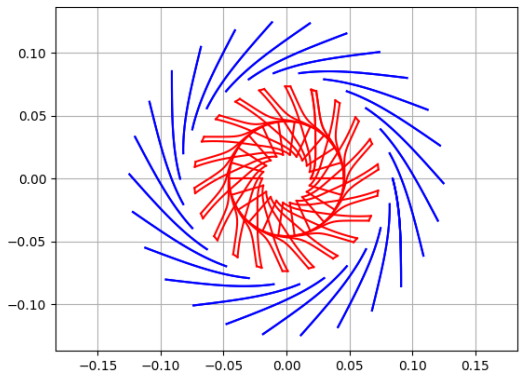

Figure 3.18: Front view of the 3D blades (vaned diffuser blades are plotted in blue)

3.2. DISK DESIGN

The compressor disk alone constitutes a major proportion of the total weight of the stage. Therefore, significant emphasis has been placed on exploring approaches that can precisely and effectively simulate the stresses in the compressor disk and blades to enable the design of these components within WEST.

3.2.1. DESIGN PROCEDURE

The design procedure for the radial compressor disk, illustrated by the flow chart in Figure 3.19, is similar to its analogous for axial turbomachinery. After the meanline design is completed and the shape of the meridional channel and the blades are determined based on that, a first guess for the disk geometry is made. This geometry is then optimized to minimize its weight while mantaining the stress values within the limits defined by the mechanical strength of the material.

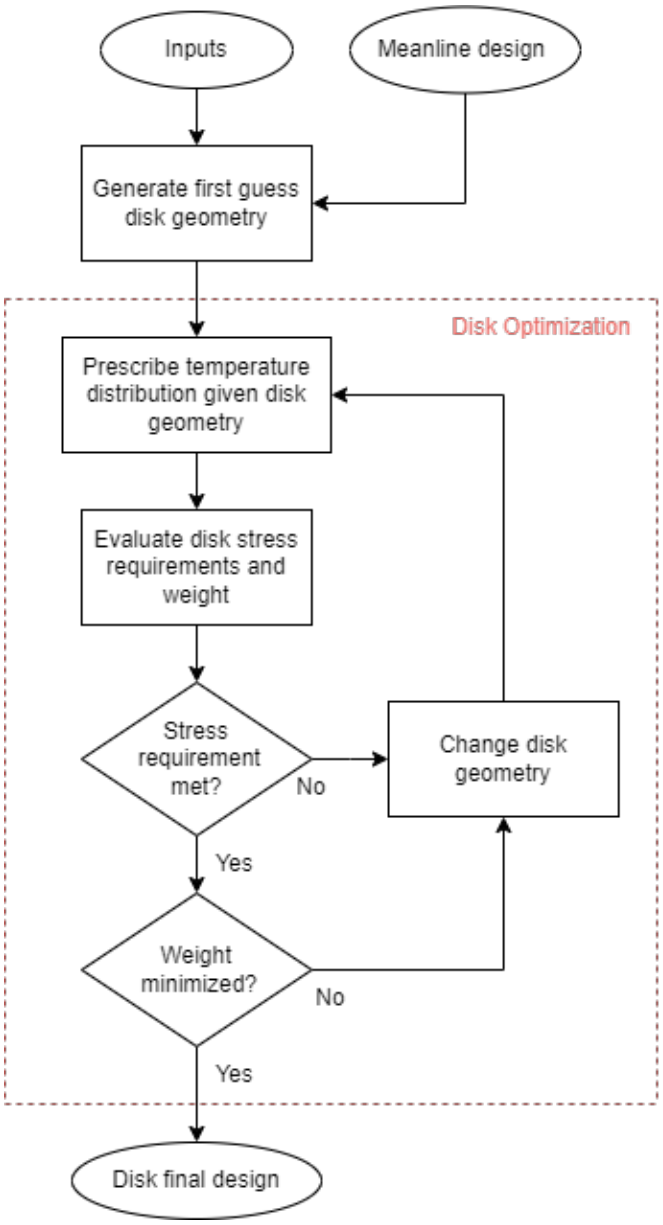

Figure 3.19: Disk design flowchart

3.2.2. STRESS CRITERIA

The stress criteria for the radial compressor disks is analogous to those considered for axial compressors at this stage of the preliminary design. They are two and can be assessed once the stress distribution within the disk

is determined: the yield criterion and the burst criterion as discussed by Tong et al. [51]. Their mathematic definition is here reported, using the same formulation proposed by I.Boersma [23] so that only non-zero parameters are present in the denominator.

$$1 - \frac{SF \cdot \sigma_{vm}}{\sigma_y} > 0 \tag{3.62}$$

The von Mises stress (σ_{vm}) can be compared to the yield stress of the material at each local section (accounting for the variation in yield stress given by the local operating temperature) to determine the safety factor with respect to material yield, as is shown in equation 3.62. Tong et al. [51] recommends a factor of safety, SF, equal to 1.1.

The burst criterion, reported in equation 3.63, is used to compare the ultimate tensile strength of the material (σ_{UTS}) to the average tangential (or hoop) stress ($\sigma_{t,ave}$) that it has to withstand; in this way the plastic behaviour of the material, which is of particular relevance at overspeeds, can be captured as well [26].

$$1 - \frac{\sigma_{t,ave}}{0.47 \cdot \sigma_{UTS}} > 0 \tag{3.63}$$

3.2.3. DISK GEOMETRY

Based on the available data for existing engine designs, two main types of geometries have been identified for radial compressor impeller disks and both can be analyzed by the code.

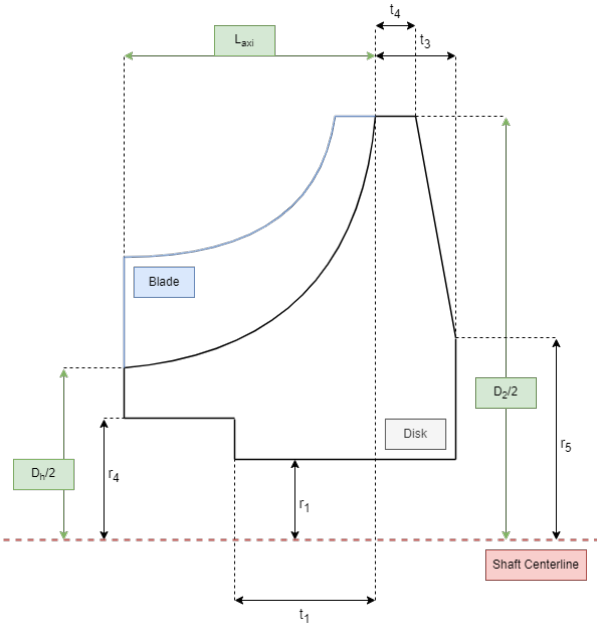

Figure 3.20: "A" type disk

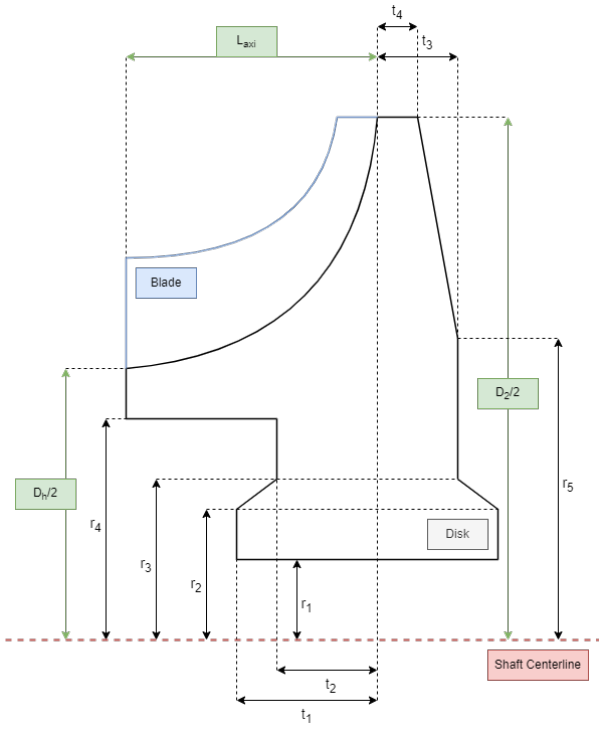

Figure 3.21: "B" type disk

The 'A' type disk (shown in figure 3.20) is usually found in low hub diameter ratio / high shape factor impellers, where the space between the shaft outside radius and the hub radius of the impeller is low, such as in both radial compressor stages of the MTR390 turboshaft engine [52]. The 'B' type disk (shown in figure 3.21) is instead for high hub diameter ratio / low shape factor impellers, and is mainly adopted in mixed axial-radial flow compressors, such as in the GE T700 engine [53].

The stress requirement for both disk types is the same, and the optimization is conducted in a very similar manner; the parameters outlined in green are fixed during the meanline design, together with the meridional shape and the shape of the blades. All other dimensions have to be determined by the optimization algorithm.

3.2.4. INPUTS

The disk design procedure only requires three additional inputs from the user after the meanline flow path has been determined. These are reported in Table 3.5.

Geometric	Unit	Description
$r_{sh,max}$	[m]	Maximum shaft radius
Disk type	[-]	–
Disk material	[-]	–

Table 3.5: Input parameters for disk design

The maximum shaft radius determines the minimum radius that the impeller disk hub can have, otherwise there would be an interference between the two elements.

3.2.5. BOUNDS AND CONSTRAINTS

The optimization of the disk focuses on minimizing the overall mass of the component while not violating the stress criteria described in section 3.2.2.To ensure the feasibility of the geometry for the impeller, a set of constraints has been defined for the variables manipulated by the optimizer. These limitations are set as follows:

$$D_h/2 - (D_2/2 - D_h/2)/20 > r_1, r_2, r_3, r_4 > r_{sh,max} \tag{3.64}$$

$$D_h/1.5 > 5 > r_{sh,max} \tag{3.65}$$

$$L_a > t_1, t_2 > 0.1 \cdot L_a \tag{3.66}$$

$$0.2 \cdot L_a > t_3, t_4 > 0.013 \cdot D_2/2 \tag{3.67}$$

Some additional inequality constraints are also enforced in order to avoid unfeasible geometries.

$$\frac{r_3 - r_2}{t_1 - t_2} \geq tan\left(\frac{\pi}{4}\right) \tag{3.68}$$

$$t_1 \geq t_2 \geq \frac{t_1}{2} \tag{3.69}$$

$$r_5 \geq r_3 \tag{3.70}$$

$$r_4 \geq r_3 \tag{3.71}$$

$$r_3 \geq r_2 \tag{3.72}$$

$$\begin{cases} r_2 \geq r_1 \cdot 1.1 & \text{if disk type 'B'} \\ r_2 \geq r_1 & \text{if disk type 'A'} \end{cases} \tag{3.73}$$

3.2.6. OBJECTIVE FUNCTION

The objective of the design procedure is to minimize the weight of the disk while maintaining the maximum stress below the limits set by the material. More in detail, the objective function of the optimization reads:

$$f_{obj} = k \cdot \frac{\text{weight}}{\text{weight}_0} + (1-k) \cdot \frac{\sigma_{max}}{\sigma_{max,0}} - A \tag{3.74}$$

$$A = \begin{cases} lim_Y & \text{if } lim_Y \leq 0 \\ 0 & \text{otherwise} \end{cases} \tag{3.75}$$

Where weight_0 is the weight of the first guess design, and lim_Y is the yield stress criterion term, expressed in equation 3.62.

The first guess design provided to the optimizer at the beginning of the design procedure may not be feasible. This may give some problems to the optimizer, which can have difficulties in finding a feasible geometry if it starts outside the correct design space.

For this reason in case the stress in the disk is above the yield criterion, a term proportional to the severity of the violation of the criterion (A) is added to the objective function so that the design is penalized by the optimizer and so that the gradient may lead more easily to feasible solutions as well.

The k parameter is set to 1 by default. This means that the second term in the objective function is normally ignored. In case the optimizer cannot find a feasible solution, the parameter k is changed to a value between 0 and 1 in order to let the optimizer minimize the maximum stress as well as the weight; if k is set to 0, only the maximum stress will be minimized.

3.3. DISK STRESS ANALYSIS

The stress analysis methodology described by Lolis [26] can be effectively used only for axial turbomachinery disk design, as it assumes that the rotating disk cross-section is symmetric in the axial direction. An alternative method to evaluate the stress distribution inside an impeller disk was then required.

3.3.1. BACKGROUND

The paper by M.J. Schilhansl [11] assesses the impact of centrifugal forces in radial compressors. Other stress are neglected, as the centrifugal ones are usually predominant at high speeds. The paper introduces a relatively straightforward approach based on a stress-strain correlation for determining the stresses in the disk of radial compressors adopting purely radial blades. The compressor is discretized into radial slices that correspond to the blades, and integrates the forces acting along the length of each slice (in the radial and tangential directions) to compute the resultant stresses.

G.S.Ray and B.K.Sinha [9] developed a procedure based on the method by Schilhansl [11] for computing centrifugal stresses in axisymmetric impellers having disks of variable thickness and blades laterally attached.

This procedure, also theoretically illustrated in the book by J.W. Sawyer [54], consists in discretizing both the disks and the blades and replacing them with a set of concentric stepped rings of different axial length according to the impeller geometry, see Figure 3.22.

The mechanical equilibrium is then solved for each ring using the recurring relation for the force, moment, linear displacement and angular displacement used by Schilhansl [11].

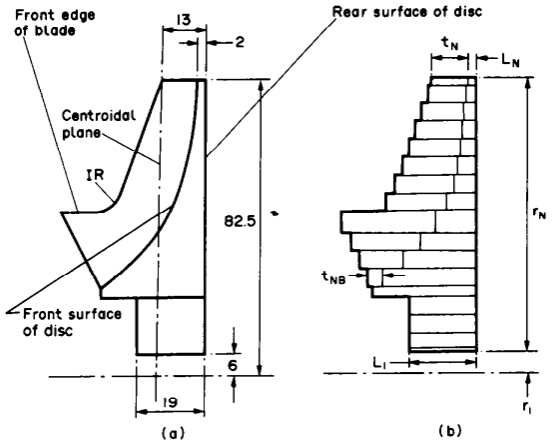

Figure 3.22: Representation of the bladed impeller: (a) sectional view, (b) replacement by a system of concentric stepped rings. [9]

Zheng et al. [10] conducted a study on the effect of temperature and pressure on the stress of a radial compressor using finite element analysis, and found that the stress caused by the temperature gradient can reach up to 57% of the total equivalent stress and is proportional to the difference between the flow temperature at the inlet and the temperature assumed for the disk hub surface (Figure 3.23). The authors suggest that the temperature effect should not be neglected in the stress analysis of the impeller.

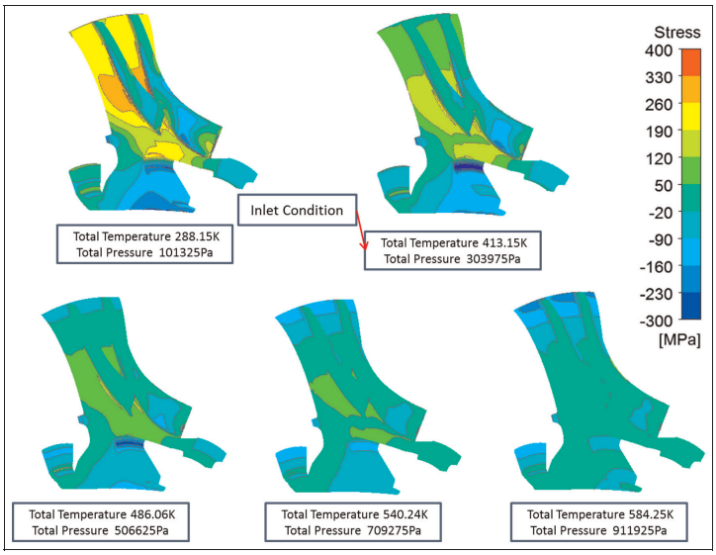

Figure 3.23: Thermal stress distribution of the impeller for different inlet conditions [10]

No method was found in literature to model the effect of temperature without recurring to more sophisticated procedures such as finite elements analyses. Thus a new simplified method was devised to evaluate thermal stresses together with centrifugal loads.

3.3.2. STRESS ANALYSIS METHOD

The methodology that is used to calculate the stress distribution in the impeller disk is based on that developed by Schilhansl [11]. Adaptations were made to take the thermal stresses in the disk into account. To this purpose, the stress-strain relation was modified according to Tong et al.[51]. The stress-strain relation in [51] is also at the basis of stress calculation in axial turbomachinery disks.

The original expression for the radial (σ_r) and tangential (σ_t) stresses are then changed as follows for the disk:

$$\sigma_{r,D} = \frac{E}{1-\nu^2} \cdot (\epsilon_r + \nu\epsilon_t) \rightarrow \sigma_{r,D} = \frac{E}{1-\nu^2} \cdot \left(\epsilon_r + \nu\epsilon_t - (1+\nu)\alpha_{exp}\Delta T\right) \tag{3.76}$$

$$\sigma_{t,D} = \frac{E}{1-\nu^2} \cdot (\epsilon_t + \nu\epsilon_r) \rightarrow \sigma_{t,D} = \frac{E}{1-\nu^2} \cdot \left(\epsilon_t + \nu\epsilon_r - (1+\nu)\alpha_{exp}\Delta T\right) \tag{3.77}$$

And for the blade:

$$\sigma_{r,B} = E \cdot (\epsilon_r) \rightarrow \sigma_{r,B} = E \cdot \left(\epsilon_r - \alpha_{exp}\Delta T\right) \tag{3.78}$$

Where ΔT is the difference between the local temperature and the reference temperature at which the thermal expansion coefficient is defined.

In order to proceed with the stress analysis methodology, the disk has to be subdivided in radial "slices" such that each slice corresponds to a blade. Then the slices are discretized radially into elements forming concentric stepped rings (see Figure 3.24).

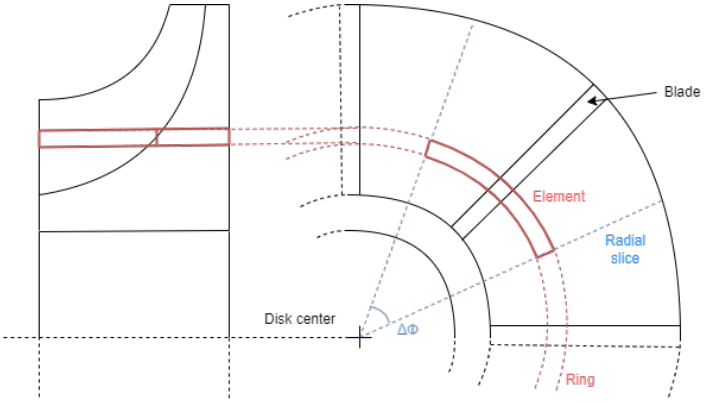

Figure 3.24: Sketch of an element of the discretized disk

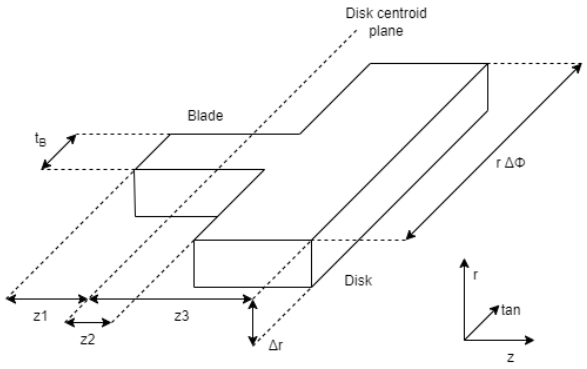

Figure 3.25: Coordinate system and geometry of an element discretizing the impeller.

The radial and tangential unit elongations (ϵ_r and ϵ_t) can be expressed in terms of the displacement of each volume element in the radial and axial directions such that:

$$\epsilon_r = \frac{\Delta u}{\Delta r} - z\frac{\Delta \alpha}{\Delta r} = \epsilon_{r0} - z\alpha' \tag{3.79}$$

$$\epsilon_t = \frac{u_0}{r} - z\frac{\alpha}{r} \tag{3.80}$$

$$\sigma_{r,D} = \frac{E}{1-\nu^2} \cdot \left(\epsilon_{r0} + \nu\frac{u_0}{r} - z\alpha' - \nu\frac{z}{r}\alpha - (1+\nu)\alpha_{exp}\Delta T\right) \tag{3.81}$$

$$\sigma_{t,D} = \frac{E}{1-\nu^2} \cdot \left(\nu\epsilon_{r0} + \frac{u_0}{r} - \nu z\alpha' - \frac{z}{r}\alpha - (1+\nu)\alpha_{exp}\Delta T\right) \tag{3.82}$$

And for the blade:

$$\sigma_{r,B} = E \cdot \left(\epsilon_{r0} - z\alpha' - \alpha_{exp}\Delta T\right) \tag{3.83}$$

Where u_0 and α are the radial and rotational terms of the displacement of each element (shown in Figure 3.26) and z is the axial coordinate in each element (see Figure 3.25), and ϵ_{r0} and α' are the components of the unit elongation in the radial direction (ϵ_r).

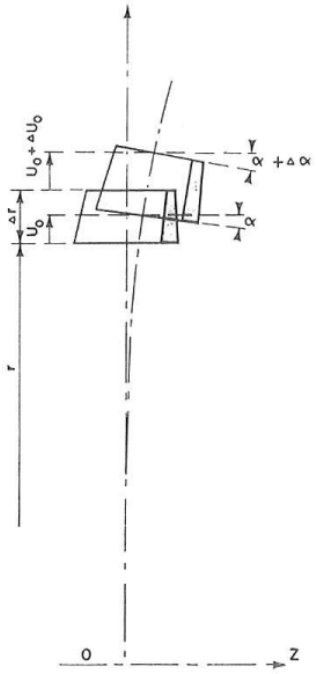

Figure 3.26: displacement and strain of a volume element [11]

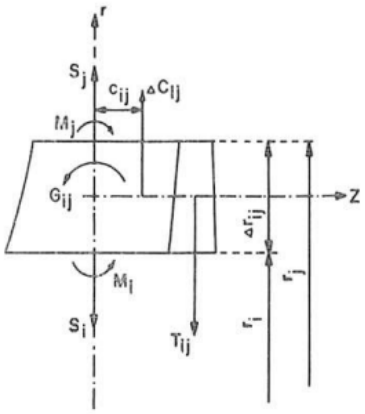

Figure 3.27: Equilibrium of a volume element of the compressor (blade and disk) [11]

For each of these volume elements the equilibrium equation in the radial direction is then evaluated as described in the paper by Ray et.al. [9], and the forces, moments and displacements at the interface between the elements are calculated:

$$S_{i+1} + \Delta C_{i,i+1} - T_{i,i+1} - S_i = 0 \tag{3.84}$$

$$M_{i+1} - c_{i,i+1} \cdot \Delta C_{i,i+1} - G_{i,i+1} - M_i = 0 \tag{3.85}$$

$$u_{0,i+1} = u_{0,i} + \Delta r_i \cdot \epsilon_{r0,i} \tag{3.86}$$

$$\alpha_{0,i+1} = \alpha_i + \Delta r_i \cdot \alpha'_i \tag{3.87}$$

By following the procedure shown in the paper by Schilhansl [11] the radial force and moment are expressed as a function of the radial displacement (u_0), turning angle (α), the unit elongation radial (ϵ_{r0}) and rotational (α') components, and the relative temperature at the radial location of the volume element (ΔT):

$$S = s_\epsilon \cdot \epsilon_{r0} + s_\beta \cdot \alpha' + s_u \cdot u_0 + s_\alpha \cdot \alpha + s_T \tag{3.88}$$

$$M = m_\epsilon \cdot \epsilon_{r0} + m_\beta \cdot \alpha' + m_u \cdot u_0 + m_\alpha \cdot \alpha + m_T \tag{3.89}$$

All terms related to thermal expansion are lumped in the constants s_T and m_T. The terms related to thermal expansion, for each volume element 'i' are derived as follows with the assumption that the effective blade thickness ($t_{B,eff}$) is constant along the z axis:

$$m_{T,i} = E\alpha_{\exp,i}\Delta T \left(t_{B,i,eff} \cdot \frac{\left(z_{2,i}^2 - z_{1,i}^2\right)}{2} + \frac{1}{1-\nu^2} \cdot r_i \Delta\Phi \cdot \frac{\left(z_{3,i}^2 - z_{2,i}^2\right)}{2} (1+\nu) \right) \tag{3.90}$$

$$s_{T,i} = -E \cdot \alpha_{\exp,i} \cdot \Delta T \left(t_{B,i,eff} \left(z_{2,i} - z_{1,i}\right) + \frac{1}{1-\nu^2} \cdot r_i \cdot \Delta\Phi \cdot \left(z_{3,i} - z_{2,i}\right) \cdot (1+\nu) \right) \tag{3.91}$$

Equations 3.88 and 3.89 can be then manipulated to find explicit relations for the quantities ϵ_{r0} and α':

$$\epsilon_{r0} = \epsilon_S \cdot S + \epsilon_M \cdot M + \epsilon_u \cdot u_0 + \epsilon_\alpha \cdot \alpha + \epsilon_T \tag{3.92}$$

$$\alpha' = \alpha_S \cdot S + \alpha_M \cdot M + \alpha_u \cdot u_0 + \alpha_\alpha \cdot \alpha + \alpha_T \tag{3.93}$$

Where the terms related to the radial displacement (ϵ_u, α_u), turning angle ($\epsilon_\alpha, \alpha_\alpha$), the radial force ($\epsilon_s, \alpha_s$) and moment ($\epsilon_M, \alpha_M$) are reported in Appendix C, while all terms related to thermal expansion are lumped in the constants ϵ_T and α_T, which are defined as follows:

$$\epsilon_{T,i} = -\frac{m_{T,i} \cdot s_{\beta,i} - m_{\beta,i} \cdot s_{T,i}}{m_{\epsilon,i} \cdot s_{\beta,i} - m_{\beta,i} \cdot s_{\epsilon,i}} \tag{3.94}$$

$$\alpha_{T,i} = -\frac{m_{\epsilon,i} \cdot s_{T,i} - m_{T,i} \cdot s_{\epsilon,i}}{m_{\epsilon,i} \cdot s_{\beta,i} - m_{\beta,i} \cdot s_{\epsilon,i}} \tag{3.95}$$

Equations 3.84 to 3.87 can then be re-arranged following the same procedure by Ray et al. [9], thus obtaining the linear that has to be solved for each element in order to compute forces and displacements:

$$S_{i+1} = P_i \cdot u_{0,i} + Q_i \cdot \alpha_i + (1 + R_i) \cdot S_i + X_i \cdot M_i + Y_i \tag{3.96}$$

$$M_{i+1} = P'_i \cdot u_{0,i} + Q'_i \cdot \alpha_i + R'_i \cdot S_i + (1 + X'_i) \cdot M_i + Y'_i \tag{3.97}$$

$$u_{0,i+1} = P''_i \cdot u_{0,i} + Q''_i \cdot \alpha_i + R''_i \cdot S_i + X''_i \cdot M_i + Y''_i \tag{3.98}$$

$$\alpha_{i+1} = P'''_i \cdot u_{0,i} + Q'''_i \cdot \alpha_i + R'''_i \cdot S_i + X'''_i \cdot M_i + Y'''_i \tag{3.99}$$

Where the Y_i parameters are defined as:

$$\begin{bmatrix} Y_i \\ Y'_i \\ Y''_i \\ Y'''_i \end{bmatrix} = \begin{bmatrix} -\Delta c_i + \Delta T_{T,i} \\ \Delta c_i \cdot c_i + \Delta G_{T,i} \\ \Delta r \cdot \epsilon_T \\ \Delta r \cdot \alpha_T \end{bmatrix} \tag{3.100}$$

With the parameters $\Delta T_{T,i}$ and $\Delta G_{T,i}$ being, respectively, the contributions given by thermal expansion to the force (T_i) [2] and moment (G_i) (as shown in Figure 3.43). These quantities are made up by two contributions: one only dependent on mechanical forces (T_0,G_0) and the other, described above, only dependent on thermal expansion, namely:

$$T = 2\Delta r \sin\left(\frac{\Delta\Phi}{2}\right) \cdot \int_{z_2}^{z_3} \sigma_{t,D} dz = T_0 + \Delta T_T \tag{3.101}$$

$$G = -2\Delta r \sin\left(\frac{\Delta\Phi}{2}\right) \cdot \int_{z_2}^{z_3} \sigma_{t,D} z dz = G_0 + \Delta G_T \tag{3.102}$$

The terms T_0 and G_0 are only a function of the mechanical stress and have the same definitions as T and G according to Schilhansl [11], whereas ΔT_T and ΔG_T are defined as follows:

$$\Delta T_T = -\frac{E}{1-\nu^2} \cdot 2\Delta r \sin\left(\frac{\Delta\Phi}{2}\right) \cdot \left[(z_3 - z_2)\left(\alpha_{\exp}(1+\nu)\Delta T - \nu\epsilon_T\right) + \frac{z_3^2 - z_2^2}{2}\nu\alpha_T \right] \tag{3.103}$$

$$\Delta G_T = \frac{E}{1-\nu^2} \cdot 2\Delta r \sin\left(\frac{\Delta\Phi}{2}\right) \cdot \left[\frac{z_3^2 - z_2^2}{2}\left(\alpha_{\exp}(1+\nu)\Delta T - \nu\epsilon_T\right) + \frac{z_3^3 - z_2^3}{3}\nu\alpha_T \right] \tag{3.104}$$

Now that all the parameters in the system of equations 3.96 through 3.99 have been defined, the equations can be arranged into a linear system for each element discretizing radially the disk. This system of equations is first solved for the element at the hub ($i = 0$) and ending at the tip of the disk ($i = N$):

[2] the vertical component of the tangential force in the disk

$$\begin{bmatrix} S_{i+1} \\ M_{i+1} \\ u_{0,i+1} \\ \alpha_{i+1} \end{bmatrix} = \begin{bmatrix} (1+R_i) & X_i & P_i & Q_i \\ R_i' & (1+X_i') & P_i' & Q_i' \\ R_i'' & X_i'' & P_i'' & Q_i'' \\ R_i''' & X_i''' & P_i''' & Q_i''' \end{bmatrix} \begin{bmatrix} S_i \\ M_i \\ u_{0,i} \\ \alpha_i \end{bmatrix} + \begin{bmatrix} Y_i \\ Y_i' \\ Y_i'' \\ Y_i''' \end{bmatrix} \Rightarrow U_{i+1} = A_i U_i + C_i \tag{3.105}$$

The boundary conditions for the stress analysis are imposed either by specifying the forces and moments at the hub (S_0, M_0) and no forces or moments at the tip ($S_N = 0$, $M_N = 0$) [9, 11, 10].

The forces and moments at the hub (S_0, M_0) can either be set equal to 0 if there is no bearing pressure,or greater than zero if the disk is mounted with interference on the shaft. At the tip, Sn a Mn are, instead, always equal to zero.

The boundary conditions of the system of equations are specified then at two different boundaries, the surface of the disk bore and at disk tip. To avoid the implementation of an iterative solution scheme, the recurring system of equations computing the forces and displacements for each element (U_i) is manipulated so that U_N is expressed as a function of U_0:

$$U_N = A_N U_{N-1} + C_N = B_N U_0 + D_N \tag{3.106}$$

Where B_N is a 4 by 4 matrix obtained by multiplying all A_i matrices and D_N is a 4 element vector calculated from the recurring relation shown in Equation 3.108:

$$B_N = A_N A_{N-1} ... A_1 A_0 \tag{3.107}$$

$$D_N = A_N D_{N-1} + C_N \, , \; D_0 = C_0 \tag{3.108}$$

The system of equations thus obtained can be written as follows:

$$U_N = B_N U_0 + D_N \Rightarrow \begin{bmatrix} S_N \\ M_N \\ u_{0,N} \\ \alpha_N \end{bmatrix} = \begin{bmatrix} b_{1,1} & b_{1,2} & b_{1,3} & b_{1,4} \\ b_{2,1} & b_{2,2} & b_{2,3} & b_{2,4} \\ b_{3,1} & b_{3,2} & b_{3,3} & b_{3,4} \\ b_{4,1} & b_{4,2} & b_{4,3} & b_{4,4} \end{bmatrix} \begin{bmatrix} S_0 \\ M_0 \\ u_{0,0} \\ \alpha_0 \end{bmatrix} + \begin{bmatrix} d_1 \\ d_2 \\ d_3 \\ d_4 \end{bmatrix} \tag{3.109}$$

So the missing quantities at the hub can be easily calculated from this system, as both the forces and moments at the hub (S_0, M_0) and at the tip (S_N, M_N) are known boundary conditions:

$$u_{0,0} = \frac{b_{1,4}(M_N - b_{2,1}S_0 - b_{2,2}M_0 - d_2) - b_{2,4}(S_N - b_{1,1}S_0 - b_{1,2}M_0 - d_1)}{b_{1,4}b_{2,3} - b_{2,4}b_{1,3}} \tag{3.110}$$

$$\alpha_0 = \frac{S_N - b_{1,1}S_0 - b_{1,2}M_0 - b_{1,3}u_{0,0} - d_1}{b_{1,4}} \tag{3.111}$$

Once all the boundary conditions are known at the hub, the system 3.109 can then be solved for each element from the disk hub to the tip.

3.3.3. BLADE THICKNESS ADJUSTMENT

The methodology used to discretize the impeller disk into finite elements requires that the disk is first subdivided into a number of angular sectors equal to the number of blades. This allows for the stress calculation to take into account the contributions that the mass of the blades has on centrifugal forces.

Moreover, the blades are assumed to be all radial oriented for the purpose of the disk discretization. If the blade thickness in each radial position is taken as the nominal thickness (calculated in section 3.1.13), the estimation of the mass of the blades, and consequently of their contribution to the centrifugal stress, will not be accurate.

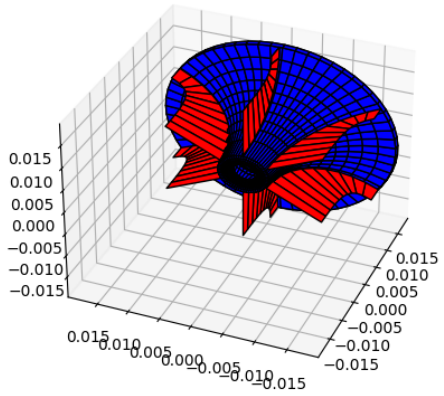

Figure 3.28: Geometry of the disk and blades as 'seen' by the stress analysis method of the impeller of the first stage radial compressor from the paper by A.Giuffrè et al. [12]

In order to increase the accuracy of this estimation a correction can be applied to the blade thickness distribution to take into account blade angles such that for each blade element 'i':

$$t_{B,i,corr} = \frac{t_{B,i}}{\beta_{bl,i}} \tag{3.112}$$

Where $\beta_{bl,i}$ is the average blade angle at the radial position corresponding to the blade element.

Furthermore the discretization method described above does not allow for the modelling of blades that do not span the full length of the flow path (such as splitter blades). For this reason the effective blade thickness in each disk element is further corrected to include also the mass of splitter blades, by using the following relation:

$$t_{B,i,eff} = t_{B,i,corr,full} + t_{B,i,corr,splitter} \cdot \frac{L_{axi,i,splitter}}{L_{axi,i,full}} \tag{3.113}$$

Where $L_{axi,i,splitter}$ and $L_{axi,i,full}$ are the lengths in the axial direction of the splitter and full blades at the radial position of the element 'i'.

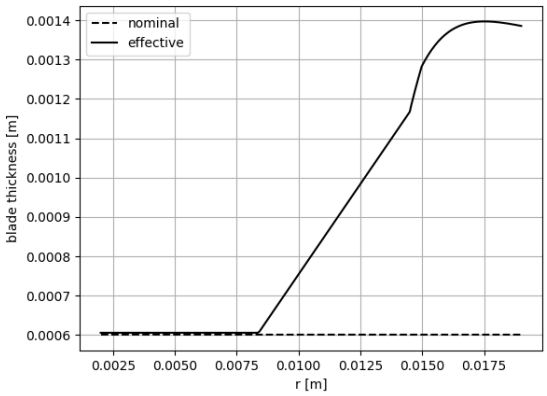

Figure 3.29: Blade thickness correction applied to the impeller of the first stage radial compressor from the paper by A.Giuffrè et al. [12]

3.3.4. DISK TEMPERATURE DISTRIBUTION

In order to calculate the stress distribution in the impeller disk, the temperature at each radial location has to be specified. No standard temperature distributions for radial compressor disks could be inferred from

the literature; some papers, such as by Zheng et al. [10] and Murkherjee and Baker [55] provide examples of temperature distributions in radial impellers, but the reported trends cannot be generalized.

A further limitation of the implemented stress analysis methodology is that temperature can vary only in the radial direction. This implies that each element is assumed of uniform temperature.

To a first approximation, trying to approximate he trend reported in literature, the temperature distribution in the impeller disk is thus taken as illustrated in Figure 3.30. The temperature is considered to be constant in the disk region below the impeller inlet hub radius and equal to the inlet static temperature (T_1), and increasing linearly throughout the disk until reaching the fluid outlet static temperature (T_2) at the rim.

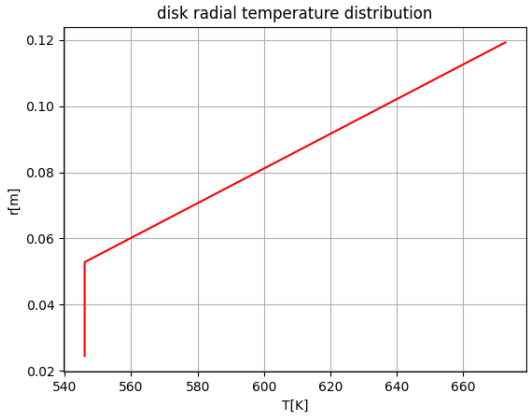

Figure 3.30: Example of the radial temperature distribution on an impeller disk (T700 radial compressor stage, section 4.5.2)

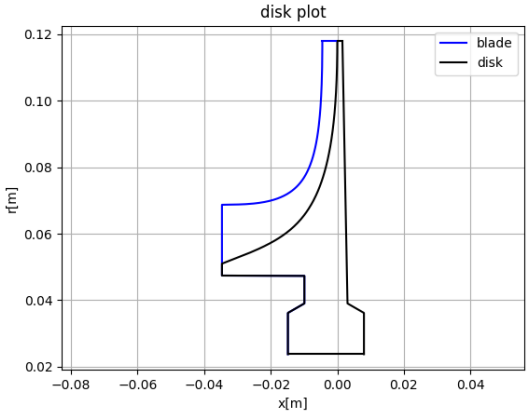

Figure 3.31: Radial compressor stage model

3.3.5. MECHANICAL STRESS VALIDATION

To verify the correct implementation of the mechanical stress analysis methodology, the examplary test cases provided by Ray et al. [9] were reproduced as accurately as possible and the resulting stress distribution compared with that in the original paper.
The paper by Ray et al. [9] does not provide a distribution of the actual stress for these test cases, but a non-dimensional equivalent stress, the so called stress coefficient (σ^*), which is defined as follows:

$$\sigma^* = \frac{\sigma}{\rho_{mat}\omega^2 r_T^2} \tag{3.114}$$

Where ρ_{mat} is the density of the disk material, ω is the rotational speed of the disk and r_T is the disk tip radius.

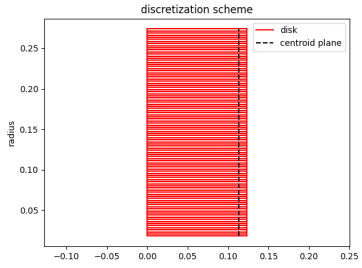

Figure 3.32: Discretization scheme of the disk using 100 slices

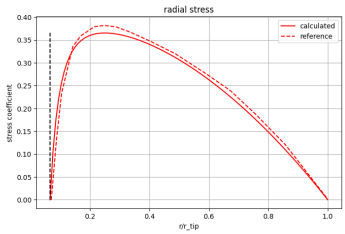

Figure 3.33: Calculated radial stress distribution compared to the result given by Ray et.al. [9]

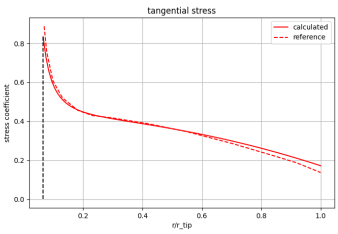

Figure 3.34: Calculated tangential stress distribution compared to the result given by Ray et.al. [9]

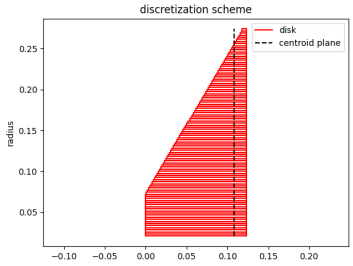

Figure 3.35: Discretization scheme of the disk using 100 slices

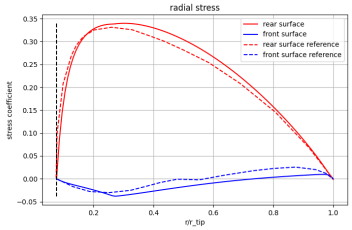

Figure 3.36: Calculated radial stress distribution compared to the result given by Ray et.al. [9]

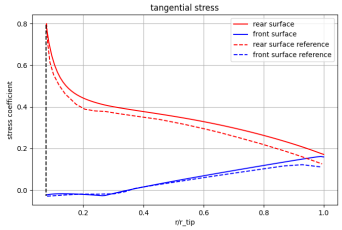

Figure 3.37: Calculated tangential stress distribution compared to the result given by Ray et.al. [9]

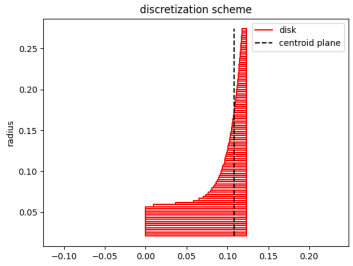

Figure 3.38: Discretization scheme of the disk using 100 slices

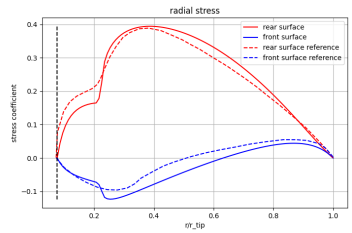

Figure 3.39: Calculated radial stress distribution compared to the result given by Ray et.al. [9]

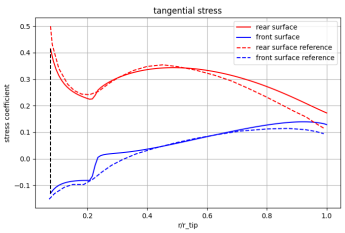

Figure 3.40: Calculated tangential stress distribution compared to the result given by Ray et.al. [9]

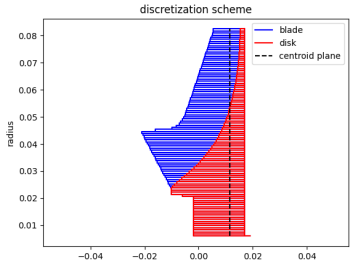

Figure 3.41: Discretization scheme of the disk using 100 slices

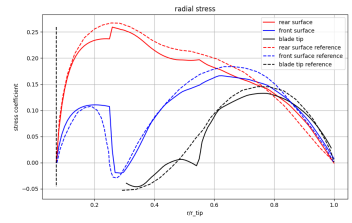

Figure 3.42: Calculated radial stress distribution compared to the result given by Ray et.al. [9]

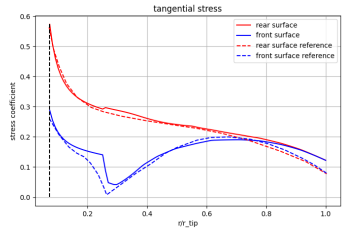

Figure 3.43: Calculated tangential stress distribution compared to the result given by Ray et.al. [9]

The calculated stress distributions match very well with the reference. Small deviations can be easily explained by differences in the discretization scheme and small variations in geometry, as the geometry of the various test cases and the reference stress distributions were obtained by digitization of the pictures provided in the paper, which may not be completely accurate.

The comparison is considered satisfactory thus proving the correct implementation of the mechanical stress analysis procedure.

3.3.6. THERMAL STRESS VALIDATION

The calculation method for thermal stresses in compressor disks is not as simple to validate, as very limited data is available in literature on thermal stress distribution in disks with non symmentric thickness distributions. The papers by Zheng [10] and Mukherjee and Baker [55] provide thermal stress distributions obtained through finite element analyses, but it is impossible to retrieve useful information from these source as the stresses are shown through 3D contour plots projected on the CAD model of the compressor impeller; furthermore it is difficult to reproduce the geometry used in these studies, as dimensions are not (or not completely) provided. For these reasons it is not possible to compare the results obtained in these papers with finite element methods with those of the method implemented in this work.

Thus, a FEM model of the first stage of the compressor from the paper by A.Giuffrè et.al. [12] was used to generate the data needed to validate the thermal stress calculation procedure. This model was provided by the authors of the paper, and does not completely match with what is shown in the publication. The geometry of the impeller (Figure 3.44) was reproduced as good as possible given the limitations of the geometry generation method of the simplified stress analysis program (3.45), and the same boundary conditions were applied in both models.

At the same time, the thermal gradient has been exaggerated in order to increase its effect on the calculated stress and to make it easier for the simplified code to match the boundary conditions. The objective of this test is to validate the method, not the results. Moreover, in both the finite element analysis and the simplified method, fluid forces acting on the blades and on the front of the disk are not taken into account. According to Zheng [10], their effect should be negligible with respect to that of the thermal and centrifugal stresses and is mainly concentrated in the blades and blade roots, which can only be poorly modelled by the simplified design method in WEST.

Finally, note that the temperature distribution in the impeller of a real radial compressor is much more complex than that considered in this analysis, and requires a detailed modelling of the heat transfer with the fluid. This is not possible to model using a preliminary design tool like WEST.

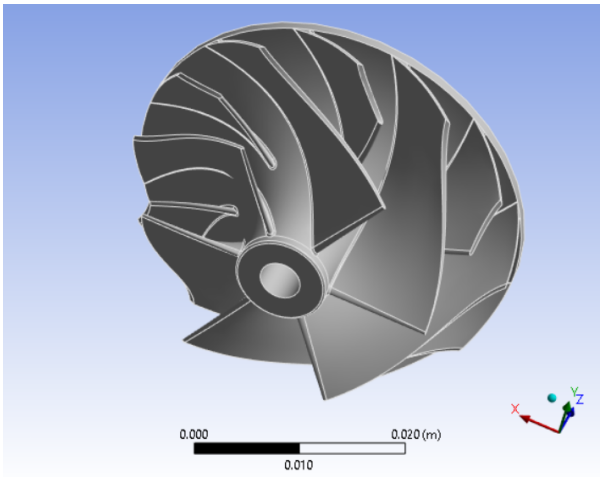

Figure 3.44: Model of the compressor in ANSYS mechanical

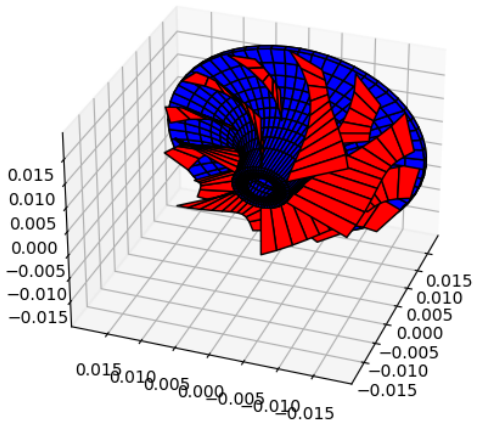

Figure 3.45: Model of the compressor reproduced using the program

The temperature distribution in the disk is calculated by ANSYS given the two fixed temperature boundary conditions at the hub and at the tip of the disk,22^oC and 122^oC, respectively, see Figure 3.46. The resulting temperature distribution in the impeller is shown in figure 3.47.

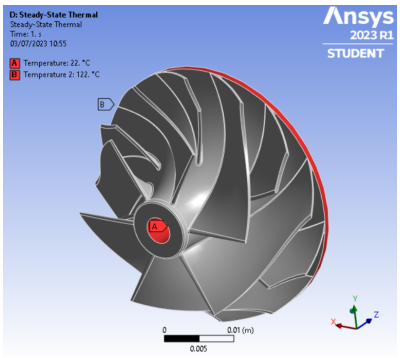

Figure 3.46: Boundary conditions specified for the thermal calculation

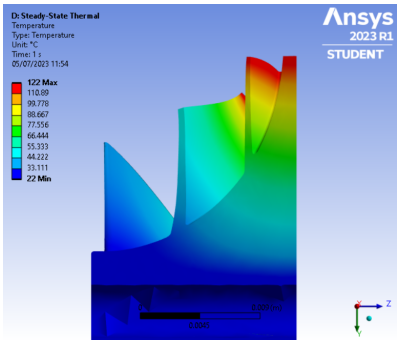

Figure 3.47: temperature distribution in the compressor disk

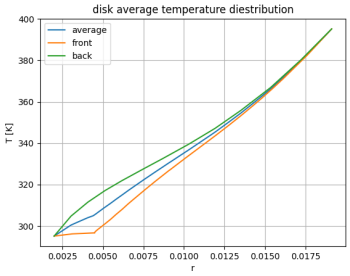

Figure 3.48: radial temperature distribution in the compressor disk

The FEM stress analysis results are calculated based on the temperature distribution. The simplified model can only account for a radial temperature difference. The temperature at each radial position in the simplified model is thus set equal to the average temperature calculated by the FEM model at the same position, shown in Figure 3.48.

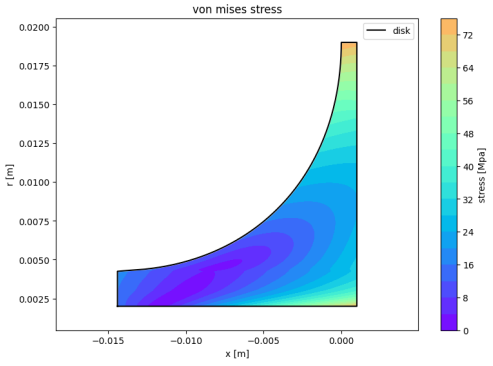

Figure 3.49: Von Mises stress contour in the impeller disk calculated with the simplified method

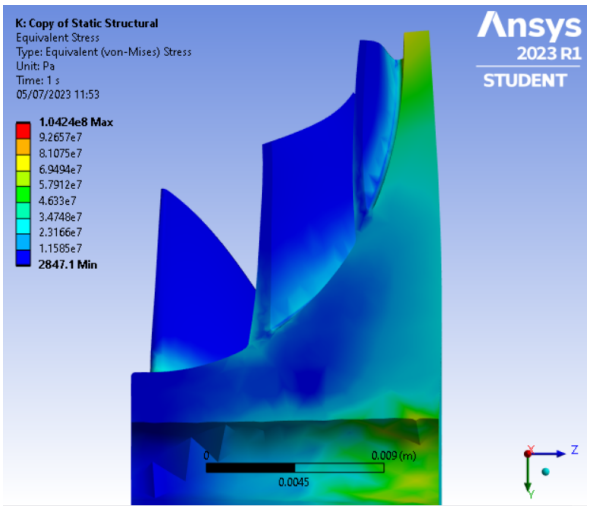

Figure 3.50: Von Mises stress contour in the impeller disk

As can be clearly seen from Figures 3.49 and 3.50, the equivalent Von Mises stress distribution caused by thermal expansion inside the impeller disk is predicted quite well by the simplified method compared to the finite element method analysis. The main differences between the two stress distributions are located towards the front of the disk, as the effect on the stresses due to the presence of the blade roots is not evaluated by the simplified method. Only the contribution of the blade to the overall thermal expansion is taken into account.

The geometry of the blades is not perfectly matched by the program. The blade attachment begins exactly at the front face of the disk for the simplified method while this is not the case for the real impeller, see Figure 3.44. Given the simplicity of the discretization scheme, the shape of the blade has to be simplified.

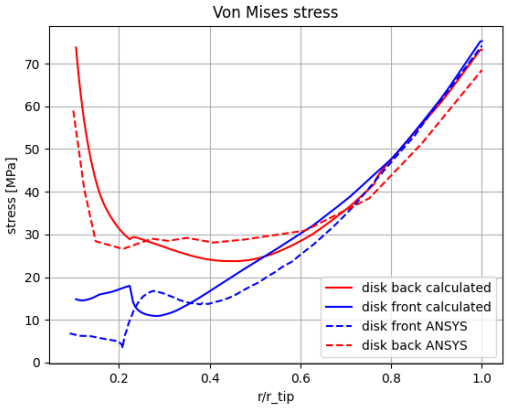

Figure 3.51: Von Mises stress distributions on the front and back of the impeller disk

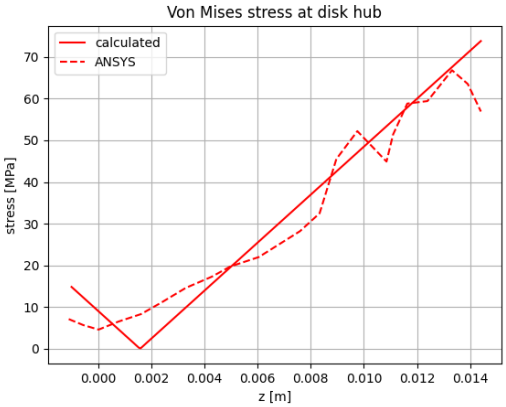

Figure 3.52: Von Mises stress distribution at the hub of the impeller disk

The front and back stress distributions calculated with the two models are shown in Figure 3.51. The profile reported for the FEM model was obtained by sampling from the FEM results a series of points along a line that follows the flow channel at equal distance between the blades. The reported stress distribution may be influenced by the stresses in the blade attachment region, which cannot be modelled with the simplified method; furthermore the maximum stress point at the hub of the disk is on the back edge of the hub according to the simplified method, while further towards the front according to the finite element analysis. The maximum stress point calculated by the simplified method is always expected to be at either the front or back of the disk, due to the linear nature of the stress distribution calculated at each axial position of each slice.

Overall, the ability of the simplified stress analysis method to predict the maximum thermal stress and its approximate location caused by a temperature gradient along the radial direction of the impeller disk was considered satisfactory for the needs of the WEST tool.

3.3.7. COMBINED EFFECT OF THERMAL AND CENTRIFUGAL STRESSES - MODEL VALIDATION

To validate the implemented stress analysis method in the case of both thermal and centrifugal stresses a second FEM analysis was executed following the procedure described in Section 3.3.6. The difference lies in the impeller rotational that is set to $\Omega = 10996\ RAD/s$.

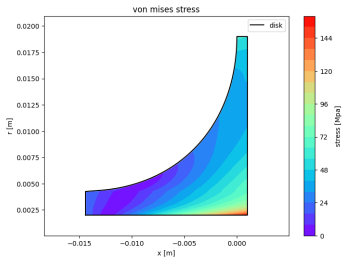

Figure 3.53: Von Mises stress contour in the impeller disk calculated with the simplified method

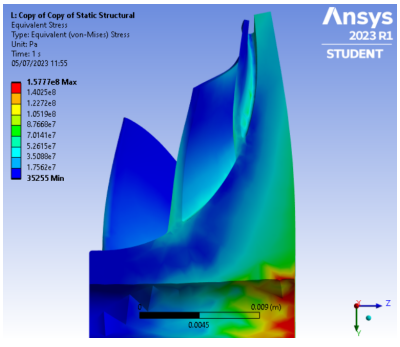

Figure 3.54: Von Mises stress contour in the impeller disk

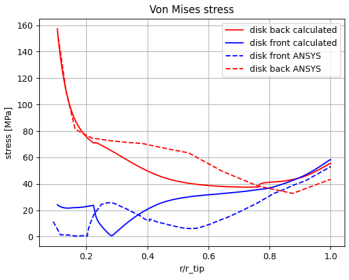

Figure 3.55: Von Mises stress distributions on the front and back of the impeller disk

Similarly to what was observed before for the thermal stresses alone, the simplified method correctly predicts the approximate location of the maximum stress and its intensity, as well as the trend of the overall distribution, as can be clearly observed by comparing Figures 3.53 and 3.54. The main differences with the FEM analysis still occurs in the locations of the blade roots, as can be seen in Figure 3.55. This is then the main limitation of the simplified method.

The results obtained with the simplified method are however still considered to be satisfactory for the

purposes of the WEST tool.

3.3.8. SENSITIVITY ANALYSIS

The stress analysis method for the impeller disk requires the its discretization into volume elements. In this section it will be discussed how the number of this elements influences the calculated stress distribution along the radial direction of the disk.

For the purpose of this analysis, the design of a radial impeller similar to that of the turboshaft GE-T700 was chosen as test case, see Figure 3.56. The geometry was discretized using an increasing number of elements and the stress distribution calculated for each discretization.

Increasing the number of elements results in increased precision in the stress distribution calculation, but also in higher computational cost of the analysis. The objective of this section is to estimate the optimal amount of volume elements that guarantees the best trade-off between precision and computational efficiency.

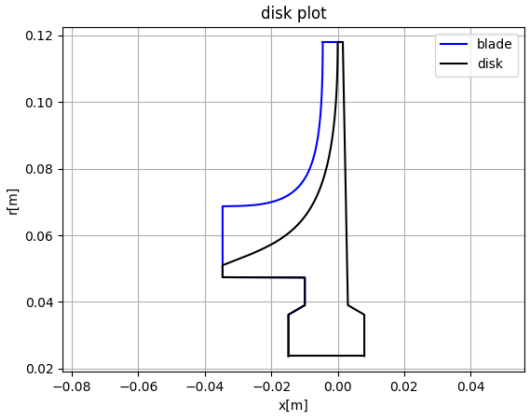

Figure 3.56: radial compressor stage model

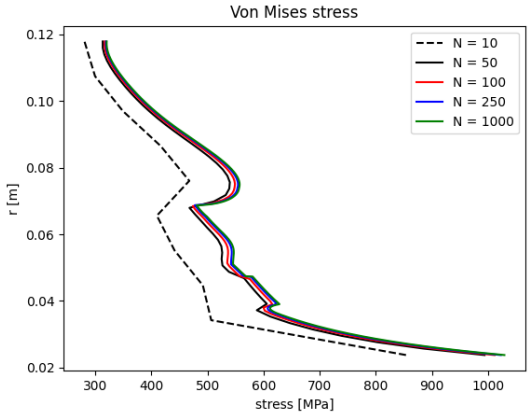

Figure 3.57: Maximum Von Mises stress radial distribution for different volume element numbers

Element Number [-]	Average Iteration Time of the optimization [s]	Maximum Von Mises Stress of the optimization [MPa]
10	0.0020	854
50	0.0997	994
100	0.0190	1012
250	0.0459	1023
1000	0.2184	1029
10000	1.9218	1031

Table 3.6: Sensitivity analysis results

In figure 3.57 it can be observed that the calculated stress distribution does not substantially change if the number of elements exceeds 100. The best trade-off between computational efficiency and solution precision can be achieved with an element count between 100 and 250. The minimum amount of elements required for an acceptable result is considered to be 100: the maximum stress is less than 2% lower than that calculated with 10000 elements, but the iteration time is less than 1% of that observed for the discretization with the highest number of elements.

3.3.9. ADAPTATION OF THE METHOD FOR AXIAL TURBOMACHINERY DISKS

The stress analysis method discussed in this section is based upon the same principles of the method described by Lolis [26] and Tong et al. [51], but instead of requiring an iterative calculation scheme to solve the boundary-value problem, the stress distribution is calculated explicitly in a single iteration. This should lead to a considerable reduction in computational cost of the WEST tool if the newly developed stress calculation procedure is adapted to analyze axial turbomachinery disks as well.

Additional computational efficiency can be gained by further simplifying the method, given that for axial turbomachinery disks, the profile is assumed symmetric with respect to the axial direction, and thus the centrifugal loads are always aligned radially for each volume element. This means that there is no moment generated by centrifugal loads. Thus there is no need to calculate the equilibrium of moments at each element interface and the angular displacement of each element is always zero.

The system of equations of each element can thus be simplified (based on Equation 3.109)as follows where each parameter is defined in the same way as discussed in section 3.3.2:

$$\begin{bmatrix} S_{i+1} \\ u_{0,i+1} \end{bmatrix} = \begin{bmatrix} (1+R_i) & P_i \\ R_i'' & P_i'' \end{bmatrix} \begin{bmatrix} S_i \\ u_{0,i} \end{bmatrix} + \begin{bmatrix} Y_i \\ Y_i'' \end{bmatrix} \Rightarrow U_{i+1} = A_i U_i + C_i \tag{3.115}$$

The boundary conditions of the problem for axial turbomachinery disks are set up differently compared to radial turbomachines. In axial stage disks the rim stress is known, given by the centrifugal force contribution of the blades attached to the disk, while the hub radial stress is 0. By following the same procedure used to make the system of equation 3.106-3.108 explicit, the boundary condition needed at the hub is calculated as follows:

$$u_{0,0} = \frac{S_N - d_1 - b_{1,1} \cdot S_0}{B_{1,2}} \tag{3.116}$$

This new numerical scheme should improve the overall computational efficiency of the stress distribution calculation; since all parameters are calculated explicitly, the method requires more initial calculations than its iterative counterpart, but the total number of operations should still be lower as no iteration is necessary.

3.3.10. COMPARISON BETWEEN THE METHODS

The test case chosen to test the two methods is the high pressure turbine of the CFM-56 turbofan (Figure 3.58), previously analysed by I.Boersma [23].The required model inputs are reported in Table 3.7.

Duty Coefficient	Unit	Value
Flow coefficient,ϕ	[-]	0.411
Work coefficient, ψ	[-]	1.472
Degree of reaction, R	[-]	0.477
Thermodynamic	**Unit**	**Value**
$\dot{m}$	[kg/s]	59.6
$\dot{W}$	[MW]	26.16
Ω	[RPM]	15183
$T_{t,in}$	[K]	1522.0
$P_{t,in}$	[bar]	26.5
$T_{cooling}$	[K]	855.6
General Design	**Unit**	**Value**
Stage Count	[-]	1
Fixed Diameter	[-]	Mid
Zweifel Coefficient, Ψ_Z	[-]	0.7
Cooled Blades	[-]	True
Geometry	**Unit**	**Value**
Row Gap	[-]	0.567
Rotor Taper Ratio	[-]	1
Rotor Aspect Ratio	[-]	1.73
Stator Taper Ratio	[-]	1
Stator Aspect Ratio	[-]	0.9
Disk Type	[-]	Web
$r_{sh,max}$	[m]	0.058
Material	**Unit**	**Value**
Stator Vane	[-]	NI 105
Rotor Blade	[-]	NI 105
Disk Material	[-]	NI 105
Casing Material	[-]	NI 105

Table 3.7: Input parameters for the turbine design

The design of this turbine stage was repeated with different element counts using both stress analysis methodologies. The computed stress distribution using both the methods completely overlaps for element counts above 100, as shown in Figure 3.59.

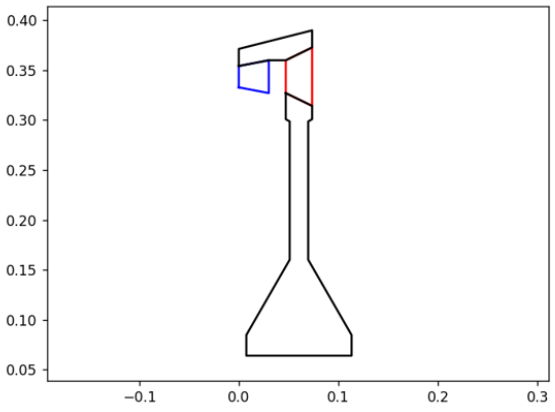

Figure 3.58: axial turbine stage

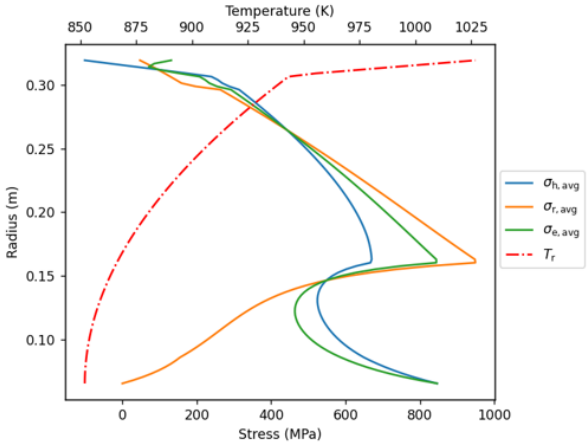

Figure 3.59: stress and temperature distribution in the turbine stage disk

Element Number [-]	Computation Time New Method [s]	Computation Time Previous Method [s]
100	13.57	22.39
250	14.77	51.38
1000	90.46	217.48

Table 3.8: Computation time comparison with different element count (these times may vary depending on the hardware and the behaviour of the gradient-based optimization)

While some variation is expected due to the iterative nature of the original disk design method, the characteristics of the numerical problem as well as the settings of the gradient-based optimization of the disk adopted in both design procedures can influence the required computation time as they may influence the number of function evaluations needed for the convergence of the optimizer. Table 3.8 still shows that, as expected, the explicit method is more computationally efficient and reduces the optimization time by a factor between 2 and 4, depending on the element count and on the efficiency of the optimizer.

3.4. CASING DESIGN

Casings are an integral part of the gas path channel in gas turbine engines and must be capable of withstanding the high pressures generated by the working fluid. Their design should also consider the containment of blade fragments in the event of blade failure and detachment, as blades have substantial kinetic energy due to the high rotational speeds of the compressor.

The energy released from disks and/or disk fragments is typically very high and cannot be neglected in the casing design. While certain detailed aspects of casings, such as flanges, connecting hardware, and actuators for variable stator vanes, might not be modeled in the current methodology, it is still possible to estimate the overall casing weight by calculating its local thickness.

Bretschneider et al. [56] developed a simplified method for the sizing and preliminary design of the casing of axial compressors based on various requirements imposed by the flow conditions inside the machine and the structural integrity of the component (blade containment and axial stiffness). Even if it was developed for axial machines, the method can be easily adapted to model the casing of a radial compressor as the design requirements remain the same.

3.4.1. CASING GEOMETRY

The radial compressor casing can be divided into three sections, in which the casing thickness has to meet different requirements, as shown in figure 3.60. These sections are: the impeller casing, which follows the shape of the tip of the blades of the impeller, the diffuser casing,and the 90^o bend, which connects the radial compressor stage with the downstream components, and occupies the space between the vaned diffuser outlet radius and the maximum outer radius of the stage.

The method used to calculate the weight of the curved sections of the casing, such as the impeller casing or the 90 degree bend, is reported in appendix D.

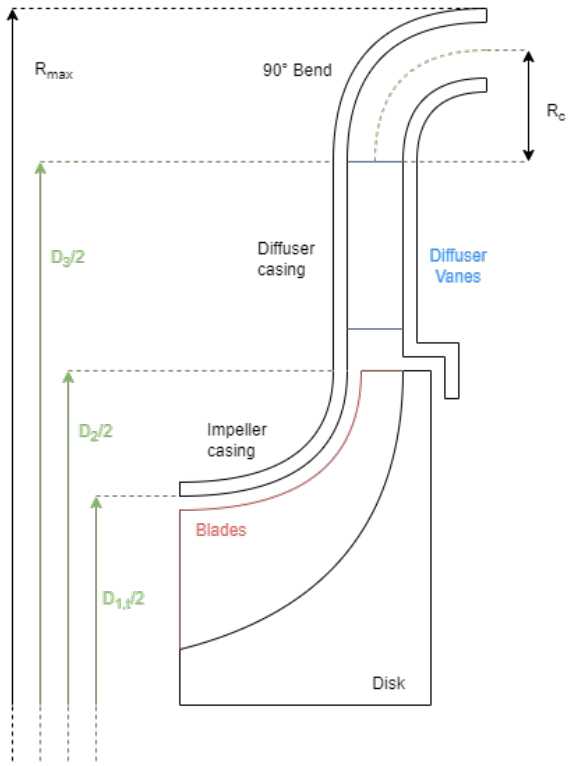

Figure 3.60: Illustration of the simplified Geometry of the radial compressor stage casing modelled by WEST

3.4.2. CASING THICKNESS

By observing various turboshaft engines and auxiliary power units reproduced in literature [57, 18, 58] it was determined that the thickness distribution of the casing of the radial compressor can be divided into two sections of uniform thickness, one in correspondence of the impeller casing section, and the other for the diffuser and 90^o bend. The thickness of these sections is set to the maximum local thickness required to meet the correct combination of one or both of the design requirements.

PRESSURE CONTAINMENT

The casing thickness necessary for pressure containment, denoted as t_{pres}, can be determined using equation 3.117 provided by Lolis [26].

$$t_{pres} = SF \cdot \frac{p \cdot r}{\sigma_y} \tag{3.117}$$

Where p represents the static pressure acting on the casing, and for each of the three previously outlined sections the static pressure is considered to be the maximum static pressure within the section, as computed by the meanline analysis; r denotes the local radius, and σ_y is the yield strength of the material. Optionally, an additional safety factor (SF) may be included, although its significance is minimal given that the thickness required to contain blade fragments far exceeds that needed for pressure containment [56].

BLADE CONTAINMENT

The thickness required for blade containment is calculated following the method by Bretschneider et al. [56] as the thickness required for the casing material to absorb the blade impact in case of complete detachment.

The kinetic energy of the blade ($E_{kin,bl}$) is calculated as shown in equation 3.118.

$$E_{kin,bl} = \frac{m_{bl} \cdot r_{cg,bl}^2 \cdot \omega^2}{2} \tag{3.118}$$

Where $r_{cg,bl}$ is the radial location of the center of gravity of the blade, which can be easily calculated given its mass and geometry.

The required casing thickness is defined in equation 3.119 as provided by Bretschneider et al. [56].

$$t_{con,bl} = S_1 \cdot \sqrt{\frac{E_{kin,bl}}{0.65 \cdot \xi \cdot \sigma_{max,bn} \cdot (\nu + \mu + \kappa/2) \cdot l^*}} \tag{3.119}$$

Where the parameters ν, ψ and κ are empirically derived coefficients, and they represent the ductile, elastic and shear portion respectively of the overall deformation energy and are defined as $\nu = 0.7$, $\psi = 0.05$ and $\kappa = 2.5$ [56].

The product $0.65 \cdot \xi \cdot \sigma_{max,bn}$ in equation 3.119 represents the maximum impact strength, where $\xi = 1.3$ is the so-called consolidation coefficient, another empirically derived parameter, and $\sigma_{max,bn}$ is the maximum bending stress of the material, which can be considered to be equal to the yield stress (σ_y).

The reference length, l^*,is chosen as the perimeter length of the blade tip, since this is the point of impact of the rotor blade [56]. This can be estimated as two times the length of the 3D curve representing the tip of the blade as discussed in section 3.1.12, as the thickness of the blade does not play a relevant role in the determination of the perimeter given the typical centrifugal compressor blade thickness.

3.4.3. 90^o BEND

If the radial compressor stage has to be connected to other turbomachinery components in the axial direction, as commonly occurring in turboshaft engines, a 90^o bend section has to be attached at the outlet of the vaned diffuser.

The design of this section follows a procedure similar to that described by Aungier [13], with the additional assumption that the height of the channel stays constant throughout the bend.

Aungier [13] suggests that the radius of the inner portion of the bend (also shown in figure 4.4) should be equal to the flowpath height at the outlet of the diffuser, otherwise a maximum outer radius may be be provided. In that case the bend radius would be adapted to match this geometry constraint.

As along this duct section there is a slight change in the flow path cross-sectional area, the kinematic quantities at the outlet of the bend are updated accordingly based on mass conservation.

4

MODELLING OF TURBOSHAFT ENGINES

This chapter will discuss how the developed component model for radial compressor stages has been integrated with the existing WEST modules, and how it can be used to model small and medium scale turboshaft engines.

For this purpose some additional components have been modelled. These are: the return channel that connects the stages together in case there is more than one radial compressor stage (Section 4.1) and the reverse-flow combustor which is often a design feature of the more compact turboshaft engines (Section 4.2); furthermore some small tweaks were done to the existing methodology in order to attempt to model some particular characteristics of existing engines (Section 4.3).

The designs of two existing turboshaft engines, the MTU Turbomeca Rolls-Royce MTR390 and the General Electric T700 have been simulated to validate the geometry prediction and weight estimation capabilities of the WEST software (Sections 4.5.1 and 4.5.2).

The model of the MTU Turbomeca Rolls-Royce MTR390 was then used to estimate the impact that design parameters such as turbine inlet temperature, mass flow rate and overall pressure ratio have on the engine design.

4.1. RETURN CHANNEL

If more than one radial compressor stage is present (as is the case for the MTR 390 turboshaft, which will be discussed in depth in section 4.5.1), a return channel has to be included to connect the outlet of the first radial compressor stage to the following one.

This return channel has the function of guiding the flow between the stages and changing the flow angle to match the inlet requirement of the following radial compressor stage. This is accomplished by means of vanes, similarly to a vaned diffuser.

A design procedure for this component is provided by R.H. Aungier [13, 14]. It involves multiple geometrical design parameters as shown in figure 4.4.

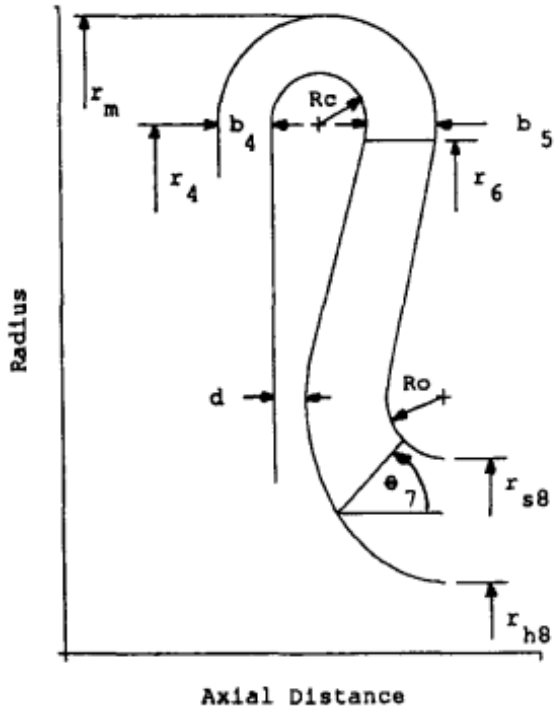

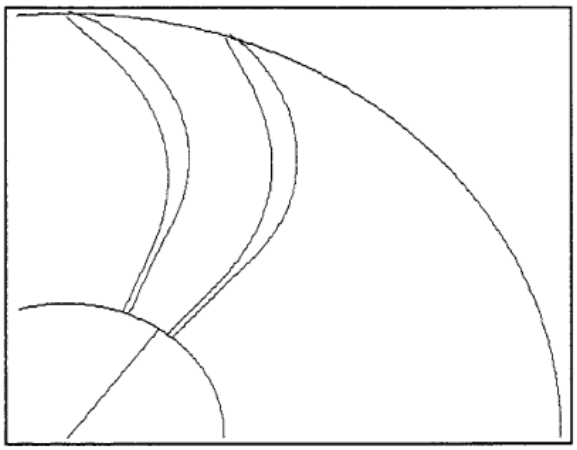

Figure 4.2: return channel vane shape [14]

Figure 4.1: return channel geometry and design parameters [13]

The adopted design procedure is a simplified version of the original one proposed by Aungier [14] to lower the number of geometrical inputs to be specified by the user in analogy with the methodology supposedly implemented in GasTurb [59].

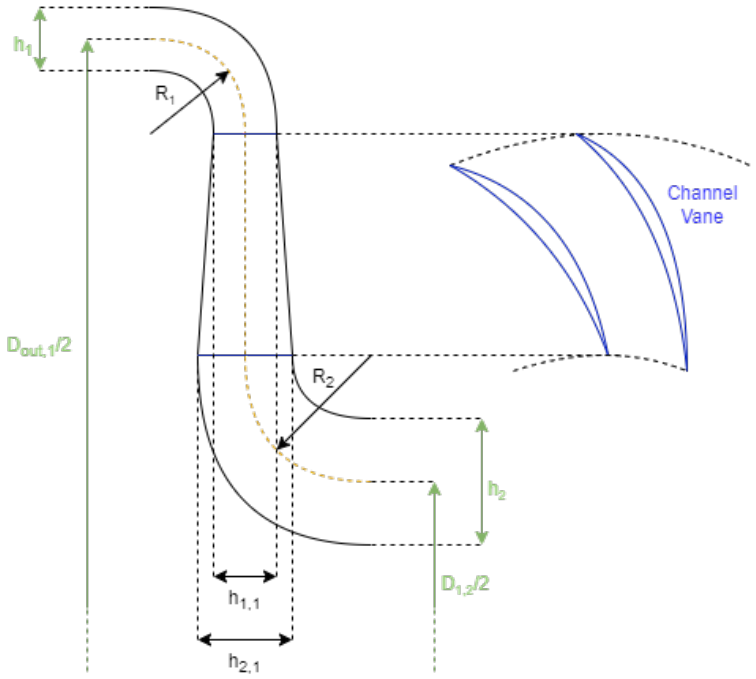

Figure 4.3: Return channel geometry

In particular, the use of the simplified geometry, shown in Figure 4.3, allows for the generation of the return channel given only the dimensions of the two connected stages and no additional input from the user.

The Inlet and outlet diameters and flow passage heights have to correspond to the outlet and inlet dimensions of the compressor stages. The simplified geometry generation procedure thus only requires four inputs to define the bends shape and three for the vanes as reported in Table 4.1.

Channel Parameter	Unit	Description
R_1	[m]	Inlet bend meanline radius
R_2	[m]	Outlet bend meanline radius
$h_{1,1}$	[m]	Vane inlet duct height
$h_{2,1}$	[m]	Vane outlet duct height
Vane Parameter	**Unit**	**Description**
β_{in}	[rad]	Vane inlet blade angle
β_{out}	[rad]	Vane outlet blade angle
N_{vane}	[-]	Number of return channel vanes

Table 4.1: Design variables of the return channel

These geometric quantities can all be calculated following the design guidelines by Aungier [13]. It results that no actual design input is required to the user. More in detail, we have:

$$R_1 = R_{bend,1} \tag{4.1}$$

$$\beta_{in} = \alpha_{3,1} \tag{4.2}$$

where $R_{bend,1}$,and $\alpha_{3,1}$ are the bend radius and the absolute flow angle at the outlet of the vaned section of the diffuser (see Figure 3.60) of the radial compressor upstream of the return channel, respectively. Similarly, it is assumed that:

$$\beta_{out} = \alpha_{1,2} \tag{4.3}$$

$$R_2 = h_2 \tag{4.4}$$

where $\alpha_{1,2}$ is the inlet absolute flow angle at the inlet of the radial compressor downstream of the return channel; the outlet bend radius is taken equal to the inlet flowpath height of the inlet channel of the radial compressor downstream of the return channel so that the condition of $R/h < 1$ specified by Aungier [13] for the outlet bend duct height is always met.

The duct heights can be calculated simply based on mass conservation given the velocity triangles at the inlet and outlet of the vaned section and the specified blade angles.

The blade profile of these vanes can then be generated through the same procedure used for the vaned diffuser blades discussed in section 3.1.9. Similarly, their performance may be evaluated using the same loss models implemented for the compressor diffuser.

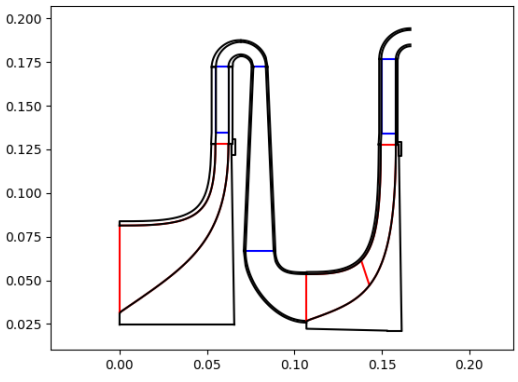

Figure 4.4: example return channel designed following this procedure

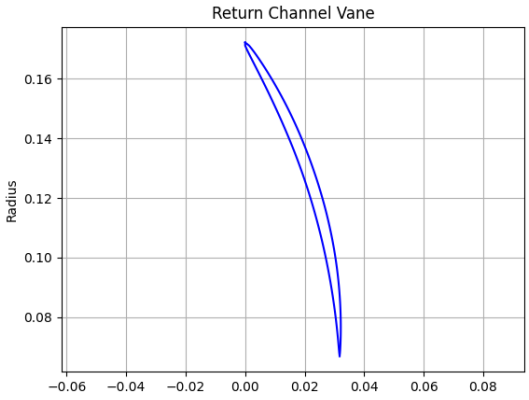

Figure 4.5: vane geometry of the return channel

The wall thickness of the channel duct is calculated using the same method used to determine the wall thickness of other engine ducts within WEST using the equation reported by Lolis [26].

4.2. REVERSE FLOW COMBUSTOR

In many applications of turboshaft engines the compactness of the gas generator is a very important design criterion. In order to reduce the engine length, the combustor often features a reverse flow configuration, as this allows the first stage of the high pressure turbine to be mounted much closer to the last compressor stage.

Though this type of configuration is very commonly found in turboshaft engines, no preliminary design method for reverse-flow combustors was found in literature. Most likely, this is due to the geometry and flow characteristics of this kind of combustor, which are more complex than those of a simple annular equivalent.

Grieb [6] reported the typical geometries of reverse flow and annular combustors when downstream of radial compressor stages in aero-engine applications, along with their key geometric parameters.

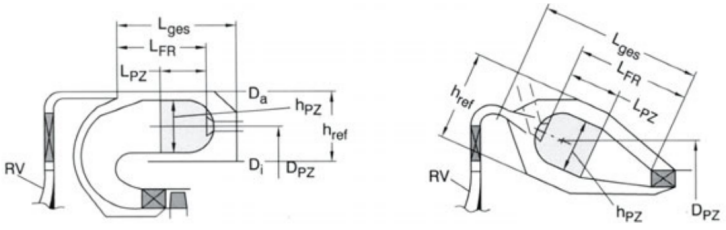

Figure 4.6: Combustor geometries from Grieb [6]

Khandelwal et.al. [15] provides an in-depth look into the detailed design procedure of a reverse flow combustor given its main dimensions , together with an illustration of the combustor developed by the authors.

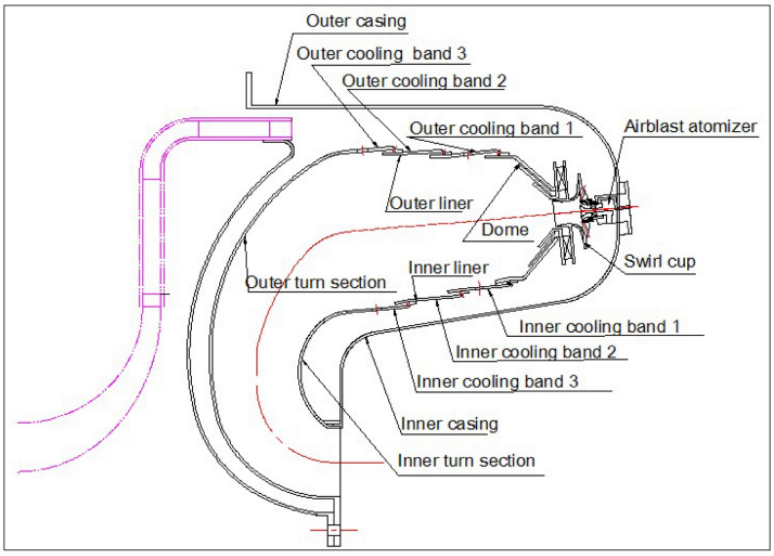

Figure 4.7: Schematic diagram of the developed combustor by Khandelwal et.al. [15]

Based on the information provided by these authors, a simplified geometry of the reverse flow combustor was conceived. As shown in Figure 4.8, this features four basic components: liner, casing, inlet de-swirler and dome-injector assembly

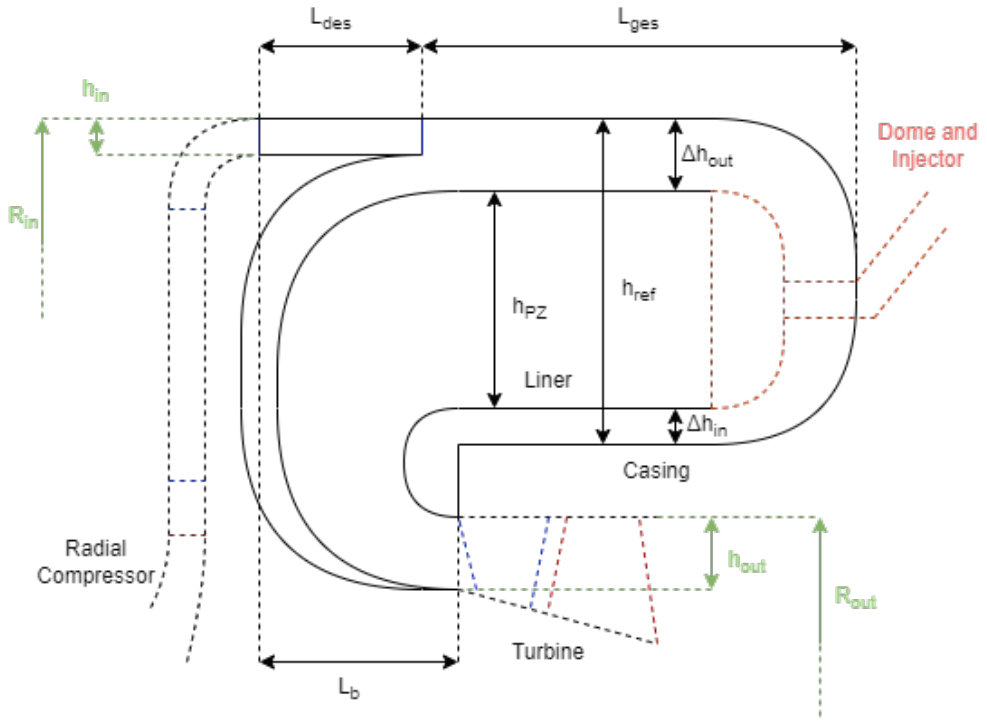

Figure 4.8: Reverse flow burner geometry

The dimensions of the reverse flow combustor are determined based on a combination of thermodynamic parameters and non-dimensional ratios. These inputs are listed in table 4.2.

Thermodynamic	Unit	Description
$\dot{m}_{air}$	[kg/s]	Air mass flow
$\dot{m}_{fuel}$	[kg/s]	Fuel mass flow
$p_{t,in}$	[Pa]	Inlet total pressure
$p_{t,out}$	[Pa]	Outlet total pressure
$T_{t,in}$	[K]	Inlet total temperature
$T_{t,out}$	[K]	Outlet total temperature
Geometric	**Unit**	**Description**
$H_{B,ratio}$	[-]	Combustor height ratio
$L_{ges,ratio}$	[-]	Combustor length-to-height ratio
$L_{b,ratio}$	[-]	Combustor axial-distance-to-height ratio

Table 4.2: Input parameters for reverse flow combustor design

The combustor height ratio relates the height of the combustor annular casing (h_{ref}) to the distance between radii (R_{in}, R_{out}) defining the position of the combustor inlet and outlet channels, as expressed in equation 4.5:

$$H_{B,ratio} = \frac{h_{ref}}{R_{in} - R_{out}} \tag{4.5}$$

The combustor length-to-height and the axial-distance-to-height ratios then define, respectively, the overall length of the combustor and the axial distance between the outlet of the radial compressor stage and the inlet of the axial turbine in relation to the combustor height. Their definition thus reads:

$$L_{ges,ratio} = \frac{L_{ges}}{h_{ref}} \tag{4.6}$$

$$L_{b,ratio} = \frac{L_b}{h_{ref}} \tag{4.7}$$

4.2.1. DE-SWIRLER

The de-swirler has the function of reducing the swirl velocity of the flow coming from the radial compressor stage. In principle, at the outlet of the de-swirler the flow should be only directed axially; it is designed following a similar strategy to the stator of an axial turbomachinery stage: the velocity triangle at the inlet is set by the design of the radial compressor stage, while at the outlet the flow velocity should have no radial component.

The wall thickness of the de-swirler duct are calculated using the same method used to size the other ducts within WEST [23, 26].

The length of the de-swirler duct is calculated based on the geometry of the rest of the combustor, making sure that the bent section of the casing leading into the axial turbine does not interfere with the radial compressor stage disk.

4.2.2. DOME AND INJECTORS

The design of the injector assembly is very complex, and no simplified preliminary design procedure was found in the literature for this subsystem. Thus, similarly to what done in WEST for annular combustors, the empirical correlation from Onat et al. [27] is used to estimate the weight of the dome and injector assembly. This correlation reads:

$$w_{dome,lbs} = 0.0106 \cdot (r^2_{t,inch} - r^2_{h,inch}) \tag{4.8}$$

4.2.3. CASING AND LINER

The thickness of the casing and liner of the reverse flow combustor is determined in a similar way as already done within WEST for annular combustors: the thickness of the casing is calculated based on the pressure containment requirement (section 3.4.2), whereas the liner thickness is taken equal to 1.5 mm as suggested by Onat et al. [27].

The weight of these components is simply obtained by calculating the volume , using the procedure shown in Appendix D and multiplying the result by the density of the material.

The height of the liner is calculated by applying an offset from the outer and inner portions of the casing, the offset is based on the observation of existing engine cross sections from available sources [15, 57, 6, 18] and is set as $\Delta h_{out} = 2 \cdot h_{in}$ for the outwards facing side and $\Delta h_{in} = h_{in}$ for the inward facing side.

This relation seems quite arbitrary, but was found to match very well data of existing combustors.

4.3. OTHER DESIGN FEATURES

Some small additions have been made to the already implemented modules in WEST to allow the program to perform properly the preliminary design of small-capacity turboshaft engines.

The following sections will briefly discuss these additions.

4.3.1. SHROUDED TURBINE

The turbine stage of a turboshaft engine is sometimes shrouded to improve its performance and efficiency. The shroud refers to a covering or casing around the turbine blades fixed to the blades themselves.

The shroud helps to reduce the flow leakage between the tips of the turbine blades and the surrounding casing. Furthermore the shroud provides additional structural support to the turbine blades. This is especially important in high-performance turboshaft engines that operate at high rotational speeds.

The shroud also dampens vibrations in the turbine blades, reducing the overall noise generated by the engine during operation; in some cases, the shroud may be used to provide additional thermal protection to the turbine blades.

The addition of the shroud at the tip of the blades, however, considerably increases the centrifugal force experienced by the blade roots, thus impacting heavily the centrifugal stress distribution in the disk.

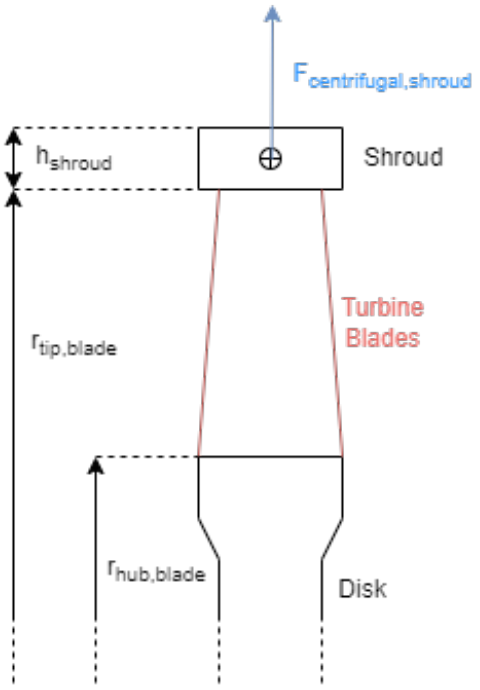

Figure 4.9: Centrifugal force acting on the turbine shroud

If the shroud thickness is known, the portion of radial stress at the rim of the disk caused by the presence of the shroud can be evaluated using equation 4.9, assuming that the stress is uniformly distributed at the rim of the disk.

$$\Delta\sigma_{rim,shroud} = \omega^2 \cdot h_{shroud} \cdot \rho_{mat} \cdot r_{cg,shroud} \cdot \frac{r_{tip,blade}}{r_{hub,blade}} \tag{4.9}$$

Alternatively, as no method was found to accurately estimate the optimal thickness of the shroud in a preliminary design stage, Grieb [6] provides some simple empirical correlations to directly determine the radial stress caused by the shroud:

$$\begin{cases} \Delta\sigma_{rim,shroud} = 0.25 \cdot \sigma_{rim,blade} & \text{for uncooled blades} \\ \Delta\sigma_{rim,shroud} = 0.50 \cdot \sigma_{rim,blade} & \text{for cooled blades} \end{cases} \tag{4.10}$$

The distinction between cooled and uncooled blades has to be specified as the presence of cooling channels in the blades reduces by a large margin the mass of the blades themselves, and thus the centrifugal stress they cause in the disk.

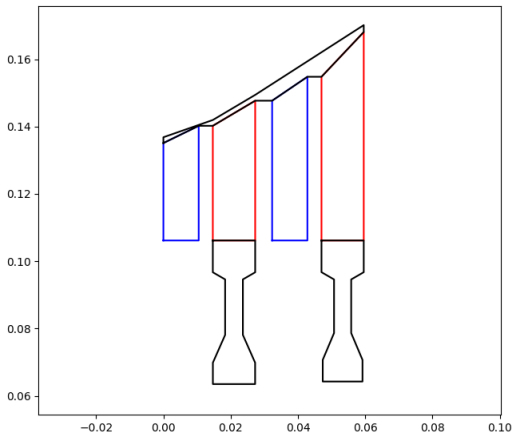

Figure 4.10: GE T700 free power turbine with shrouded blades

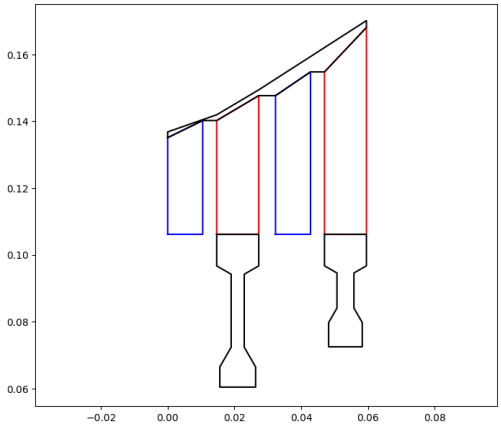

Figure 4.11: GE T700 free power turbine with unshrouded blades

Disk Type	Turbine Weight [kg]
Web Shrouded	7.52
Web Unshrouded	7.12

Table 4.3: Free power turbine weight comparison with and without shroud model

Implementing the shrouded turbine model does not appear to significantly impact the weight of this component, as shown by the test case illustrated in Figures 4.10 and 4.11 . However, the geometry change in the disks is significant, Notice that the weight of the actual shroud is not accounted in the turbine weight reported in Table 4.3. If this is included, the overall weight of the turbine will be higher.

4.3.2. BLISKS

Blisks, which stands for "bladed disks" or "integrally bladed rotors", combine both the rotor disk and blades into an integrated component realized from a single metal piece [53]. They may be preferred over regular blades in axial compressors for several reasons; they can provide improved aerodynamic performance compared to traditional blades, as by integrating the blades directly into the disk, gaps and interface between individual blades is reduced, thus minimizing air leakage and improving overall compressor efficiency.

The integration of the blade with the disk also eliminates the need for the hardware to attach the blade to the disk, leading to a reduction in weight and overall part count. This simplification can result in a more reliable and easier to maintain compressor; the absence of blade attachments eliminates the risk of blade loss due to blade-root fatigue, which is a concern with traditional blade designs.

This solution also impact the design of the rim of the disk, as the rim position to which the blades are attached can be much thinner. This particular kind of compressor disks has been modelled with the existing tools, adapting the existing webbed disk design code, by changing the estimated thickness of the blade root/rim portion of the disk from 75% of the blade height to 10%.

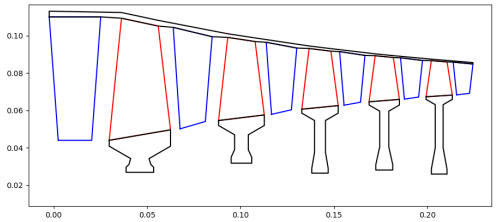

Figure 4.12: GE T700 axial compressor with blisks

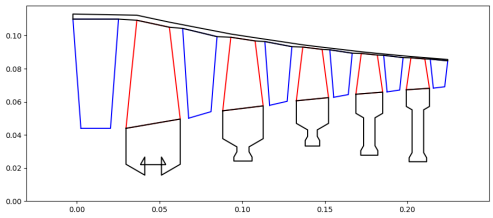

Figure 4.13: GE T700 axial compressor with regular webbed disks

Disk Type	Compressor Weight [kg]
Web with Blisks	9.79
Web without Blisks	11.87

Table 4.4: Compressor weight comparison with and without blisk model

This strategy was tested for the test case of the axial compressor of the GET700 engine. Figures 4.12 and 4.13 show the results of the compressor preliminary design in the case of blisk adoption and of conventional blades, respectively, while Table 4.4 reports the estimated weight. It is apparent that by adopting blisks the weight of the compressor does not change significantly, though the geometry of the engine is better predicted, especially in the case of the first stage disk.

4.3.3. TURBINE OUTLET FRAME

In small gas turbines, a turbine exit frame is typically essential to provide support for the turbine bearing, specifically for radial loads. The thrust loads, on the other hand, are handled by the front frame and front bearing, which may be integrated into the gearbox in certain cases [27].

As the empirical correlations from Onat and Klees [27] are already used to estimate the weight of all frames of the engine, it makes sense to use the model provided by the same authors in case of free power turbines of small capacity turboshafts.

Equation 4.11 is used to estimate the weight of the rear frame, which includes the tailpipe and nose cone:

$$W_{lbs,frame} = 55.5 \cdot R_{t,ft}^2 + 6.53 \tag{4.11}$$

Where $R_{t,ft}$ is the turbine tip radius in feet.

4.4. GEARBOX WEIGHT ESTIMATION

Turboshaft engines for either fixed-wing, tilt-rotor or rotorcraft applications often require that a reduction gearbox is fitted between the power turbine shaft and the power output shaft, which can be then connected directly to the propeller/rotor or other transmission components; the main function of this reduction gearbox is to reduce the output shaft rotational speed and increase the torque, allowing also the connection of additional gearing for auxiliary systems(oil pumps, alternators, fuel pumps, etc.).

This gearbox is sometimes an integral part of the engine package, such as in the MTR390 turboshaft engine [52, 57]. Thus, in these cases, it is necessary to estimate the weight of the reduction gearbox together with the rest of the engine.

The simplest method available to this purpose is provided by Onat and Klees [27] which correlates the gearbox weight with the shaft power and input RPM:

$$W_{lbs,gearbox} = 324 \cdot \left(\frac{hp}{RPM_{in}} \right)^{0.8} \tag{4.12}$$

Grieb [6], instead, proposes a correlation where the gearbox with respect to that of the engine block is expressed as a function of the speed reduction ratio, namely:

$$\frac{W_{gearbox}}{W_{engine}} = 0.02 + 0.047 \cdot \frac{RPM_{in}}{RPM_{out}} \tag{4.13}$$

Where RPM_{in} and RPM_{out} are the inlet and outlet rotational speeds of the gearbox expressed in number of revolutions per minute.

Brown et al. [16] and Hendricks and Tong [17] provide similar methods for the estimation of the gearbox of a turboshaft engine. The weight is a function of the gear reduction ratio and power output of the engine. Their correlations were fitted based on the data from a large number of existing engines, see Figures 4.14 and 4.15.

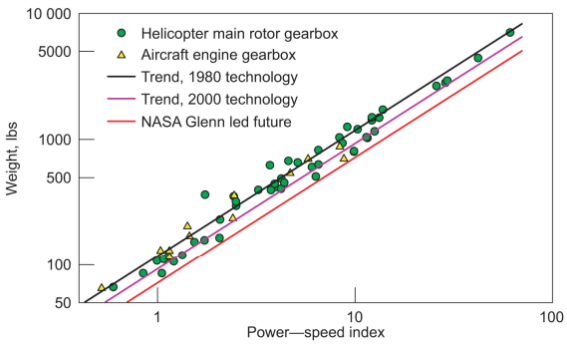

Figure 4.14: Correlation provided by Brown et al. [16]

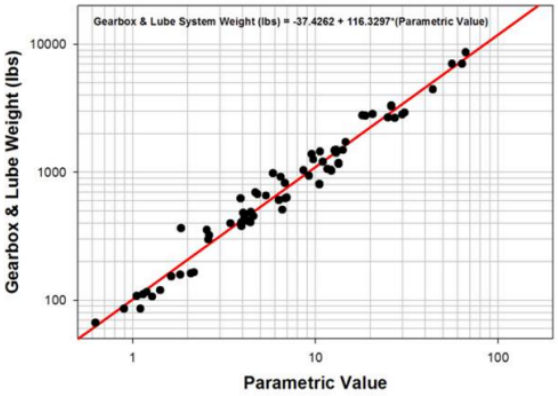

Figure 4.15: Correlation provided by Hendricks and Tong [17]

where the power-speed index and the Parametric value used by these two methods are calculated based on the gear reduction ratio and power output of the engine, namely:

$$\text{Parametric Value} = \left(\frac{hp}{RPM_{out}}\right)^{0.75} \cdot \left(\frac{RPM_{in}}{RPM_{out}}\right)^{0.15} \tag{4.14}$$

$$\text{Power-speed Index} = (hp)^{0.76} \cdot \left(\frac{RPM_{in}^{0.13}}{RPM_{out}^{0.89}}\right) \tag{4.15}$$

The correlations proposed by these authors are as follows, where hp is the power at the engine output shaft expressed in horsepower and K is a scaling factor based on the technology level, see Table 4.5.

$$W_{(lbs),Hendricks} = -37.4262 + 116.3297 \cdot \text{Parametric Value} \tag{4.16}$$

$$W_{(lbs),Brown} = \text{Power-speed Index} \cdot K \tag{4.17}$$

K value	Level
118	year 1980
94	year 2000
72	future [1]

Table 4.5: Technology level scaling factor

4.5. WEIGHT ESTIMATION VALIDATION

Detailed data about the breakdown of component weights and detailed dimensions of small and medium turboshaft engines is not available in the literature. For this reason , the turboshaft engines chosen as test case are those for which detailed cross-sections [18, 57, 52]were found. The validation exercise consist in matching as closely as possible the estimated geometry of these engines, and comparing the overall engine weights.

In the following sections the design of two turboshaft engines with similar operating characteristics but very different architectures will be presented. These are the MTU Turbomeca Rolls-Royce MTR390 and the General Electric T700; the inputs and results for both these engines will be discussed in detail.

Appendix E contains an extended set of plots for the design results of the radial compressor stages of both engines.

4.5.1. MTU TURBOMECA ROLLS-ROYCE MTR390

The MTR390 is a modern turboshaft engine in the 1000 kW power range, developed collaboratively by three prominent European aero engine companies: MTU, TURBOMECA, and ROLLS-ROYCE.

The compressor assembly features two centrifugal stages, see Figure 4.16, whose design has been refined since 1982. Initially, the OEM considered an axial-centrifugal configuration, but the present design shows notable performance benefits in terms of efficiency (increased by 2%), flow, and pressure ratio. These advantages were achieved by employing a circumferential speed that is lower than that of the centrifugal compressor in the original axial-centrifugal version [52].

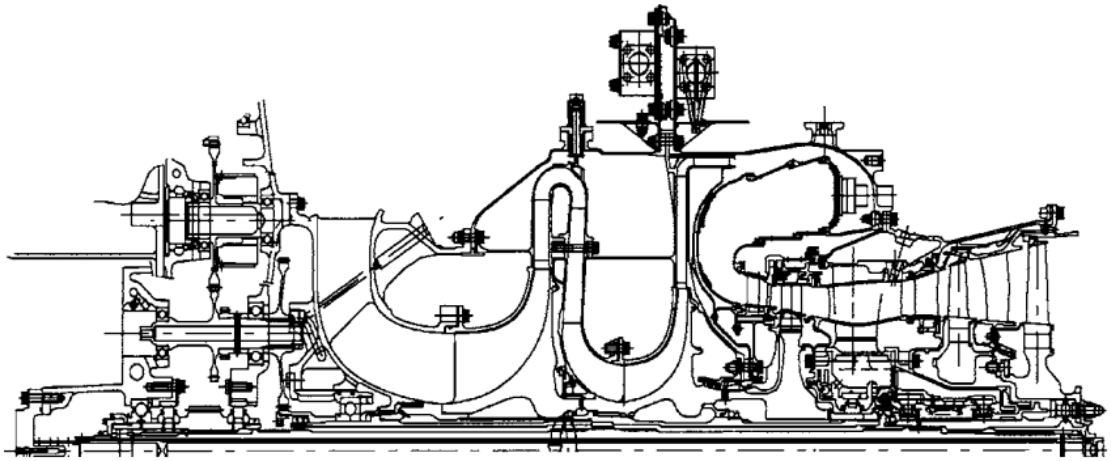

Figure 4.16: Cross-section of the MTR390 engine from Grieb [18]

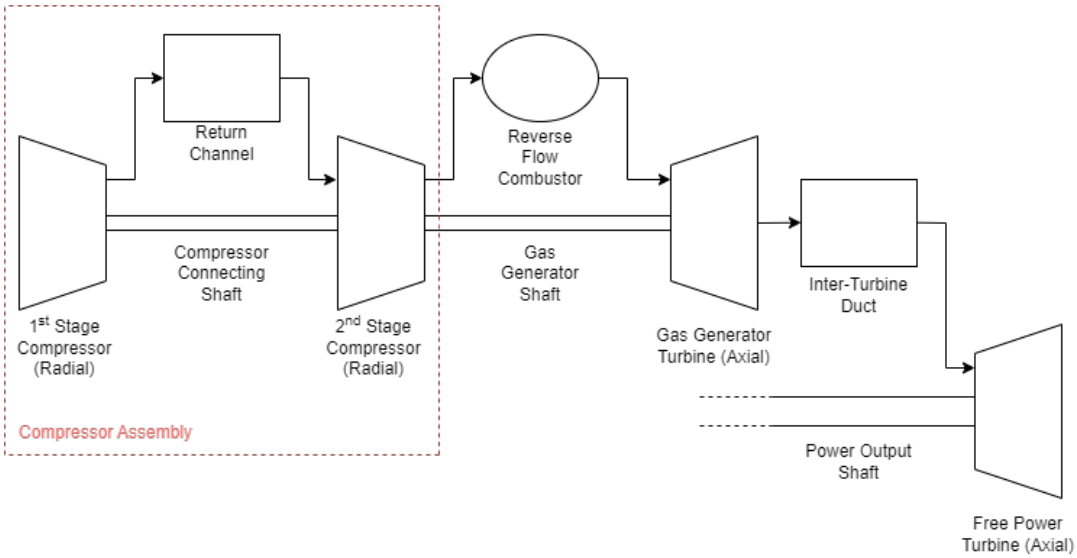

Figure 4.17: Overview of the components of the MTR390 model realized with WEST

The compressor overall pressure ratio is 13. The engine features also a compact reverse-flow combustor, a single stage high pressure cooled axial turbine to power the gas generator and a single row uncooled free power turbine stage that sends power into an integrated step down gearbox, which reduces the output shaft speed from 27000 RPM to 8000 RPM. A schematic of the layout of the engine components is shown in Figure 4.17.

The model inputs are reported in Table 4.6, Table 4.8 and Table 4.7

COMPRESSORS

		First Stage Compressor	Second Stage Compressor
Duty Coefficient	**Unit**	**Value**	**Value**
Flow coefficient,ϕ	[-]	0.28	0.25
Work coefficient, ψ	[-]	0.5	0.5
Degree of reaction, R	[-]	0.7	0.55
Thermodynamic	**Unit**	**Value**	**Value**
$\dot{m}$	[kg/s]	3.2	3.2
Ω	[RPM]	39000	39000
$T_{t,in}$	[K]	300	450
$P_{t,in}$	[bar]	1	3.6
β_{tt}	[-]	3.6	3.6
η_{tt}	[-]	0.87	0.87
General Design	**Unit**	**Value**	**Value**
Shape Factor	[-]	0.85	0.75
Splitter Blades	[-]	True	True
Splitter Length	[-]	0.5	0.5
Geometry	**Unit**	**Value**	**Value**
Disk Type	[-]	'A'	'A'
$r_{sh,max}$	[m]	0.02	0.02
D_3/D_2	[-]	-[a]	1.65[b]
Material	**Unit**	**Value**	**Value**
Diffuser Vane	[-]	Ti-17	Ti-17
Disk/Blade Material	[-]	Ti-17	Ti-17
Casing Material	[-]	17-4PH	17-4PH

[a] computed
[b] specified to better match the existing geometry

Table 4.6: Input parameters for MTR390-2C radial compressor stages

COMBUSTOR

Thermodynamic	**Unit**	**Value**
$\dot{m}_{air}$	[kg/s]	3.2
$\dot{m}_{fuel}$	[kg/s]	0.079
$p_{t,in}$	[bar]	13
$p_{t,out}$	[bar]	12.4
$T_{t,in}$	[K]	670
$T_{t,out}$	[K]	1450
Geometric	**Unit**	**Value**
$H_{B,ratio}$	[-]	0.75
$L_{ges,ratio}$	[-]	1.1
$L_{b,ratio}$	[-]	0.65

Table 4.7: Input parameters for MTR390-2C reverse flow combustor

TURBINES

		Gas Generator Turbine	Free Power Turbine
Duty Coefficient	**Unit**	**Value**	**Value**
Flow coefficient,ϕ	[-]	0.41	0.4
Work coefficient, ψ	[-]	1.7	1.4
Degree of reaction, R	[-]	0.48	0.5
Thermodynamic	**Unit**	**Value**	**Value**
$\dot{m}$	[kg/s]	3.279	3.279
$\dot{W}$	[kW]	1200	970
Ω	[RPM]	39000	27000
$T_{t,in}$	[K]	1450	1100
$P_{t,in}$	[bar]	12.4	4.65
$T_{cooling}$	[K]	450	-
η_{tt}	[-]	0.91	0.91
General Design	**Unit**	**Value**	**Value**
Stage Count	[-]	1	2
Fixed Diameter	[-]	Tip	Hub
Zweifel Coefficient, Ψ_Z	[-]	0.8	0.8
Cooled Blades	[-]	True	False
Geometry	**Unit**	**Value**	**Value**
Row Gap	[-]	0.567	0.567
Stage Gap	[-]	0.567	0.567
Rotor Taper Ratio	[-]	1	1
First Stage Rotor Aspect Ratio	[-]	1	2
Last Stage Rotor Aspect Ratio	[-]	-	2.7
Stator Taper Ratio	[-]	1	1
First Stage Stator Aspect Ratio	[-]	1	1.7
Last Stage Stator Aspect Ratio	[-]	-	2
Disk Type	[-]	Web	Web
$r_{sh,max}$	[m]	0.02	0.04
Material	**Unit**	**Value**	**Value**
Stator Vane	[-]	NI 105	NI 105
Rotor Blade	[-]	IN 718	IN 718
Disk Material	[-]	IN 718	IN 718
Casing Material	[-]	NI 105	17-4PH

Table 4.8: Input parameters for MTR390-2C axial turbine stages

Component [-]	Weight [kg]
First stage compressor	7.01
casing	2.31
disk + blades	4.59
stator vanes	0.11
inter-compressor connecting shaft	0.11
First stage inlet frame	3.76
Return channel	2.55
vanes	0.55
Second stage compressor	4.35
casing	2.06
disk + blades	2.1
stator vanes	0.19
Combustor	37.51
de-swirler vanes	0.10
de-swirler duct	0.79
casing + liner	6.68
frame	29.74
Gas generator turbine	4.64
Inter-turbine frame	8.87
Turbine connecting duct	0.86
Free power turbine	12.57
Free power turbine frame	9.35
Gas generator shaft	0.26
Power output shaft	0.87
Accessories	15.33
Total weight	105.48
Gearbox	
Brown [16]	15.76
Hendricks [17]	-0.76
Grieb [6]	18.84
Onat [27]	12.99

Table 4.9: Design results of the MTR390-2C turboshaft engine

The results of the preliminary design are reported in Table 4.9. The total weight estimated by the program is of 105.48 kg excluding the gearbox, which falls short of the published weight of the engine [60], which is 169 kg; it has to be considered, however, that the published weight of the engine does not only include the weight of the gas generator and free power turbine assembly, but the oil filtration and management system and the integrated reduction gearbox, that contains additional gearing for powering other components such as oil pumps. These components are not included in any of the models discussed for the gearbox weight estimation. Moreover, no model to estimate the weight of the outer casing as well as the inlet dict leading into the first compressor stage has been implemented.

The various models used for the gearbox weight estimation give very different results, especially the correlation developed by Hendricks et al. [17] which is evidently not suited for this kind of gearbox, as the estimate weight is negative.

Depending on the choice of the model for the gearbox weight the results provide an estimation that is between 70.1% and 73.5% of the published weight, which falls well within the expectations for the accuracy of the WEST program.

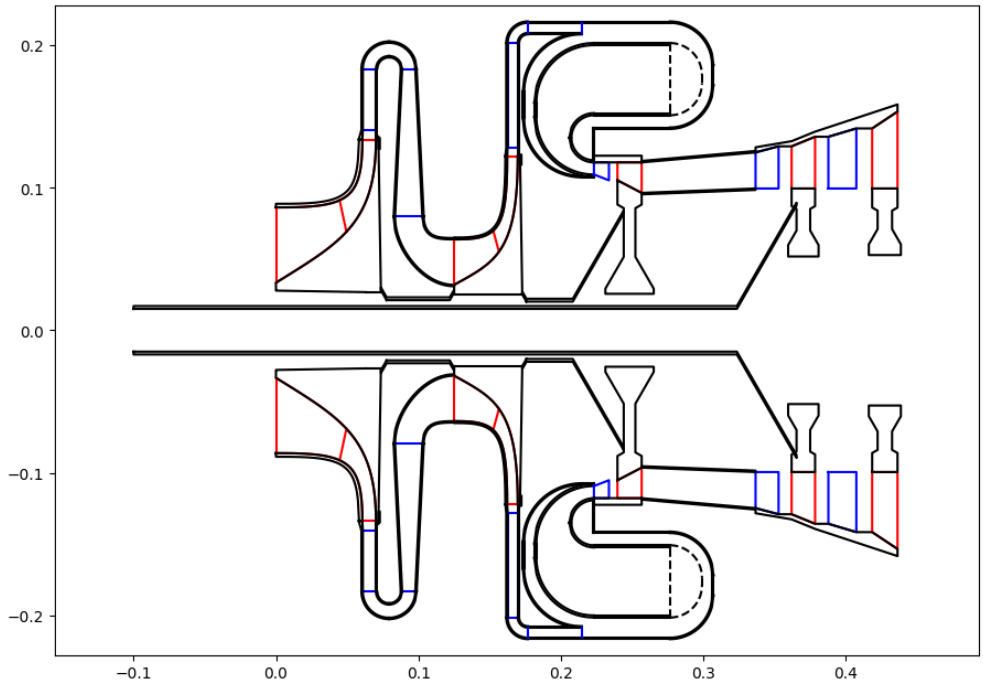

Figure 4.18: Mechanical design results of the MTR390-2C turboshaft engine

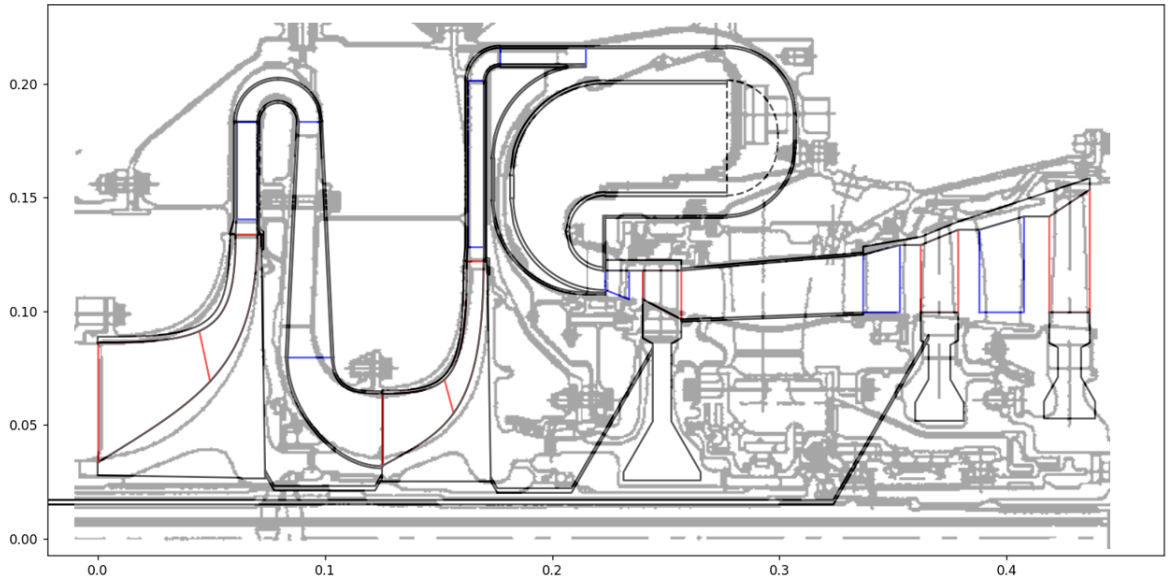

Figure 4.19: Overlay of MTR390-2C actual and WEST cross-sections [18]

The overlap between the engine cross-section and the generated geometry is rather good, see Figures 4.18 and 4.19; some differences are in the shape of the radial compressor stages, as the flow path shape of the first stage is predicted as slightly narrower than its real counterpart; furthermore the cuts at the hub of both impeller disks are not present as it is not possible to model this kind of feature with the developed tools.

The return channel between the two stages does not completely match, as expected due to the adopted simplified geometry model.

On the contrary, the geometry of the reverse flow combustor matches very closely with the real engine.

4.5.2. GENERAL ELECTRIC T700

The General Electric T700 and CT7 are a family of turboshaft and turboprop engines in the 1,100–2,200 kW class.

Data for the operating conditions and cycle parameters for the T700 is not fully available in literature. However it was possible to retrieve most of the main engine parameters from Ballin [61] and the General Electric brochure for the T700-401C/-701C models [62].

It was also possible to retrieve the materials for the axial and radial compressor disks from the technical report by Hunter and Grimmer [53].

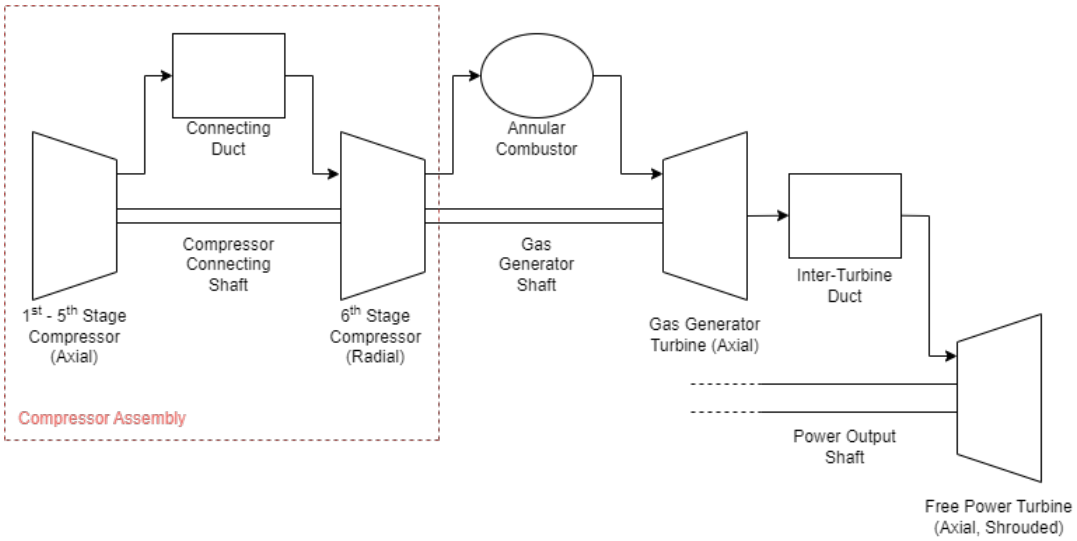

Figure 4.20: Overview of the components of the T700 model realized with WEST

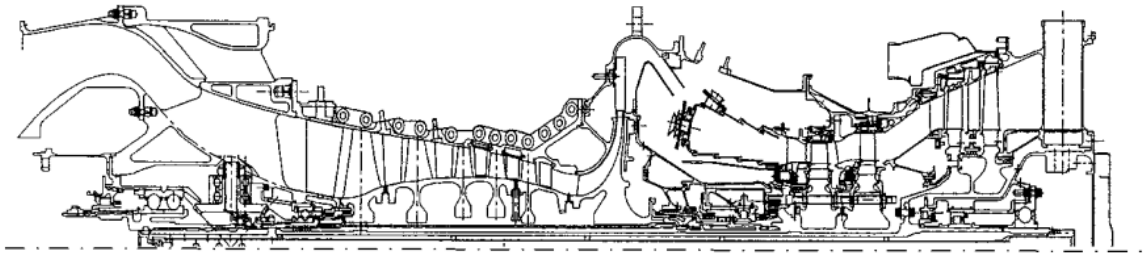

Figure 4.21: Cross-section of the T700 engine from Grieb [18]

The T700-GE-700 (the initial version from which the whole familiy started) is a free-turbine turboshaft engine without an integrated gearbox. It comprises a five-stage axial and one-stage centrifugal mixed-flow compressor characterized by the use of single piece blisk axial stages.

The engine has an annular combustion chamber with central fuel injection to enhance combustion and minimize smoke emissions. It also incorporates a two-stage gas generator turbine and a two-stage free power turbine with tip-shrouded blades.A simplified prcoess flow diagram of the engine is provided in Figure 4.20 , while its cross section in Figure 4.21.

The design incorporates also an inlet particle separator to remove dirt, sand, and dust.

The inputs of this model are reported in Table 4.10, Table 4.13 , Table 4.13 and Table 4.12 All inputs were tuned to obtain the closest possible match between the flow path of the modelled engine and the one represented in the cross section.

COMPRESSORS

Duty Coefficient	Unit	Value
Flow coefficient,ϕ	[-]	0.4
Work coefficient, ψ	[-]	0.4
Degree of reaction, R	[-]	0.5
Thermodynamic	**Unit**	**Value**
$\dot{m}$	[kg/s]	4.57
$\dot{W}$	[MW]	1.188
Ω	[RPM]	44740
$T_{t,in}$	[K]	300
$P_{t,in}$	[bar]	1
β_{tt}	[-]	6.5
η_{tt}	[-]	0.91
General Design	**Unit**	**Value**
Stage Count	[-]	5
Fixed Diameter	[-]	Mid
Guide Vane	[-]	True
Geometry	**Unit**	**Value**
Row Gap	[-]	0.25
Stage Gap	[-]	0.45
Rotor Taper Ratio	[-]	0.6
First Stage Rotor Aspect Ratio	[-]	2.3
Last Stage Rotor Aspect Ratio	[-]	1.65
Stator Taper Ratio	[-]	0.65
First Stage Stator Aspect Ratio	[-]	2.9
Last Stage Stator Aspect Ratio	[-]	1.9
Disk Type	[-]	Web (Blisk)
$r_{sh,max}$	[m]	0.02
Material	**Unit**	**Value**
Stator Vane	[-]	17-4PH
Rotor Blade	[-]	17-4PH
Disk Material	[-]	17-4PH
Casing Material	[-]	17-4PH

Table 4.10: Input parameters for the axial compressor of the T700 engine

Duty Coefficient	Unit	Value
Flow coefficient,ϕ	[-]	0.28
Work coefficient, ψ	[-]	0.5
Degree of reaction, R	[-]	0.7
Thermodynamic	**Unit**	**Value**
$\dot{m}$	[kg/s]	4.57
Ω	[RPM]	44740
$T_{t,in}$	[K]	560
$P_{t,in}$	[bar]	6.5
β_{tt}	[-]	2.7
η_{tt}	[-]	0.91
General Design	**Unit**	**Value**
Shape Factor	[-]	0.45
Splitter Blades	[-]	True
Splitter Length	[-]	0.5
Geometry	**Unit**	**Value**
Disk Type	[-]	'B'
$r_{sh,max}$	[m]	0.02
r_{max}	[m]	0.191[a]
Material	**Unit**	**Value**
Diffuser Vane	[-]	IN 718
Disk/Blade Material	[-]	IN 718
Casing Material	[-]	17-4PH

[a] specified to better match the existing geometry

Table 4.11: Input parameters for T700 radial compressor stage

COMBUSTOR

Thermodynamic	Unit	Value
$\dot{m}_{air}$	[kg/s]	4.57
$\dot{m}_{fuel}$	[kg/s]	0.13
$p_{t,in}$	[bar]	17.5
$p_{t,out}$	[bar]	16.7
$T_{t,in}$	[K]	750
$T_{t,out}$	[K]	1400
V_m	[m/s]	27

Table 4.12: Input parameters for T700 annular combustor

TURBINES

		Gas Generator Turbine	Free Power Turbine
Duty Coefficient	**Unit**	**Value**	**Value**
Flow coefficient,ϕ	[-]	0.41	0.4
Work coefficient, ψ	[-]	1.7	1.4
Degree of reaction, R	[-]	0.48	0.5
Thermodynamic	**Unit**	**Value**	**Value**
$\dot{m}$	[kg/s]	4.7	4.7
$\dot{W}$	[MW]	2.0	1.3
Ω	[RPM]	44740	22000
$T_{t,in}$	[K]	1400	1020
$P_{t,in}$	[bar]	16.7	4.65
$T_{cooling}$	[K]	500	-
η_{tt}	[-]	0.91	0.91
General Design	**Unit**	**Value**	**Value**
Stage Count	[-]	2	2
Fixed Diameter	[-]	Hub	Hub
Zweifel Coefficient, Ψ_Z	[-]	0.7	0.7
Cooled Blades	[-]	True	False
Geometry	**Unit**	**Value**	**Value**
Row Gap	[-]	0.567	0.4
Stage Gap	[-]	0.567	0.4
Rotor Taper Ratio	[-]	1	1
First Stage Rotor Aspect Ratio	[-]	1	3
Last Stage Rotor Aspect Ratio	[-]	1.6	4.4
Stator Taper Ratio	[-]	1	1
First Stage Stator Aspect Ratio	[-]	1	3
Last Stage Stator Aspect Ratio	[-]	1.2	4.3
Disk Type	[-]	Web	Web (Shrouded)
$r_{sh,max}$	[m]	0.02	0.04
Material	**Unit**	**Value**	**Value**
Stator Vane	[-]	NI 105	NI 105
Rotor Blade	[-]	IN 718	NI 105
Disk Material	[-]	IN 718	NI 105
Casing Material	[-]	NI 105	NI 105

Table 4.13: Input parameters for T700 axial turbine stages

Component [-]	Weight [kg]
Axial compressor	9.79
inter-compressor connecting shaft	0.15
inter-compressor connecting duct	0.16
First stage inlet frame	6.10
Radial compressor	5.08
casing	1.72
disk + blades	3.30
stator vanes	0.06
Combustor	27.55
frame	23.30
Gas generator turbine	6.58
Inter-turbine frame	11.91
Turbine connecting duct	0.54
Free power turbine	7.52
Free power turbine frame	17.93
Gas generator shaft	0.38
Power output shaft	1.41
Accessories	16.17
Total weight	111.30

Table 4.14: Design results of the GE T700 turboshaft engine

The results of the preliminary design are reported in Table 4.14.The total weight of the modelled engine (111.30 kg) is greatly underestimated compared to the published data of 207kg [62]. This can be partly explained with the fact that not all design features and components of the engine are modelled. For example the inlet particle separator, which according to Grieb [6] accounts for as much as 16% of the gas generator weight, is not accounted in the weight estimation.

The outer casing and other potential additional components that contribute to the total dry weight of the engine (de-icing systems, variable inlet guide vanes) are also not modelled.

If the mass of the particle separator, estimated based on the rule of thumb reported by Grieb, is subtracted from the published weight, the underestimation by the program is of about −37% which is still within the −40%/+10% accuracy expectation of the WEST tool. Notice, however, that the good geometry match between the model and the cross section of the real engine (see Figures 4.22 and 4.23) suggests that if the non-modelled additional components were accounted for, the accuracy in the weight would estimation be much higher.

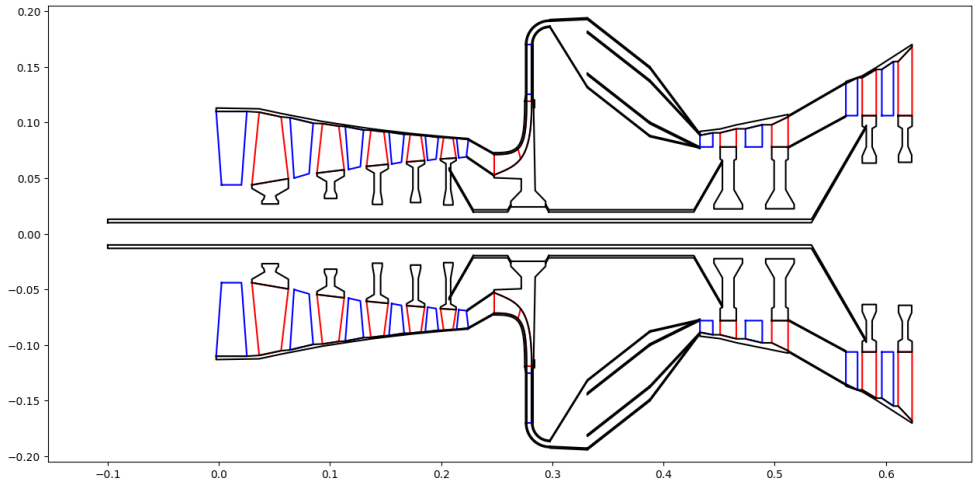

Figure 4.22: Mechanical design results of the GE-T700 turboshaft engine

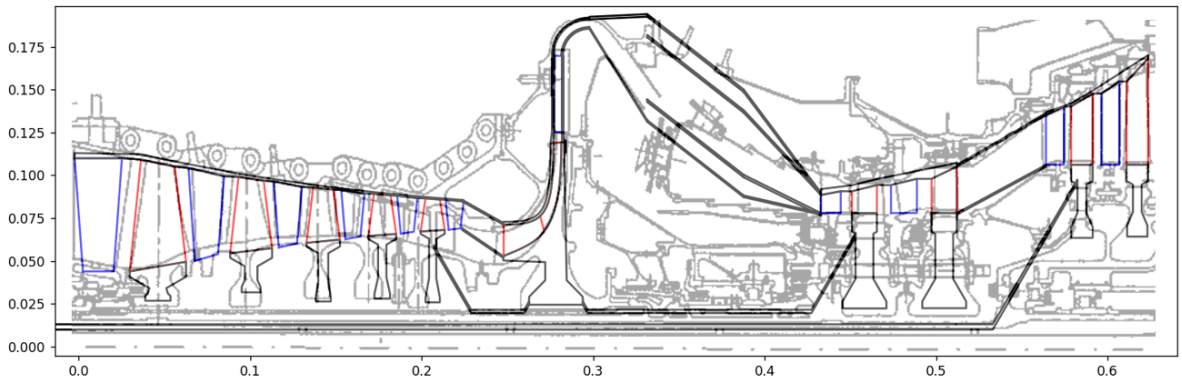

Figure 4.23: Overlay of GE-T700 actual and WEST cross-sections [18]

The match between the generated engine cross-section (Figure 4.23) and its real counterpart is very good. In the flow path the largest mismatch is observed close to the transition between the axial and radial compressor stages, as the axial compressor design methodology allows only for mid, hub or tip fixed diameters. So the more complex shape of this engine cannot be fully captured.

The annular combustor was designed using the annular combustor model available in WEST. It is apparent, however, that this model does not accurately match the real geometry. This should not impact significantly the weight estimation as most of the combustor weight is represented by the frame, whose weight only scales with the outside radius that is prescribed in the analysis.

A small mismatch is found also in the geometry of the free power turbine disks and casing most likely due to the fact that the free power turbine of this engine is built with tip shrouded blades. Even if a model was introduced to account for the shroud's centrifugal stress contribution, the shroud and the related casing weight is still not accounted.

Even though the weight is underestimated by a large margin, the matching of the geometry is still very good, and with the addition of models for the excluded components the results should greatly improve.

4.6. SENSITIVITY ANALYSIS

Using the MTR390 turboshaft engine model developed in section 4.5.1 a series of analyses was conducted to observe the behaviour of the model as key design parameters of the engine are changed.

Three sets of results are obtained varying the mass flow rate by ±25% (section 4.6.1), the overall pressure ratio by ±15% (section 4.6.2) and the turbine inlet temperature by ±7% (section 4.6.3).

4.6.1. MASS FLOW RATE

The sensitivity of the engine weight to the variation in mass flow rate was evaluated by varying the design mass flow rate of the engine by a factor of ±25%.

The inputs of the design are the same as shown in section 4.5.1 except for the mass flow rate, and the power output of the turbines.

The power output of the turbines has to be scaled for both the gas generator and the free power turbine. The gas generator turbine needs to provide the necessary power for the compressor stages, as more power is needed for the same pressure ratio if the mass flow rate is increased and less power if it is decreased. Assuming that the pressures and temperature are to be kept the same across the free power turbine as the original engine design, the power output of this component changes with the mass flow rate. The power outputs of the turbine stages are reported in Table 4.15.

	$0.75 \cdot \dot{m}_{nominal}$	$\dot{m}_{nominal}$	$1.25 \cdot \dot{m}_{nominal}$
Component [-]	**Power** [kW]	**Power** [kW]	**Power** [kW]
HPT	900	1200	1500
FPT	727.5	970	1212.5

Table 4.15: Adjusted turbine powers for mass flow scaling for the MTR390 engine model

Figures 4.24 and 4.25 show the estimated geometries of the two analysed engines, while the other results are reported in Tables 4.16 and 4.17.

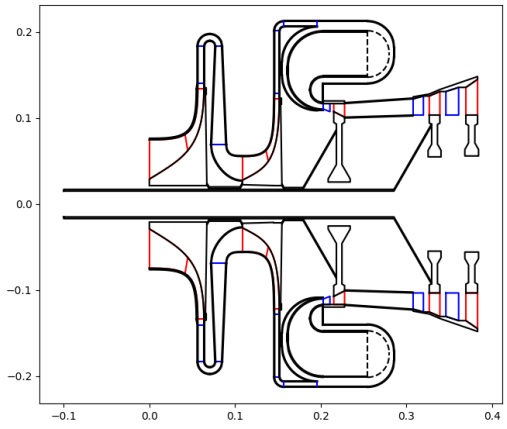

Figure 4.24: Mechanical design results of the MTR390-2C turboshaft engine with $\dot{m} = 0.75 \cdot \dot{m}_{nominal}$

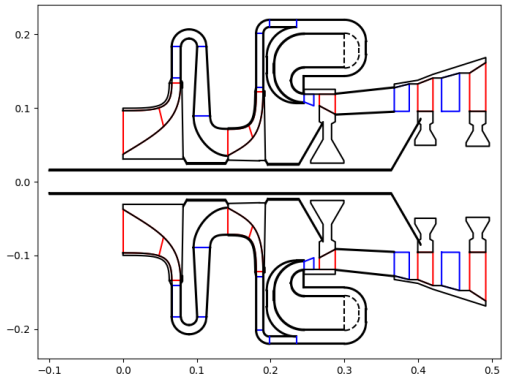

Figure 4.25: Mechanical design results of the MTR390-2C turboshaft enginewith $\dot{m} = 1.25 \cdot \dot{m}_{nominal}$

	$0.75 \cdot \dot{m}_{nominal}$	$\dot{m}_{nominal}$	$1.25 \cdot \dot{m}_{nominal}$
Component [-]	**Weight** [kg]	**Weight** [kg]	**Weight** [kg]
First stage compressor	5.57	7.01	8.96
casing	1.87	2.31	2.81
disk + blades	3.64	4.59	5.97
stator vanes	0.06	0.11	0.18
inter-compressor connecting shaft	0.08	0.11	0.15
First stage inlet frame	2.81	3.76	4.70
Return channel	2.31	2.55	2.70
vanes	0.55	0.55	0.61
Second stage compressor	3.75	4.35	5.01
casing	1.85	2.06	2.27
disk + blades	1.77	2.1	2.49
stator vanes	0.13	0.19	0.29
Combustor	36.25	37.51	38.71
de-swirler vanes	0.08	0.10	0.12
de-swirler duct	0.80	0.79	0.77
casing + liner	6.45	6.68	6.89
frame	28.73	29.74	30.73
Gas generator turbine	3.12	4.64	6.86
Inter-turbine frame	8.71	8.87	9.03
Turbine connecting duct	0.87	0.86	0.85
Free power turbine	7.95	12.57	18.27
Free power turbine frame	8.65	9.35	10.05
Gas generator shaft	0.24	0.26	0.27
Power output shaft	0.84	0.87	0.92
Accessories	13.40	15.33	17.65
Total weight	92.25	105.48	121.45

Table 4.16: Design results of the MTR390-2C turboshaft engine

	$0.75 \cdot \dot{m}_{nominal}$	$1.25 \cdot \dot{m}_{nominal}$
Assembly [-]	**ΔWeight** [%]	**ΔWeight** [%]
First stage compressor	-20.5	+27.8
Return channel	-9.4	+5.9
Second stage compressor	-13.8	+15.2
Combustor	-3.3	+3.2
Gas generator turbine	-32.8	+47.8
Turbine connecting duct	+1.1	-1.2
Free power turbine	-12.57	+45.3
Frames	-5.6	+5.4
Total	-12.5	+15.1

Table 4.17: Weight variation of each assembly as a result of the mass flow rate scaling

Increasing the mass flow rate through the engine results in an increase of the overall weight of every component of the engine. Thus, the whole engine design is scaled up.

The weight of the engine is increased by 15.1% for an increase in mass flow rate of 25% as the outer diameter of the components is not changed by a large amount, leading to a smaller change in the combined weight of the frames, which covers about half of the total estimated weight. A similar trend is observed for the reduction in mass flow rate of -25%, which yields a reduction in total engine weight of -12.5% while the frames weight is only reduced by -5.6%.

The components more affected by the change in mass flow rate and power requirement are the two turbine

spools, that increase in weight by more than 40% when the mass flow rate is increased. This can be attributed to the increase in power output, which leads to bigger blades and thus much "thicker" disks; a similar but opposite trend is observed when the mass flow rate is reduced.

4.6.2. OVERALL PRESSURE RATIO

The sensitivity of the engine weight to the variation in overall pressure ratio was evaluated by varying the design pressure ratio of the engine ($OPR = 13$) by ±2.

The inputs of the model are the same of Section 4.5.1 except for OPR, and the power output of the turbines.

The power output of the turbines has to be scaled for both the gas generator and the free power turbine. The gas generator turbine needs to provide the necessary power for the compressor stages, as more power is needed if the design pressure ratio is increased and the mass flow rate is kept the same. Assuming that the exhaust pressure and temperature of the engine are the same as in the original engine design, the power output of this component slightly changes for different compressor pressure ratios. The power outputs of the turbine stages are reported in Table 4.18.

	$OPR = 11$	$OPR = 13$	$OPR = 15$
Component [-]	**Power [kW]**	**Power [kW]**	**Power [kW]**
HPT	1090	1200	1300
FPT	956.2	970	973.1

Table 4.18: Adjusted turbine powers for overall pressure ratio for the MTR390 engine model

Note that the powers of the free power turbine shown in table 4.18 are very similar, so the alternative engines may also be confronted as if they had the same power output, as the mass flow rate adjustment (described in Section 4.6.1) required to reach the same power output would be of less than 2%.

Figures 4.26 and 4.27 show the estimated engine geometries of the two analysed engines, while the overall results are reported in Tables 4.19 and 4.20.

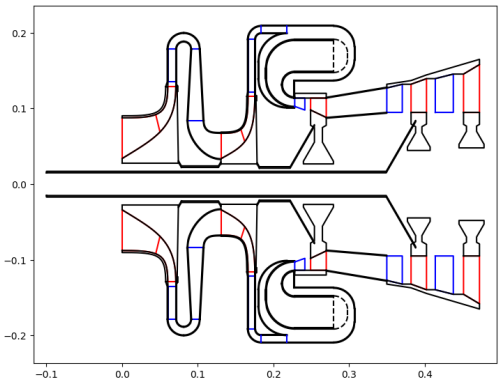

Figure 4.26: Mechanical design results of the MTR390-2C turboshaft engine with $OPR = 11$

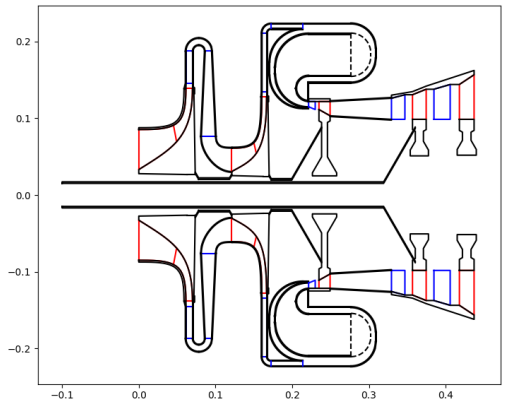

Figure 4.27: Mechanical design results of the MTR390-2C turboshaft enginewith $OPR = 15$

	$OPR = 11$	$OPR = 13$	$OPR = 15$
Component [-]	**Weight [kg]**	**Weight [kg]**	**Weight [kg]**
First stage compressor	7.08	7.01	7.01
casing	2.32	2.31	2.31
disk + blades	4.61	4.59	4.61
stator vanes	0.13	0.11	0.09
inter-compressor connecting shaft	0.13	0.11	0.10
First stage inlet frame	3.88	3.76	3.66
Return channel	2.51	2.55	2.55
vanes	0.56	0.55	0.51
Second stage compressor	4.38	4.35	4.39
casing	2.00	2.06	2.13
disk + blades	2.12	2.1	2.11
stator vanes	0.26	0.19	0.14
Combustor	34.96	37.51	41.11
de-swirler vanes	0.10	0.10	0.09
de-swirler duct	0.68	0.79	1.11
casing + liner	6.20	6.68	8.04
frame	27.79	29.74	31.67
Gas generator turbine	5.90	4.64	4.09
Inter-turbine frame	8.26	8.87	9.45
Turbine connecting duct	0.83	0.86	0.88
Free power turbine	17.58	12.57	14.39
Free power turbine frame	9.72	9.35	9.60
Gas generator shaft	0.25	0.26	0.26
Power output shaft	0.89	0.87	0.87
Accessories	15.96	15.33	16.29
Total weight	109.83	105.48	112.08

Table 4.19: Design results of the MTR390-2C turboshaft engine

	$OPR = 11$	$OPR = 15$
Assembly [-]	**ΔWeight [%]**	**ΔWeight [%]**
First stage compressor	+1.0	+0.0
Return channel	-1.6	+0.0
Second stage compressor	+0.7	+0.9
Combustor	-6.8	+9.6
Gas generator turbine	+27.7	-11.9
Turbine connecting duct	-3.5	+2.3
Free power turbine	+39.9	+14.5
Frames	-4.0	+5.1
Total	+4.1	+6.3

Table 4.20: Weight variation of each assembly as a result of the overall pressure ratio scaling

The change in pressure ratio is mainly affecting the turbine stage design. The decrease in pressure ratio leads to taller blades. If the aspect ratio is kept constant, the blades become also longer, increasing the weight of the disks by a large margin, as shown in Table 4.20. The gas generator turbine increases in weight by 27.7% and the free power turbine by 39.9% even if the output power is lower for both.

The increase in pressure ratio reduces the weight of the gas generator turbine for the same reason described earlier: the blades become shorter due to higher pressure, whereas the weight of the free power turbine is increased, mainly due to the increased weight of the disks.

Overall the pressure ratio does not have a large impact on the total engine weight. If the aspect ratios of the

blades were adjusted given the taller blades, the difference in weight would probably be even lower.

4.6.3. TURBINE INLET TEMPERATURE

The sensitivity of the engine weight to the variation in turbine inlet temperature was evaluated by varying the design turbine inlet temperature of the engine ($TIT = 1450K$) by $\pm 100K$.

The inputs of the model are left the same of Section 4.5.1 except for the turbine inlet temperature and the design power output of the free power turbine, which is reduced to allow the free power turbine to have the same outlet total pressure as the original design. The power outputs of the turbine stages are reported in Table 4.21.

	$TIT = 1350$	$TIT = 1450$	$TIT = 1550$
Component [-]	**Power [kW]**	**Power [kW]**	**Power [kW]**
FPT	814.6	970	1126.2

Table 4.21: Adjusted turbine powers for turbine inlet temperature for the MTR390 engine model

Alternatively, the engine mass flow rate through the engine can be adjusted in order to match the power output of the original engine. In this case, the turbine power changes as in Table 4.22.

	$TIT = 1350$ $1.19 \cdot \dot{m}_{nominal}$	$TIT = 1450$ $\dot{m}_{nominal}$	$TIT = 1550$ $0.86 \cdot \dot{m}_{nominal}$
Component [-]	**Power [kW]**	**Power [kW]**	**Power [kW]**
HPT	1428	1200	1032
FPT	970	970	970

Table 4.22: Adjusted turbine powers for mass flow scaling for the MTR390 engine model to match the output power of the original engine with different turbine inlet temperatures

Figures 4.28,4.29, 4.31, and 4.31 show the estimated engine geometries of the four analysed engines, the rest of the results are reported in Tables 4.23 and 4.24.

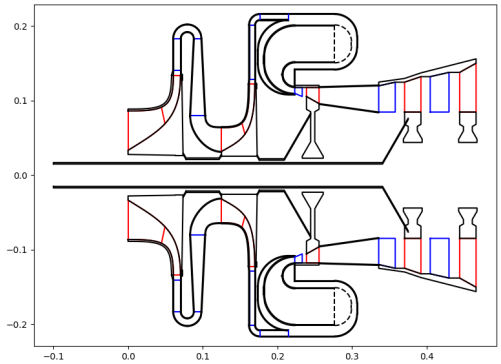

Figure 4.28: Mechanical design results of the MTR390-2C turboshaft engine with $TIT = 1350$

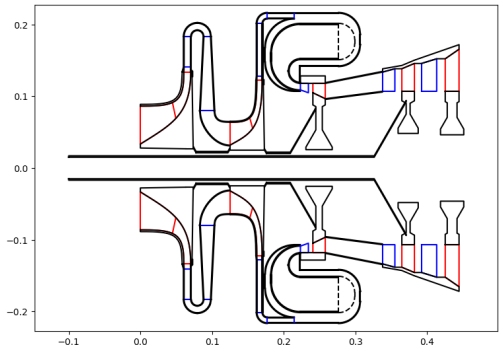

Figure 4.29: Mechanical design results of the MTR390-2C turboshaft enginewith $TIT = 1550$

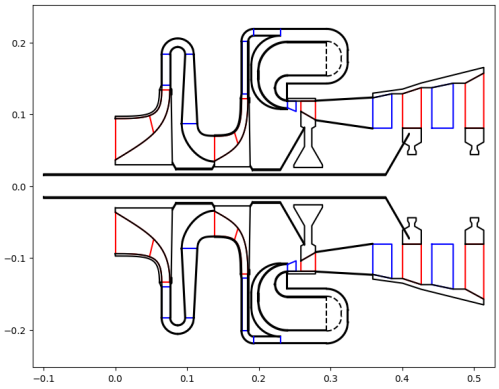

Figure 4.30: Mechanical design results of the MTR390-2C turboshaft engine with $TIT = 1350$ and $\dot{m} = 1.19 \cdot \dot{m}_{nominal}$

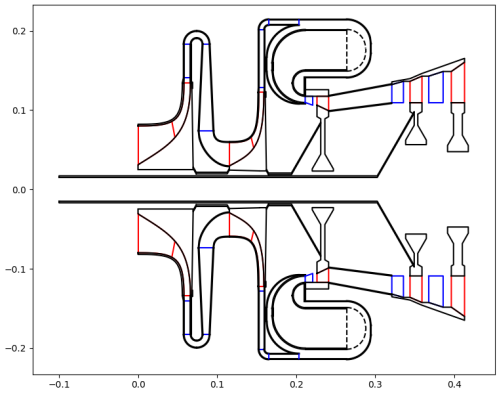

Figure 4.31: Mechanical design results of the MTR390-2C turboshaft enginewith $TIT = 1550$ and $\dot{m} = 0.86 \cdot \dot{m}_{nominal}$

	$TIT = 1350$	$TIT = 1350$ $\dot{m} = 119\%$	$TIT = 1450$	$TIT = 1550$	$TIT = 1550$ $\dot{m} = 86\%$
Component [-]	**Weight** [kg]	**Weight** [kg]	**Weight** [kg]	**Weight** [kg]	**Weight** [kg]
First stage compressor	7.01	8.51	7.01	7.01	6.16
casing	2.31	2.69	2.31	2.31	2.07
disk + blades	4.59	5.65	4.59	4.59	4.02
stator vanes	0.11	0.17	0.11	0.11	0.08
inter-compressor connecting shaft	0.11	0.14	0.11	0.11	0.10
First stage inlet frame	3.76	4.47	3.76	3.76	3.23
Return channel	2.55	2.64	2.55	2.55	2.42
vanes	0.55	0.58	0.55	0.55	0.48
Second stage compressor	4.35	4.87	4.35	4.35	3.96
casing	2.06	2.23	2.06	2.06	1.94
disk + blades	2.10	2.39	2.10	2.10	1.88
stator vanes	0.19	0.25	0.19	0.19	0.13
Combustor	37.51	38.43	37.51	37.52	36.83
de-swirler vanes	0.10	0.11	0.10	0.10	0.08
de-swirler duct	0.79	0.77	0.79	0.79	0.80
casing + liner	6.68	6.85	6.68	6.69	6.57
frame	29.74	30.49	29.74	29.74	29.20
Gas generator turbine	3.53	5.44	4.64	6.19	4.17
Inter-turbine frame	8.85	8.96	8.87	8.89	8.80
Turbine connecting duct	0.82	0.82	0.86	0.89	0.90
Free power turbine	15.74	20.28	12.57	17.53	13.20
Free power turbine frame	9.07	9.67	9.35	10.39	9.93
Gas generator shaft	0.26	0.27	0.26	0.26	0.25
Power output shaft	0.85	0.89	0.87	0.91	0.89
Accessories	15.62	17.47	15.33	16.61	15.03
Total weight	107.48	120.20	105.48	114.31	103.45

Table 4.23: Design results of the MTR390-2C turboshaft engine

	$TIT = 1350$	$TIT = 1350$ $\dot{m} = 119\%$	$TIT = 1550$	$TIT = 1550$ $\dot{m} = 86\%$
Assembly [-]	**ΔWeight** [%]	**ΔWeight** [%]	**ΔWeight** [%]	**ΔWeight** [%]
First stage compressor	+0.0	+21.4	+0.0	-12.1
Return channel	+0.0	+3.5	+0.0	-5.1
Second stage compressor	+0.0	+12.0	+0.0	-9.0
Combustor	+0.0	+2.5	+0.0	-1.8
Gas generator turbine	-23.9	+17.2	+33.4	-10.1
Turbine connecting duct	-4.7	-4.7	+3.5	+4.7
Free power turbine	+25.2	+61.3	+39.5	+5.0
Frames	-0.6	+3.6	+2.0	-1.0
Total	+1.9	+14.0	+8.4	-1.9

Table 4.24: Weight variation of each assembly as a result of the turbine inlet temperature scaling

The trend shown by the results in Tables 4.23 and 4.24 is quite interesting; if the turbine inlet temperature is changed without scaling the mass flow rate of the engine, the compressor assembly does not change at all, whereas all effects are concentrated in the turbine stages.

As could be expected, a lower turbine inlet temperature reduces the weight of the gas generator turbine, as the thickness of the casing can be lower, as well as the thickness of the disk. This results in a weight reduction of the turbine by −23.9%. The opposite effect is observed in the case of increased turbine inlet temperature: the increased thickness of the casing and volume of the disk cause an increase in weight of 33.4%.

If the mass flow rate is not adjusted to maintain the nominal engine power output constant, the free power turbine weight always increases regardless of the turbine inlet temperature value. In the case of lowered TIT, this effect can be attributed most likely to the same phenomenon described for OPR scaling (Section 4.6.2), where the height of the flow channel becomes larger if the OPR is reduced and therefore the blades and the disks are axially longer as the aspect ratio is the same. In the case of increased TIT, the higher weight can be attributed to the overall higher power output and operating temperature of the stage, which increase the structural loads on the disks.

The weights of the various frames, being only a function of the outer radius, do not vary a lot. However, as they represent about half of the total engine's estimated weight, a variation of 2% of the weight of the frames, as is the case for $TIT = 1550$, can contribute alone to about 15% of the total engine weight increase, or 1.3% of the original engine's weight.

If the mass flow rate was scaled to match the power output of the original engine, the same effects to what was discussed in section 4.6.1 with regards to the mass flow scaling, are observed. It is worth mentioning that the model with $TIT = 1550$ yields a lower weight by −1.9% compared to the original engine, as the same power output can be achieved with a lower mass flow rate if the turbine inlet temperature is increased.

5

CONCLUSIONS AND RECOMMENDATIONS

The chapter is divided into three main sections, corresponding to the three main modeling activities described in this thesis, with an additional fourth section dedicated to recommendations on the future development of the WEST tool.

5.1. ASPECT RATIO OF AXIAL COMPRESSOR BLADES

WEST is conceived as a preliminary design and component-based weight estimation method for turbine engines given high-level thermodynamic specifications and design inputs. However, the methodology for the preliminary design implemented in WEST for axial compressors requires information about the blade geometry, such as the blade aspect ratio, that the user may find difficult to specify properly.

The primary objective of the first part of the thesis work was to investigate potential approaches for automatically determining the optimal aspect ratio of the blades of axial compressor stages, minimizing number of required model inputs.

An overview of the available literature on blade aspect ratios in axial compressors was presented in Section 2.1. Subsequently, an in-depth analysis using computational fluid dynamics was conducted to gain a comprehensive understanding of this design problem.

No real consensus was found in the literature on the effect of aspect ratio on axial compressor efficiency or on possible preliminary methods to determine optimal blade aspect ratios in the meanline design phase.

A series of CFD based optimizations was conducted on a sample compressor stage using the MULTALL[40] software while varying the number of blades, flow coefficient and work coefficient of the stage, in order to obtain a better understanding of the interaction between these parameters and the resulting optimal range of blade aspect ratio.

A similar analysis was performed with a meanline code implementing empirical models for the estimation of stage losses, yielding very similar results to the CFD-based optimization study.

Based on information reported by E. Steinhardt [1], it was hypothesized that the optimal aspect ratio may vary as a function of the stage work coefficient. This hypothesis was further supported by observing the historical trend in axial compressor design, which shows an increase in work coefficient and a decrease in aspect ratio the more modern the engine[2].

The simulations successfully reproduced the trends observed in the literature, but the initial objective of implementing a fully automated method to determine the optimal aspect ratio was not fully achieved. Nonetheless, the study provided valuable insights into the compressor blade design problem.

The main challenge lies in the strong relation between the optimal aspect ratio and the solidity or number of blades of the stage. From an aerodynamics perspective, the results might suggest that the optimal compressor design solution is to adopt "infinitely many, infinitely thin" blades. At the same time, this solution is impractical for both structural and manufacturing considerations. A rough estimation of stresses indicated that structural limitations might be more related to vibrations and fluid-structure interactions than mechanical stresses. At the same time, the WEST software does not allow for an evaluation of these effects.

Nevertheless, the results obtained using the meanline code showed that if the optimal solidity/number of blades could be defined independently of the aspect ratio, this code could be effectively used to determine the optimal aspect ratio.

A potential solution to address the interdependence between the aspect ratio and the solidity/number of blades in the stage has been identified in the criterion introduced by Lieblein [42, 19]. This criterion offers a means to estimate the optimal stage solidity solely based on velocity triangles, provided that an assumption is made about the diffusion factor. By employing this approach it became possible to replicate the trend outlined by Steinhardt [1]. However, it is worth noting that the calculated efficiency of stage configurations with optimal aspect ratios obtained through this method was lower than what achieved when the aspect ratio was varied independently of blade count.

Further research into how Lieblein's criterion can be combined with meanline-based loss models to estimate the optimal aspect ratio during the preliminary design phase is highly likely to yield promising results for the future development of the WEST tool. If this method is rigorously validated through comparisons with designs from existing engines, it could potentially be integrated into WEST to determine the aspect ratio of axial compressor stages without necessitating additional user inputs.

5.2. MODELLING OF RADIAL COMPRESSORS

Large turbofan engines rely on axial turbomachinery to handle significant mass flow rates, while smaller turboshafts feature axial and radial stages, or even a combination of the two technologies.

Given the interest in the ARENA project in small-capacity turboshafts, the WEST tool was then extended to deal with radial compressors.

The design of the radial compressor stage can be divided into three main steps: the definition of the flow path (blades and diffuser vanes), the sizing of the disks, and the casing. The implented design procedure follows this sequence.

More in detail, the meanline code follows the preliminary meanline design procedure detailed by M. Gambini, M. Vellini [5], and R.H. Aungier [43]. The calculation procedure involves two nested iterative loops: one to determine the stage efficiency based on loss models and a second one to ensure that the effective total-to-total pressure ratio of the compressor meets the design requirement. The first loop is omitted in case the efficiency is provided as input by the user.

In order to more precisely design the impeller disk, a new preliminary stress analysis methodology was developed, based on the works by Schilhansl [11] and Ray et al. [9]; this method estimates the radial and tangential stress distributions in the impeller disk caused by mechanical as well as thermal loads. The developed methodology was validated by comparing the results with those of a finite element model of a radial compressor developed by A.Giuffrè [12]. The comparison shows a very good accuracy of the implemented analytical method in predicting the stress distribution in the disk.

The developed stress analysis methodology was also adapted to calculate the stresses in axial turbomachinery disks, greatly decreasing the computational time without any accuracy penalty with respect to the algorithm previously implemented in WEST. This is a remarkable achievement given that the disk sizing procedure is called by an optimizer to minimize the engine weight.

5.3. MODELLING OF TURBOSHAFT ENGINES

To perform the modeling of turboshaft engines, several additional components were added to the WEST tool. These include the return channel, which connects multiple radial compressor stages, and the reverse-flow combustor, commonly found in compact turboshaft engines. Additionally, some adjustments were made to the existing methodology to account for specific characteristics of turboshafts, such as integrated gearboxes, blisks and shrouded turbine blades.

To validate the accuracy of the tool, two existing turboshaft engines were simulated using the WEST software: the MTU Turbomeca Rolls-Royce MTR390 and the General Electric T700 (Sections 4.5.1 and 4.5.2).

The total weights of the two engines were found to be highly underestimated, whereas the predicted flow path and the geometry of other engine components match very closely the actual engines. As the weight estimation method does not model all engine components (missing elements include, but are not only limited to: engine outer casing, inlet and outlet ducts, gearbox accessories, turbine shrouds...)the underestimation

of the engine weight was expected. Large uncertainty is also introduced by the gearbox model, as in some cases different empirical methods yielded very different weight estimates, such as in the case of the MTR390 integrated gearbox.

The lack of available data about component weights of turboshaft engines prevents a thorough validation of the WEST tool, though the good match with the actual engine geometry and the physical soundness of the generated designs gives some confidence in the accuracy of the weight estimation method.

It is hypothesized that if more components of the engine are modelled and a detailed turboshaft weight breakdown is available, the results will turn out to be more accurate than what can be concluded at first glance.

A sensitivity study was performed on the model of the MTU Turbomeca Rolls-Royce MTR390 to estimate how the geometry and weight of the engine would vary when some of the high-level design parameters are changed. The parameters taken into consideration for this study are the air mass flow rate, the overall pressure ratio and the turbine inlet temperature.

The behaviour of the engine model follows the expected outcome for a change in mass flow rate through the engine. Increasing the mass flow rate leads to a higher weight in every component of the engine, and the opposite effect is obtained if the mass flow rate is decreased. The relative change in engine mass is about half of the relative change in mass flow rate: the mass of the engine increases by 15% with a mass flow rate increase of 25% and decreases by −13% with a mass flow rate decrease of −25%.

The weight of the engine is not affected as much by the overall pressure ratio as it is by the mass flow rate; the main effect of the design change is observed in the combustor and the turbines. A lower pressure ratio leads to a wider flow passage through the turbine stages. The taller and wider turbine blades require bigger disks, and thus the overall weight is increased. If the pressure ratio is increased, however, the outer radius of the combustor and turbines increases; this mainly affects the weight of the frames, which accounts for most of the increase in engine weight.

The turbine inlet temperature was varied in four test cases; in two cases the temperature was increased and decreased and the mass flow rate through the engine was kept constant, while in the other two cases the mass flow rate was adjusted so that the power output of the engine remained constant. If the mass flow rate is kept constant, the compressor and combustor are not affected by the change in turbine inlet temperature. The weight of the engine is slightly higher if the turbine inlet temperature is either increased or decreased. If the mass flow rate is adjusted, however, the increased turbine inlet temperature case yields an engine design with a lower weight than the original engine model.

The validation of the WEST models against the data of real engines and the outcomes of the sensitivity analysis demonstrate that the tool is capable of providing consistent and realistic results for a variety of design inputs. The development of the tool is not complete, and some additional features and improvements can be implemented in the future. Some suggestions on possible improvements are listed in Section 5.4.

5.4. RECOMMENDATIONS

The aim of this section is to present new ideas or possible adaptations that can lead to a further improvement of the WEST preliminary engine design methodology and weight estimation. These recommendations are organized into three main categories:

- Extensions of the current methodology (Section 5.4.1). In this section, suggestions are provided for expanding the capabilities of the current methodologies. This includes additional features and component models to broaden the range of engines that can be modeled.
- Improvements to the current methodology (Section 5.4.2). This section addresses potential enhancements and refinements of the existing methodologiy to increase the accuracy, efficiency, or usability of the program.
- Computational cost reduction (Section 5.4.3). Here, strategies for reducing the computational burden of the program are discussed. This is crucial to make the tool suitable for extensive optimization studies.

5.4.1. POSSIBLE EXTENSIONS OF THE TOOL

- The current model for radial compressor stages can be modified with relative minor efforts to include the possibility of adopting a volute instead of a 90^o bend at the outlet of the vaned diffuser. This would

allow the user to model compressor stages of smaller-scale gas generators, such as those of auxiliary power units.

- A detailed component-based model may be added for the gearbox weight estimation. This would allow for a more precise estimation of the weight of the gearbox often attached to turboshaft engines.
- A model for the fan of the turbofan engines, and for propellers of turboprop engines can be added to the program. This would expand the modelling capabilities of the program.
- Materials and related temperature-dependent properties database of the program can be extended. WATE++ [51] and GTlab [45] databases are valuable resources for this purpose. By incorporating a wider range of materials, such as advanced alloys, composites, and coatings in WEST the user will have more options to properly model the various engine components.
- Models of other common components of turboshaft engines, such as inlet particle separators, variable geometry guide vanes and inlet ducts, should be added to the program. This will both expand the modelling capabilities of the program and aide in the validation of the existing models, as discussed in the previous section.
- A model for radial inflow turbines is still missing. This would allow to model the turbine stages of many small scale gas generators, such as those of auxiliary power units.

5.4.2. METHOD IMPROVEMENTS

- If the method based on Lieblein's [42, 19] criterion is rigorously validated through comparisons with designs from existing engines, it could potentially be integrated into WEST to determine the aspect ratio of axial compressor stages without necessitating additional user inputs. A similar procedure can be done for axial turbine stages as well. Alternatively, the geometrical correlations by Greitzer et al. [4] can be implemented to determine the aspect ratio of the stage based only on the blade height.
- To improve the method for determining the number of blades in an axial compressor row in WEST and ensure accuracy, it is recommended to use the true chord instead of the axial chord when calculating the maximum pitch, in accordance with the original model.
- The temperature distribution assumed in radial compressor disks can be improved by modeling the heat transfer through the disk. This procedure may be implemented for axial turbomachinery as well.
- The reverse-flow combustor model can be improved by incorporating a more physically-based procedure for the preliminary design of this component.
- The annular combustor geometry should be adapted make it more compliant with the channel shape used in turboshaft engine applications where the component is connected to the outlet of a radial compressor stage, as during the validation steps it was found that the available geometry model did not align well with the T700 annular combustor.
- The accuracy of thermodynamic calculations can be increased by accounting for the variation of the working fluid thermodynamic properties with temperature.
- The implementation of a methodology to calculate the stresses in impeller blades would allow for a better, more phisically-based, estimation of the blade thickness.
- The stress calculation procedure should take into account the taper of the blade thickness between the root and tip.
- The minimum thickness of the disk tip may be calculated based on a minimization of the displacement at that location, as presented by Zheng et al. [63], given the fluid force acting on the disk. A method to estimate this force is then required.
- The radial compressor weight estimation should account for the possibility of inlet guide vanes,in a similar way as already done in WEST for axial compressors.

5.4.3. COMPUTATIONAL COSTS

The computation time of the program, which is mainly affected by the disk geometry optimization procedure, has been significantly reduced thanks to the developed stress calculation procedure.

In order to further reduce computational costs, the discretization technique used for both axial and radial turbomachinery disks can be adjusted to allow for a nonuniform distribution of the element radial thickness. Mesh refinements can be adopted around thickness discontinuities or areas of abrupt change in the geometry. The accuracy of the results can be improved or preserved even if the number of total elements is reduced.

Reducing the number of elements would lead to a reduction in the computation time required by the program.

A

MEANLINE LOSS MODEL FOR AXIAL COMPRESSORS

In this appendix the full set of loss models used for the analysis of axial compressors in section 2.4.1 is reported and briefly explained.

This set is mostly based on the equations provided in the book by M.Gambini and M.Vellini [5] with some minor adjustments.

A.1. PRESSURE LOSS BREAKDOWN

the total pressure loss coefficients for the rotor and stator are defined as follows, with station 1 being at the inlet of the rotor, station 2 being between the rotor and the stator and station 3 being at the outlet of the stator.

$$Y_{tot,R} = \frac{p_{1tr} - p_{2tr}}{p_{1tr} - p_1} \tag{A.1}$$

$$Y_{tot,S} = \frac{p_{2t} - p_{3t}}{p_{2t} - p_2} \tag{A.2}$$

Where p_{-tr} is the relative total pressure (based on relative velocities), p_{-t} is the total pressure and p_- the static pressure; the total loss coefficient combines the profile losses, secondary losses, endwall losses, shockwave losses and tip clearance losses:

$$Y_{tot,-} = Y_p + Y_s + Y_{ew} + Y_{shock} + Y_{TC} \tag{A.3}$$

A.1.1. PROFILE LOSSES

The full set of equations as given by the book [5] is reported here, no detailed explanation will be given for these equations as it is already provided by the authors, the full set is only included for completeness and repeatability of the results.

$$Y_p = 2 \cdot \frac{\theta_{2,C} \cdot \sigma}{\cos(\beta_2)} \cdot \left(\frac{\cos(\beta_1)}{\cos(\beta_2)}\right)^2 \cdot \frac{2 \cdot H_{te}}{3 \cdot H_{te} - 1} \cdot \left(1 - \frac{\theta_{2,C} \cdot \sigma \cdot H_{te}}{\cos(\beta_2)}\right)^{-3} \tag{A.4}$$

The calculation of the profile losses is based on the model proposed by Lieblein [64] (equation A.4) and for which the profile losses depend on the boundary-layer momentum thickness at the blade outlet (θ_2), which in this case is expressed as a ratio with the blade chord ($\theta_{2,C} = \theta_2 / C$) and the boundary layer trailing-edge shape factor (H_{TE}).

These two parameters are calculated with the method provided by Koch and Smith [65] shown in equations A.5 through A.22.

$$K_1 = 0.2445 \ , \ K_2 = 0.4458 \ , \ K_3 = 0.7688 \ , \ K_4 = 0.6024 \tag{A.5}$$

$$\Gamma = \frac{(\tan(\beta_1) - \tan(\beta_2))\cos(\beta_1)}{\sigma} \tag{A.6}$$

$$A_{throat} = A_1 - \frac{1}{3}(A_1 - A_2) \tag{A.7}$$

$$A_{o,throat} = \left(1.0 - K_2\sigma\frac{t/c_{max}}{\cos\left(\frac{\beta_1+\beta_2}{2}\right)}\right)\frac{A_{throat}}{A_1} \tag{A.8}$$

$$\rho_t/\rho_1 = 1 - \frac{M_{1,rel}^2}{1-M_{1,rel}^2}\left(1 - A_{o,throat} - K_1\sigma\Gamma\tan(\beta_1)/\cos(\beta_1)\right) \tag{A.9}$$

$$DF_{eq} = \frac{w_1}{w_2}(1 + K_3(t/c_{max}) + K_4\Gamma)\sqrt{(\sin(\beta_1) - K_1\sigma\Gamma)^2 + \left(\frac{\cos(\beta_1)}{A_{o,throat}\rho_t/\rho_1}\right)^2} \tag{A.10}$$

$$\theta_{2,C_0} = 2.664\times10^{-3}DF_{eq} - 1.519\times10^{-4} + \frac{6.713\times10^{-3}}{2.60 - DF_{eq}} \tag{A.11}$$

$$H_{te,0} = \begin{cases}(0.91 + 0.35DF_{eq})(1 + 0.48(DF_{eq}-1)^4 + 0.21(DF_{eq}-1)^6) & \text{if } DF_{eq} \le 2\\ 2.7209 & \text{otherwise}\end{cases} \tag{A.12}$$

$$n = 2.853 + DF_{eq}(-0.97747 + 0.19477DF_{eq}) \tag{A.13}$$

$$\zeta_m = 1.0 + (0.11757 - 0.16983DF_{eq})M_{tot}^n \tag{A.14}$$

$$\zeta_h = 0.53\frac{h_b(1)}{h_b(2)} + 0.47 \tag{A.15}$$

$$Re_{cr} = 100\frac{c}{k_s} \tag{A.16}$$

$$\zeta_{re} = \begin{cases}(1\times10^6/Re1)^{0.166} & \text{if } Re1 \le Re_{cr} \;\&\; Re1 \ge 2\times10^5\\ 1.30626\times(2\times10^5/Re1)^{0.5} & \text{if } Re1 \le Re_{cr} \;\&\; Re1 < 2\times10^5\\ (1\times10^6/Re_{cr})^{0.166} & \text{if } Re1 > Re_{cr} \;\&\; Re_{cr} \ge 2\times10^5\\ 1.30626\times(2\times10^5/Re_{cr})^{0.5} & \text{if } Re1 > Re_{cr} \;\&\; Re_{cr} < 2\times10^5\end{cases} \tag{A.17}$$

$$\eta_m = 1.0 + (0.10725 + DF_{eq}\cdot(-0.8671 + 0.18043\cdot DF_{eq}))\cdot M_{tot}^{1.8} \tag{A.18}$$

$$\eta_h = 1.0 + \frac{h_{b,1}}{h_{b,2}}\cdot(0.0026\cdot DF_{eq}^8 - 0.024); \tag{A.19}$$

$$\eta_{re} = \begin{cases}1\times10^6/Re1 & Re1 < Re_{cr}\\ (1\times10^6/Re_{cr})^{0.06} & \text{otherwise}\end{cases} \tag{A.20}$$

$$\theta_{2,C} = \theta_{2,C_0}\cdot\zeta_m\cdot\zeta_h\cdot\zeta_{re}; \tag{A.21}$$

$$H_{te} = H_{te_0}\cdot\eta_m\cdot\eta_h\cdot\eta_{re} \tag{A.22}$$

A.1.2. SECONDARY LOSSES

Secondary losses are evaluated using the model by Howell [66]:

$$\beta_M = \arctan\left(\frac{\tan(\beta_1) + \tan(\beta_2)}{2}\right) \tag{A.23}$$

$$c_L = \left|\frac{2}{\sigma}\cos(\beta_M)(\tan(\beta_1) - \tan(\beta_2))\right|; \tag{A.24}$$

$$Y_s = 0.018\cdot\frac{\sigma\cdot\cos(\beta_1)^2}{\cos(\beta_M)^3}\cdot c_L^2; \tag{A.25}$$

A.1.3. END WALL LOSSES

End wall losses are calculated by using the correlation proposed by Aungier [67]:

$$Y_{ew} = 0.0146 \cdot \frac{1}{AR} \cdot \left(\frac{\cos(\beta_1)}{\cos(\beta_2)} \right)^2 \tag{A.26}$$

A.1.4. SHOCK WAVE LOSSES

Shock wave losses are calculated from an interpoaltion of the data provided by Koch and Smith [65]:

$$Y_{shock} = \begin{cases} 0.32 M_{1,rel}^2 - 0.62 M_{1,rel} + 0.3 & \text{if } M_{1,rel} \geq 1 \\ 0 & \text{otherwise} \end{cases} \tag{A.27}$$

A.1.5. TIP CLEARANCE LOSSES

Tip clearance losses can be calculated by using the correlations of Yaras and Sjolander [68]:

$$K_E = 0.5 \ , \ K_G = 1.0 \ , \ \tau / h_b = 1\% \tag{A.28}$$

$$Y_{tip} = 1.4 \cdot K_E \cdot \sigma \cdot (\tau / h_b) \cdot cos^2(\beta_1) / cos^3(\beta_M) \cdot c_L^{1.5} \tag{A.29}$$

$$Y_{gap} = 0.0049 \cdot K_G \cdot \sigma \cdot \frac{1}{AR} \cdot \sqrt{c_L} / cos(\beta_M) \tag{A.30}$$

$$Y_{TC} = Y_{tip} + Y_{gap} \tag{A.31}$$

B

TIP DIAMETER RATIO OF A RADIAL COMPRESSOR GIVEN THE MEANLINE INPUT PARAMETERS

At the beginning of the radial compressor flow path meanline design, the tip and hub diameter ratios of the stage have to be determined in order to establish the dimensions of the inlet of the stage, this appendix shows how this step is accomplished.

First the isentropic total temperature at the outlet of the stage has to be calculated:

$$T_{3t_{\text{is}}} = T_{1t} \cdot (\beta_{tt})^{\frac{\gamma-1}{\gamma}} \tag{B.1}$$

This allows to compute the specific work of the stage:

$$w = c_p \cdot (T_{3t_{\text{is}}} - T_{1t}) \tag{B.2}$$

From the definition of work coefficient and flow coefficient the rotational velocities at the tip of the impeller (outlet) and the inlet absolute flow velocity are then computed (the full procedure for the computation of the velocity triangles is reported in section 3.1.3):

$$u_2 = \sqrt{\frac{w}{\psi}} \tag{B.3}$$

$$v_1 = u_2 \cdot \phi \cdot \sqrt{1 + \tan^2(\alpha_1)} \tag{B.4}$$

$$v_{1,m} = u_2 \cdot \phi \tag{B.5}$$

The thermodynamics at the inlet of the stage, such as static enthalpy, static temperature, mach number, static pressure and density can be then computed based on the velocity and the inlet flow characteristics:

$$h_{1t} = T_{1t} \cdot c_p \tag{B.6}$$

$$h_1 = h_{1t} - \frac{v_1^2}{2} \tag{B.7}$$

$$T_1 = \frac{h_1}{c_p} \tag{B.8}$$

$$m_1 = \frac{v_1}{\sqrt{\gamma \cdot R \cdot T_1}} \tag{B.9}$$

$$p_1 = \frac{p_{1t}}{\left(1 + \frac{\gamma-1}{2} \cdot m_1^2\right)^{\frac{\gamma}{\gamma-1}}} \tag{B.10}$$

$$\rho_1 = \frac{p_1}{R \cdot T_1} \tag{B.11}$$

After the thermodynamic parameters at the inlet of the stage are determined, the volumetric flow rate at the inlet can be calculated:

$$\dot{v}_1 = \frac{\dot{m}_a}{\rho_1} \tag{B.12}$$

As both the volumetric flow rate and the inlet meridional velocities are known, the area at the inlet can be easily computed:

$$A_1 = \frac{\dot{v}_1}{v_{1m}} \tag{B.13}$$

From the outlet rotational velocity and the rotational speed of the impeller, the outlet diameter can be obtained:

$$D_2 = \frac{60}{\pi} \cdot \frac{u_2}{\Omega} \tag{B.14}$$

Once the area is calculated, all dimensions of the inlet can be derived if the impeller shape factor (k) is known:

$$D_{1,t} = \sqrt{\frac{4A_1}{k \cdot \pi}} \tag{B.15}$$

$$\delta_t = \frac{D_{1,t}}{D_2} \tag{B.16}$$

$$\delta_h = \sqrt{\delta_t^2 - \frac{4A_1}{\pi \cdot D_2^2}} \tag{B.17}$$

$$D_{1,h} = \delta_h \cdot D_2 \tag{B.18}$$

C

Stress Analysis Calculation Procedure

This appendix reports the full calculation procedure used for the centrifugal and thermal stresses in a radial compressor disk, mainly based on the work of Schilhansl [11] and Ray et al. [9].

What is provided here is intended to supplement the procedure detailed in section 3.3.2 providing all data so that it may be possible to replicate.

The procedure is based on the hypothesis that the stresses in the impeller disk and blades follow these stress-strain relations:

$$\sigma_{r,D} = \frac{E}{1-\nu^2} \cdot \left(\epsilon_r + \nu\epsilon_t - (1+\nu)\alpha_{exp}\Delta T\right) \tag{C.1}$$

$$\sigma_{t,D} = \frac{E}{1-\nu^2} \cdot \left(\epsilon_t + \nu\epsilon_r - (1+\nu)\alpha_{exp}\Delta T\right) \tag{C.2}$$

And for the blade:

$$\sigma_{r,B} = E \cdot \left(\epsilon_r - \alpha_{exp}\Delta T\right) \tag{C.3}$$

where the strain in the radial direction, ϵ_r and the strain in the tangential direction ϵ_t are expressed as a function of the radial displacement and rotation, as done in section 3.3.2.

The restoring forces at the interface between the volume elements can be computed as a function of the radial stresses at each location:

$$S = S_{blade} + S_{disk} = \int_{z_1}^{z_2} \sigma_{r,B} t_B dz + \int_{z_2}^{z_3} \sigma_{r,D} r \Delta\Phi dz \tag{C.4}$$

$$M = -\int_{z_1}^{z_2} \sigma_{r,B} t_B z dz - \int_{z_2}^{z_3} \sigma_{r,D} r \Delta\Phi z dz \tag{C.5}$$

If the integrations are carried out applying the stress-strain correlations, the equilibrating force and moment can be expressed as follows:

$$S = s_\epsilon \cdot \epsilon_{r,0} + s_\beta \cdot \alpha' + s_u \cdot u_0 + s_\alpha \cdot \alpha + s_T \tag{C.6}$$

$$M = m_\epsilon \cdot \epsilon_{r,0} + m_\beta \cdot \alpha' + m_u \cdot u_0 + m_\alpha \cdot \alpha + m_T \tag{C.7}$$

Where all the constants are calculated through the integration and are reported in equations C.8 through C.15 as well as the expressions foe s_T and m_T reported in section 3.3.2.

$$m_{\epsilon,i} = -E\left(t_{B,i} \cdot \frac{\left(z_{2,i}^2 - z_{1,i}^2\right)}{2} + \frac{1}{1-\nu^2} \cdot r_i \Delta\Phi \cdot \frac{\left(z_{3,i}^2 - z_{2,i}^2\right)}{2}\right) \tag{C.8}$$

$$m_{\beta,i} = E\left(t_{B,i}\cdot\frac{\left(z_{2,i}^3 - z_{1,i}^3\right)}{3} + \frac{1}{1-\nu^2}\cdot r_i\Delta\Phi\cdot\frac{\left(z_{3,i}^3 - z_{2,i}^3\right)}{3}\right) \tag{C.9}$$

$$m_{u,i} = -\frac{E\nu}{1-\nu^2}\cdot\Delta\Phi\cdot\frac{\left(z_{3,i}^2 - z_{2,i}^2\right)}{2} \tag{C.10}$$

$$m_{\alpha,i} = \frac{E\nu}{1-\nu^2}\cdot\Delta\Phi\cdot\frac{\left(z_{3,i}^3 - z_{2,i}^3\right)}{3} \tag{C.11}$$

$$s_{\epsilon,i} = E\left(t_{B,i}\left(z_{2,i} - z_{1,i}\right) + \frac{1}{1-\nu^2}\cdot r_i\cdot\Delta\Phi\cdot\left(z_{3,i} - z_{2,i}\right)\right) \tag{C.12}$$

$$s_{\beta,i} = -E\left(t_{B,i}\cdot\frac{\left(z_{2,i}^2 - z_{1,i}^2\right)}{2} + \frac{1}{1-\nu^2}\cdot r_i\cdot\Delta\Phi\cdot\frac{\left(z_{3,i}^2 - z_{2,i}^2\right)}{2}\right) \tag{C.13}$$

$$s_{u,i} = E\cdot\frac{\nu}{1-\nu^2}\cdot\Delta\Phi\cdot\left(z_{3,i} - z_{2,i}\right) \tag{C.14}$$

$$s_{\alpha,i} = -E\cdot\frac{\nu}{1-\nu^2}\cdot\Delta\Phi\cdot\frac{\left(z_{3,i}^2 - z_{2,i}^2\right)}{2} \tag{C.15}$$

Equations C.6 and C.7 can be then manipulated to yield a calculation procedure for the quantities ϵ_{r0} and α':

$$\epsilon_{r0} = \epsilon_S\cdot S + \epsilon_M\cdot M + \epsilon_u\cdot u_0 + \epsilon_\alpha\cdot\alpha + \epsilon_T \tag{C.16}$$

$$\alpha' = \alpha_S\cdot S + \alpha_M\cdot M + \alpha_u\cdot u_0 + \alpha_\alpha\cdot\alpha + \alpha_T \tag{C.17}$$

Were all the constants are defined as reported in equations C.18 through C.27:

$$\epsilon_{s,i} = -\frac{m_{\beta,i}}{m_{\epsilon,i}\cdot s_{\beta,i} - m_{\beta,i}\cdot s_{\epsilon,i}} \tag{C.18}$$

$$\epsilon_{m,i} = \frac{s_{\beta,i}}{m_{\epsilon,i}\cdot s_{\beta,i} - m_{\beta,i}\cdot s_{\epsilon,i}} \tag{C.19}$$

$$\epsilon_{u,i} = -\frac{m_{u,i}\cdot s_{\beta,i} - m_{\beta,i}\cdot s_{u,i}}{m_{\epsilon,i}\cdot s_{\beta,i} - m_{\beta,i}\cdot s_{\epsilon,i}} \tag{C.20}$$

$$\epsilon_{\alpha,i} = -\frac{m_{\alpha,i}\cdot s_{\beta,i} - m_{\beta,i}\cdot s_{\alpha,i}}{m_{\epsilon,i}\cdot s_{\beta,i} - m_{\beta,i}\cdot s_{\epsilon,i}} \tag{C.21}$$

$$\epsilon_{T,i} = -\frac{m_{T,i}\cdot s_{\beta,i} - m_{\beta,i}\cdot s_{T,i}}{m_{\epsilon,i}\cdot s_{\beta,i} - m_{\beta,i}\cdot s_{\epsilon,i}} \tag{C.22}$$

$$\alpha_{s,i} = \frac{m_{\epsilon,i}}{m_{\epsilon,i}\cdot s_{\beta,i} - m_{\beta,i}\cdot s_{\epsilon,i}} \tag{C.23}$$

$$\alpha_{m,i} = -\frac{s_{\epsilon,i}}{m_{\epsilon,i}\cdot s_{\beta,i} - m_{\beta,i}\cdot s_{\epsilon,i}} \tag{C.24}$$

$$\alpha_{u,i} = -\frac{m_{\epsilon,i}\cdot s_{u,i} - m_{u,i}\cdot s_{\epsilon,i}}{m_{\epsilon,i}\cdot s_{\beta,i} - m_{\beta,i}\cdot s_{\epsilon,i}} \tag{C.25}$$

$$\alpha_{\alpha,i} = -\frac{m_{\epsilon,i}\cdot s_{\alpha,i} - m_{\alpha,i}\cdot s_{\epsilon,i}}{m_{\epsilon,i}\cdot s_{\beta,i} - m_{\beta,i}\cdot s_{\epsilon,i}} \tag{C.26}$$

$$\alpha_{T,i} = -\frac{m_{\epsilon,i}\cdot s_{T,i} - m_{T,i}\cdot s_{\epsilon,i}}{m_{\epsilon,i}\cdot s_{\beta,i} - m_{\beta,i}\cdot s_{\epsilon,i}} \tag{C.27}$$

The procedure presented in section 3.3.2 can then be followed to calculate the stresses in the disk.

D

WEIGHT OF ARBITRARY SHAPED DUCTS AND CASINGS

Many of the new elements added to the weight estimation program present casing curved casing or duct sections, the weight of these sections is calculated by multiplying the total volume occupied by the material with by the density of the material; however, the calculation of the volume is not trivial as the curved sections need to be revolved around the center line of the engine.

Each curved casing section is divided into volume elements, for each of these elements the volume is then calculated as if it was a diagonal casing section in the same way the volume of ducts and casings was already calculated by the program.

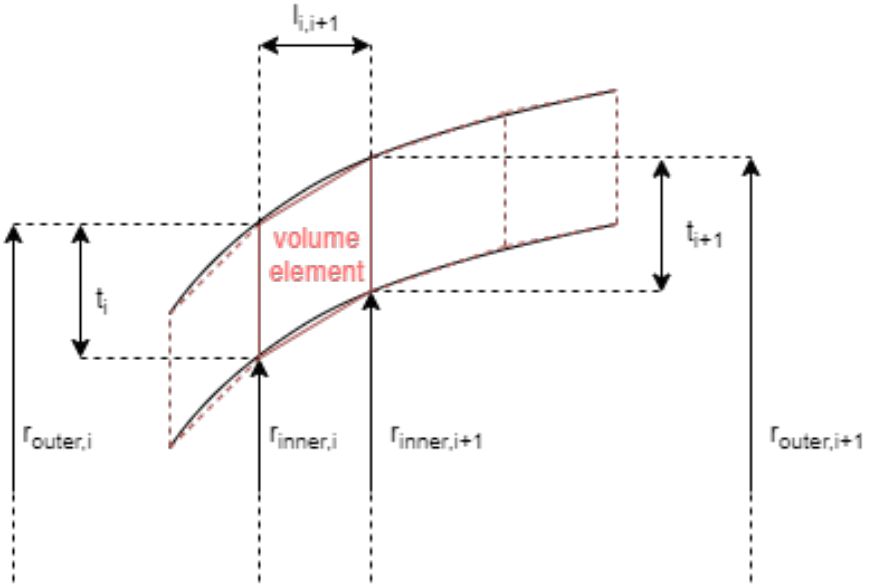

Figure D.1: schematic of the geometry of a volume element

The volume of each element is calculated as follows:

$$V_i = \frac{\pi \cdot l_{i,i+1}}{3}\left(\left(r_{outer,i}^2 + r_{outer,i} \cdot r_{outer,i+1} + r_{outer,i+1}^2\right) - \left(r_{inner,i}^2 + r_{inner,i} \cdot r_{inner,i+1} + r_{inner,i+1}^2\right)\right) \tag{D.1}$$

Then the total weight of the casing/duct section can be easily calculated:

$$m_{tot} = \rho_{mat} \cdot \sum_{i=1}^{N_{sections}} V_i \tag{D.2}$$

E

EXTENDED RESULTS

E.1. MTR390

E.1.1. FIRST STAGE COMPRESSOR

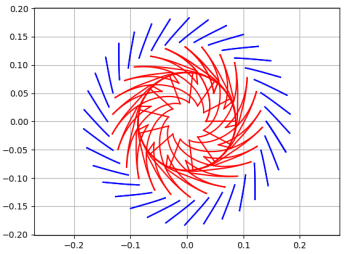

Figure E.1: Front view of the geometry of the MTR390 first stage radial compressor model stage rotor (red) and stator (blue) blades

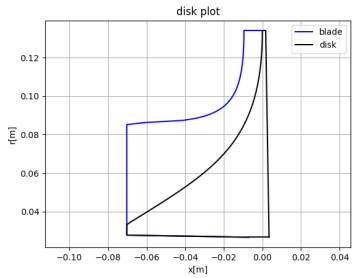

Figure E.2: Plot of the MTR390 first stage radial compressor model disk geometry

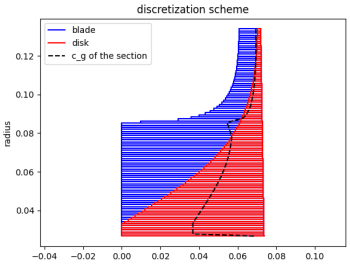

Figure E.3: Plot of the discretization of the MTR390 first stage radial compressor with 100 volume elements

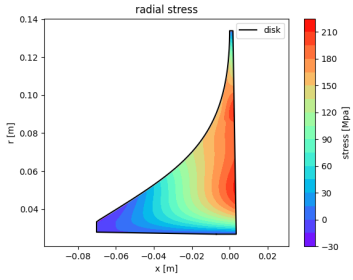

Figure E.4: Contour of the computed radial stress in the MTR390 first stage radial compressor disk

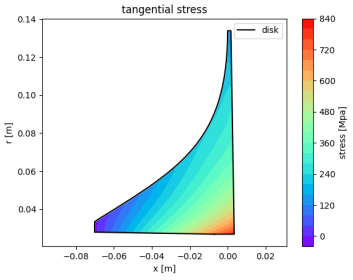

Figure E.5: Contour of the computed tangential stress in the MTR390 first stage radial compressor disk

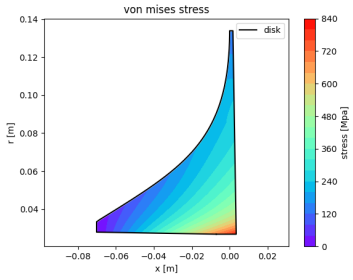

Figure E.6: Contour of the computed von Mises equivalent stress in the MTR390 first stage radial compressor disk

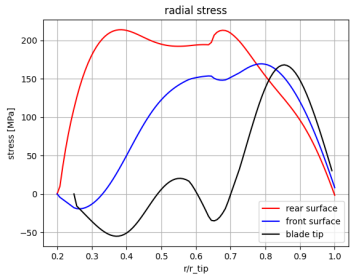

Figure E.7: Plot of the computed radial stress in the MTR390 first stage radial compressor disk at the front and back surfaces

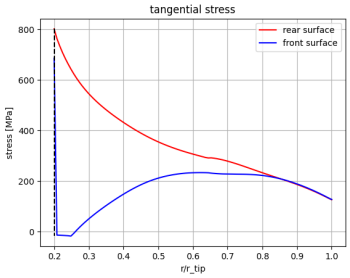

Figure E.8: Plot of the computed tangential stress in the MTR390 first stage radial compressor disk at the front and back surfaces

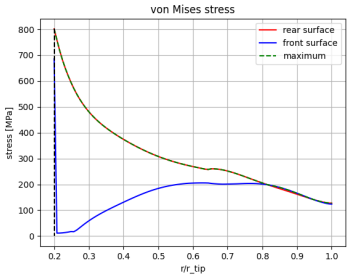

Figure E.9: Plot of the computed von Mises equivalent stress in the MTR390 first stage radial compressor disk at the front and back surfaces

E.1.2. SECOND STAGE COMPRESSOR

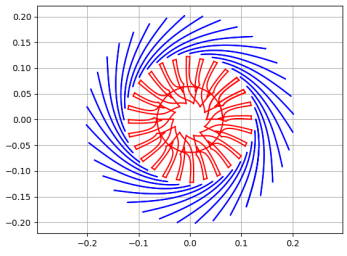

Figure E.10: Front view of the geometry of the MTR390 second stage radial compressor model stage rotor (red) and stator (blue) blades

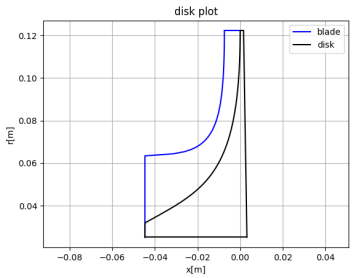

Figure E.11: Plot of the MTR390 second stage radial compressor model disk geometry

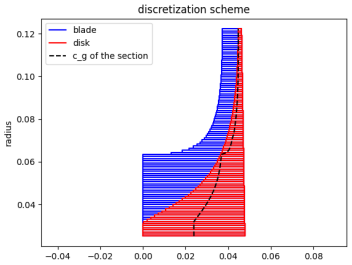

Figure E.12: Plot of the discretization of the MTR390 second stage radial compressor with 100 volume elements

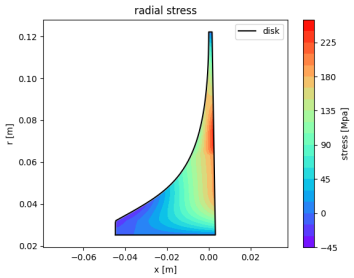

Figure E.13: Contour of the computed radial stress in the MTR390 second stage radial compressor disk

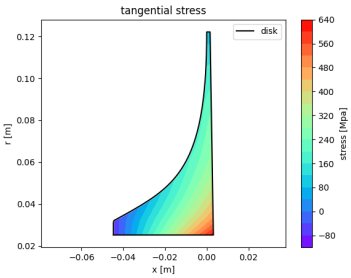

Figure E.14: Contour of the computed tangential stress in the MTR390 second stage radial compressor disk

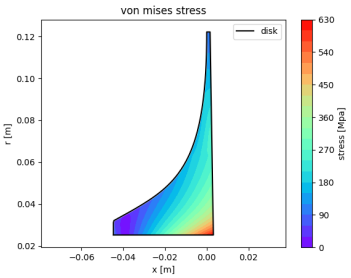

Figure E.15: Contour of the computed von Mises equivalent stress in the MTR390 second stage radial compressor disk

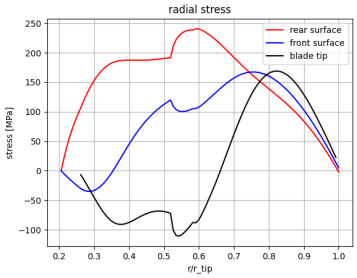

Figure E.16: Plot of the computed radial stress in the MTR390 second stage radial compressor disk at the front and back surfaces

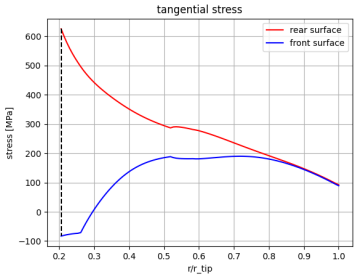

Figure E.17: Plot of the computed tangential stress in the MTR390 second stage radial compressor disk at the front and back surfaces

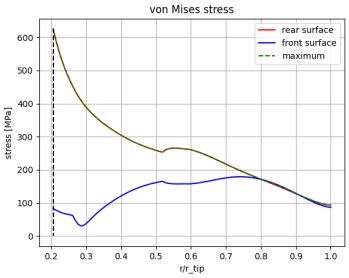

Figure E.18: Plot of the computed von Mises equivalent stress in the MTR390 second stage radial compressor disk at the front and back surfaces

E.2. T700

E.2.1. Radial Compressor

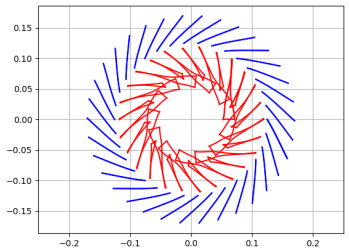

Figure E.19: Front view of the geometry of the T700 radial compressor model stage rotor (red) and stator (blue) blades

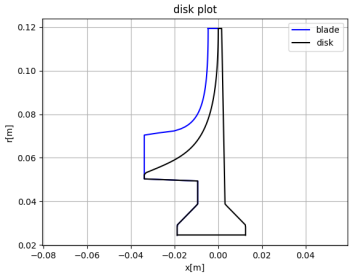

Figure E.20: Plot of the T700 radial compressor model disk geometry

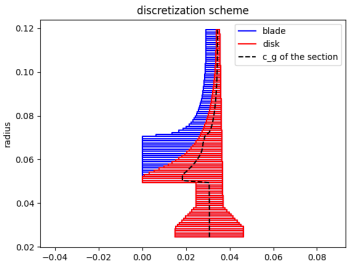

Figure E.21: Plot of the discretization of the T700 radial compressor with 100 volume elements

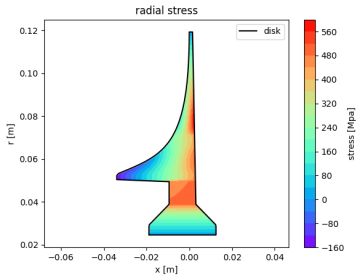

Figure E.22: Contour of the computed radial stress in the T700 radial compressor disk

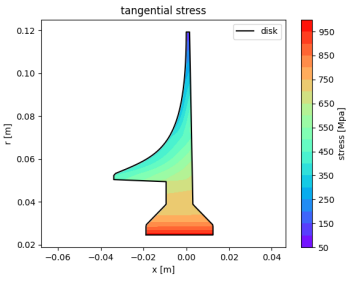

Figure E.23: Contour of the computed tangential stress in the T700 radial compressor disk

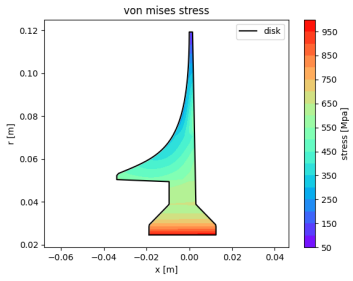

Figure E.24: Contour of the computed von Mises equivalent stress in the T700 radial compressor disk

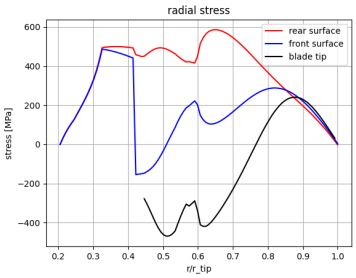

Figure E.25: Plot of the computed radial stress in the T700 radial compressor disk at the front and back surfaces

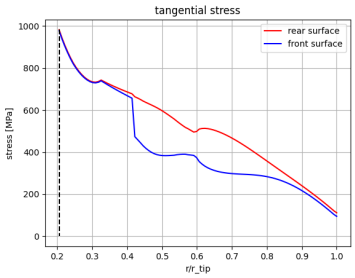

Figure E.26: Plot of the computed tangential stress in the T700 radial compressor disk at the front and back surfaces

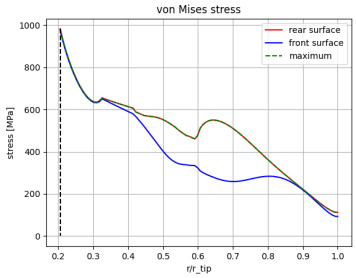

Figure E.27: Plot of the computed von Mises equivalent stress in the T700 radial compressor disk at the front and back surfaces

BIBLIOGRAPHY

[1] E.Steinhardt, *Aero-engine design: A state of the art,* von Karman Institute for Fluid Dynamics Lecture Series 2003-06 (2003).

[2] R. C. Bolam, J. P. C. Roque, S. Monir, A. Anuchin, and Y. Vagapov, *Review of low aspect ratio blade dynamics for electrical axial fans and compressors,* 56th International Universities Power Engineering Conference (UPEC) (2021).

[3] H.-O. To and R. J. Miller, *The effect of aspect ratio on compressor performance,* Proceedings of ASME Turbo Expo 2015: Turbine Technical Conference and Exposition (2015).

[4] e. a. E.M.Greitzer, *N+3 aircraft concept designs and trade studies, final report.* NASA Technical Reports Server **2:Appendices - Design Methodologies for Aerodynamics, Structures, Weight, and Thermodynamic Cycles** (2010), [Technical report].

[5] M. Gambini and M. Vellini, *Turbomachinery Fundamentals, Selection and Preliminary Design*, 1st ed. (Springer, 2020).

[6] H. Grieb, *Projektierung von Turboflugtriebwerken* (Springer Basel AG, 2004).

[7] C. Xu, *Design experience and considerations for centrifugal compressor development,* Proceedings of the Institution of Mechanical Engineers, Part G: Journal of Aerospace Engineering **221**, 273 (2007).

[8] C. Xu and R. S. Amano, *Empirical design considerations for industrial centrifugal compressors,* International Journal of Rotating Machinery (2012).

[9] G.S.Ray and B.K.Sinha, *Computation of centrifugal stresses in a radial-flow impeller,* Computers & Structures **40**, 731 (1991).

[10] X. Zheng and C. Ding, *Effect of temperature and pressure on stress of impeller in axial-centrifugal combined compressor,* Advances in Mechanical Engineering **8** (2016), 10.1177/1687814016653547.

[11] M. Schilhansl, *Stress analysis of a radial-flow rotor,* Journal of Engineering for Power, Transactions of the ASME , 124 (1962).

[12] A. Giuffre', P. Colonna, and M. Pini, *Design Optimization of a High-Speed Twin-Stage Compressor for Next-Gen Aircraft Environmental Control System,* Journal of Engineering for Gas Turbines and Power **145** (2022), 10.1115/1.4056022.

[13] R. H. Aungier, *Aerodynamic Design and Analysis of Vaneless Diffusers and Return Channels,* Turbo Expo: Power for Land, Sea, and Air, **Volume 1: Aircraft Engine; Marine; Turbomachinery; Microturbines and Small Turbomachinery** (1993), 10.1115/93-GT-101.

[14] R. H. Aungier, *Centrifugal Compressor Stage Preliminary Aerodynamic Design and Component Sizing,* Turbo Expo: Power for Land, Sea, and Air, **Volume 1: Turbomachinery** (1995), 10.1115/95-GT-078.

[15] B. Khandelwal, M. Yan, G. Hegde, V. Sethi, and R. Singh, *Design procedure of a reverse flow combustor for a helicopter engine with high temperature rise*, Tech. Rep. (SAE Technical Paper, 2011).

[16] G. Brown, A. Kascak, B. Ebihara, D. Johnson, B. Choi, M. Stebert, and C. Buccieri, *Nasa glenn research center program in high power density motors for aeropropulsion,* NASA/TM-2005-213800, ARL-MR-0628 [Technical Memorandum] (2005).

[17] E. Hendricks and M. Tong, *Performance and weight estimates for an advanced open rotor engine,* in *48th AIAA/ASME/SAE/ASEE Joint Propulsion Conference & Exhibit* (2012) p. 3911.

[18] H. Grieb, *Verdichter für Turbo-Flugtriebwerke* (Springer Berlin Heidelberg, 2009).

[19] M.Pini, *Lecture 7 – axial compressors,* AE4206 Turbomachinery (2022), department of Flight Performance and Propulsion, Faculty of Aerospace Engineering, Delft University of Technology. Delft, The Netherlands. February 2021. p. 5. [Lecture Content].

[20] Air Transport Action Group (ATAG), *Facts & figures,* (2020).

[21] M. Sielemann, A. Pitchaikani, N. Selvan, and M. Sammak, *The jet propulsion library: Modeling and simulation of aircraft engines,* Proceedings of the 12th International Modelica Conference, Session 11D: Aerospace , 909 (2017).

[22] Airborne Energy Harvesting for Aircraft (ARENA), *Knowledge centre organic rankine cycle (kcorc) : Rd projects,* (2022).

[23] I. H.Boersma, *Weight estimation of gas turbine engines: Development of a component-based preliminary engine design tool,* MSc thesis TU Delft (2022).

[24] P. Lolis, P. Giannakakis, V. Sethi, A. J. B. Jackson, and P. Pilidis, *Evaluation of aero gas turbine preliminary weight estimation methods,* The Aeronautical Journal **118**, 625–641 (2014).

[25] *An Integrated Method for Propulsion System Conceptual Design*, Turbo Expo: Power for Land, Sea, and Air, Vol. Volume 1: Aircraft Engine; Fans and Blowers; Marine (2015).

[26] P. Lolis, *Development of a preliminary weight estimation method for advanced turbofan engines*, Ph.D. thesis, Cranfield University (2014).

[27] E. Onat and G. Klees, *A method to estimate weight and dimensions of large and small gas turbine engines*, Tech. Rep. (1979).

[28] C. A. Snyder and M. T. Tong, *Modeling turboshaft engines for the revolutionary vertical lift technology project,* in *Annual Forum and Technology Display: The Future of Vertical Flight*, GRC-E-DAA-TN66991 (2019).

[29] C. A. Snyder, *Exploring advanced technology gas turbine engine design and performance for the large civil tiltrotor (lctr),* in *50th AIAA/ASME/SAE/ASEE Joint Propulsion Conference* (2014) p. 3442.

[30] B. T. Schiltgen and J. Freeman, *Aeropropulsive interaction and thermal system integration within the eco-150: A turboelectric distributed propulsion airliner with conventional electric machines,* in *16th AIAA Aviation Technology, Integration, and Operations Conference* (2016) p. 4064.

[31] P. Schmollgruber, D. Donjat, M. Ridel, I. Cafarelli, O. Atinault, C. François, and B. Paluch, *Multidisciplinary design and performance of the onera hybrid electric distributed propulsion concept (dragon),* in *AIAA Scitech 2020 Forum* (2020) p. 0501.

[32] J. L. Felder, G. V. Brown, H. DaeKim, and J. Chu, *Turboelectric distributed propulsion in a hybrid wing body aircraft*, Tech. Rep. (2011).

[33] W. R. Britsch, W. M. Osborn, and M. R. Laessig, *Effects of diffusion factor, aspect ratio, and solidity on overall performance of 14 compressor middle stages,* NASA Technical Paper 1523 (1979).

[34] G. J. Fahmi, *The performance of two axial-flow compressors of differing blade aspect ratio,* (1971).

[35] L. SMITH, *Casing boundary layers in multistage axial-flow compressors,* Flow Research on Blading , 275 (1970).

[36] M. Peter, T. Schmidt, and P. Jeschke, *Influence of blade aspect ratio on axial compressor efficiency,* Journal of the Global Power and Propulsion Society **3**, 639 (2019).

[37] M.V.Casey, *A mean line prediction method for estimating the performance characteristics of an axial compressor stage,* Proceedings of the Institution of Mechanical Engineers International Conference on Turbomachinery – Efficiency Prediction and Improvement. (1987), paper C 246/87.

[38] J.D.Denton, *Meangen description,* User Manual (2017), (last updated).

[39] J.D.Denton, *Instruction for program stagen,* User Manual (2017), (last updated).

[40] J.D.Denton, *Multistage turbomachinery flow calculation program: Multall_open,* User Manual (2020), (last updated).

[41] P.P.Walsh and P.Fletcher, *Gas Turbine Performance*, second ed. ed. (Blackwell Science, 2004).

[42] S. Lieblein, R. L. Broderick, and F. C. Schwenk, *Diffusion factor for estimating losses and limiting blade loadings in axial-flow-compressor blade elements* (National Advisory Committee for Aeronautics Washington, DC, USA, 1953).

[43] R. H. Aungier, *Centrifugal Compressors: A Strategy for Aerodynamic Design and Analysis* (ASME Press, 2000).

[44] F. Lou and N. L. Key, *Design considerations for the final-stage centrifugal compressor in aeroengines,* JOURNAL OF PROPULSION AND POWER **36**, 791 (2020).

[45] S. Reitenbach, M. Vieweg, R. Becker, C. Hollmann, F. Wolters, J. Schmeink, T. Otten, and M. Siggel, *Collaborative aircraft engine preliminary design using a virtual engine platform, part a: Architecture and methodology,* in *AIAA Scitech 2020 Forum* (2020) p. 0867.

[46] B. S. Eckert, *Axial- und Radial-Kompressoren.Anwendung/Theorie/Berechnung* (Springer, 1961).

[47] C. Osnaghi, *Teoria Delle Turbomacchine* (Esculapio, 2002) (in italian).

[48] F. J. Wiesner, *A Review of Slip Factors for Centrifugal Impellers,* Journal of Engineering for Power **89**, 558 (1967).

[49] D. J. L. Smith and H. Merryweather, *The use of analytic surfaces for the design of centrifugal impellers by computer graphics,* International Journal for Numerical Methods in Engineering **7**, 137 (1973).

[50] C. Bryce, J. Erwin, G. Perrone, E. Nelson, R. Tu, and A. Bosco, *Small, high pressure ratio compressor: Aerodynamic and mechanical design*, Tech. Rep. (Nasa Technical Report, 1973).

[51] M. Tong, I. Halliwell, and L. Ghosn, *A computer code for gas turbine engine weight and disk life estimation,* Journal of Engineering for Gas Turbines and Power-transactions of The Asme - J ENG GAS TURB POWER-T ASME **126** (2004), 10.1115/1.1691980.

[52] *MTR390—Engine for the Future*, Turbo Expo: Power for Land, Sea, and Air, Vol. Volume 2: Aircraft Engine; Marine; Microturbines and Small Turbomachinery (1992).

[53] W. Hunter, G. Grimmer, and G. E. C. L. M. A. E. GROUP, *T700 blisk and impeller manufacturing process development program*, Tech. Rep. (Tech. Rep. ADA093877, General Electric Company, 1979).

[54] J. Sawyer, *Sawyer's Gas Turbine Engineering Handbook: Maintenance & basic fundamentals*, Sawyer's Gas Turbine Engineering Handbook (Gas Turbine Publications, 1972).

[55] S. Mukherjee and D. Baker, *Thermal design of high pressure ratio turbocharger compressor wheels,* SAE Transactions , 498 (2002).

[56] S.Bretschneider, F.Rothe, M.G.Rose, and S.Staudacher, *Compressor Casing Preliminary Design Based on Features,* Turbo Expo: Power for Land, Sea, and Air **Volume 5: Structures and Dynamics, Parts A and B**, 1 (2008).

[57] K.Trappmann, J.S.Ducos, and A.R.Anderson, *MTR390 a new generation turboshaft engine,* Fifteenth european rotorcradt forum (1989).

[58] R. E. Wells and A. L. Romanin, *The gtcp331 auxiliary power unit for the next generation commercial transports,* SAE Transactions , 3479 (1980).

[59] G. GmbH, *GasTurb 14:Design and Off-Design Performance of Gas Turbines* (Copyright © 2023 by GasTurb GmbH) program Manual.

[60] *Mtu's official website page for the mtr390 engine,* (2023).

[61] M. G. Ballin, *A high fidelity real-time simulation of a small turboshaft engine*, Tech. Rep. (NASA Technical Memorandum 100991, 1988).

[62] *T700-401c/-701c turboshaft engines,* General Electric product datasheet .

[63] X. Zheng, L. Jin, Y. Zhang, H. Qian, and F. Liu, *Effects of disk geometry on strength of a centrifugal compressor impeller for a high pressure ratio turbocharger*, in *Gas Turbine India Conference*, Vol. 45165 (American Society of Mechanical Engineers, 2012) pp. 683–690.

[64] S. Lieblein, *Loss and stall analysis of compressor cascades,* Journal of basic engineering **81**, 387 (1959).

[65] C. Koch and L. Smith Jr, *Loss sources and magnitudes in axial-flow compressors,* (1976).

[66] A. Howell, *Development of the british gas turbine unit. new york,* (ASME, 1947).

[67] R. Aungier and S. Farokhi, *Axial-flow compressors: a strategy for aerodynamic design and analysis,* Appl. Mech. Rev. **57**, B22 (2004).

[68] M. Yaras and S. Sjolander, *Prediction of tip-leakage losses in axial turbines,* (1992).